Computational Modelling of Radiosensitising Properties of Nanoparticles

Thesis

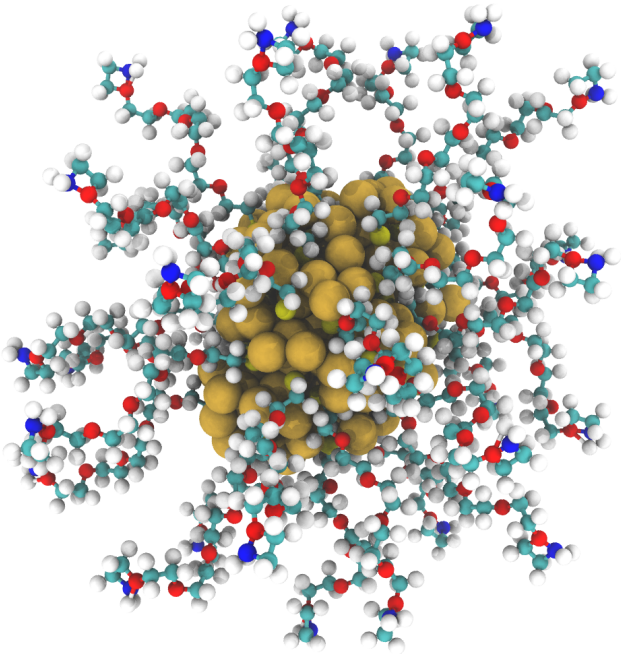

COMPUTATIONAL MODELING OF RADIOSENSITIZING PROPERTIES OF NANOPARTICLES

KASPAR HAUME

A thesis submitted in partial fulfilment for the degree of Doctor of Philosophy

School of Physical Sciences
The Open University

March 2018

Kaspar Haume: *Computational modeling of radiosensitizing properties of nanoparticles*

SUPERVISORS
Andrey V. Solov'yov
Nigel J. Mason

LOCATION
Copenhagen

SUBMISSION DATE
March 8th 2018

COLOPHON
This document was typeset with LaTeX using ArsClassica, a reworking of the ClassicThesis style designed by André Miede, inspired by *The Elements of Typographic Style* by Robert Bringhurst.

ABSTRACT

Metal nanoparticles (NPs) are currently under intense investigation due to their potential application in radiotherapy treatment of cancerous tumors by acting as radiosensitizing agents which may potentially lead to a reduction of side-effects caused by radiotherapy.

This thesis presents a framework to accurately explore a number of important parameters of coated NPs using computational and theoretical methods which may be applied to any coated NP system.

The detailed structure of poly(ethylene glycol) (PEG)-coated gold nanoparticles (AuNPs) was studied using atomistic classical molecular dynamics simulations. By varying the number of attached PEG molecules it was demonstrated that the thickness of the coating, and therefore the size of the overall NP, was independent of the coating molecule surface density. On the other hand, the water content of the coating was observed to decrease with increasing coating surface density. In particular, it was found that the region immediately outside the NP core was devoid of water for high coating densities.

The energetics of the coating formation was investigated by calculating the free energy change associated with the binding of a PEG molecule to a gold surface. The binding was demonstrated to be energetically favorable with a dominating contribution coming from a decrease in potential energy associated with the binding. This methodology may be extended to provide estimates for the lifetime of NP coatings *in vivo* where they have been shown to be degraded by exchange with biological proteins post administration.

The transport of low-energy secondary electrons emitted by a carbon ion-irradiated AuNP was calculated as a diffusion process and the radical production, due to inelastic collisions of the electrons inside the coating medium, was quantified. By varying the ion energy and coating water content we demonstrated that the presence of water near the NP surface is crucial in order to achieve radical production enhancement compared to pure water.

ACKNOWLEDGEMENTS

First and foremost I would like to thank my supervisors Professor Andrey Solov'yov and Professor Nigel Mason for the guidance and support they have provided during my studies and for allowing me to take part in the ARGENT project which has provided me with an awesome journey professionally, personally, and literally. In this regard I would also like to acknowledge the efforts of Sandrine Lacombe in regards to leading the ARGENT project and for all other early-stage researchers with whom I had the pleasure of collaborating and who made the stays in Paris, Genoa, and at conferences a great and fun experience.

The last half of the project was spent at MBN Research Center in Frankfurt working primarily in close collaboration with Pablo de Vera and Alexey Verkhovtsev whom I wish to thank especially for their help, assistance, and fruitful discussions during this time and for proofreading parts of this thesis.

At The Open University I had the pleasure of meeting many kind and friendly people who made my stay there fun and enjoyable. In addition to my stay at The Open University I also spent time at QuantumWise. I would like to express my gratitude to Kurt Stokbro for first suggesting me to apply for the ARGENT project and second for providing me with a rewarding experience while working at QuantumWise. Here I had a very exciting time in the Platform team and in the Dynamics team where I learned a lot and which provided a significant part of my research. I am very grateful for the numerous discussions with Dr. Julian Schneider and his help in preparing and proofreading parts of this thesis and for his patient and useful help whenever I needed it.

Most importantly, the constant support and encouragement of my family and friends made this entire period possible and provided a great source of energy and inspiration.

This project was part of the EU initial training network (ITN) ARGENT (Advanced Radiotherapy Generated by Exploiting Nanoprocesses and Technologies)[1] and has received funding from the European Union Seventh Framework Programme [PEOPLE - 2013 - ITN - ARGENT project] under grant agreement number 608163.

1 http://www.itn-argent.eu

CONTENTS

1 INTRODUCTION

Cancer is currently one of the leading causes of death worldwide and the number of cancer-diagnosed patients is rapidly increasing, in part due to an aging population, and is expected to reach 22 million cases in the next two decades [1]. Current cancer treatment can be grouped into three main categories: surgery, radiotherapy, and chemotherapy. Surgical treatment is the preferred method for superficial and nonmetastasized tumors while for inoperable tumors traditional chemotherapy and radiotherapy offer a possibility of treatment [2]. Radiotherapy is used in over 50 % of all cancer treatments but concerns about the damage induced in surrounding healthy tissue due to the nonspecific dose deposition of photon radiotherapy (X-rays or gamma rays) limit how much radiation a patient can receive without the risk of serious side-effects. The effort to increase the efficiency and reduce the side-effects of radiotherapy have been the aims of the recent multidisciplinary projects NANO-IBCT[1] and ARGENT[2] of which the present thesis is part of the research programme. While the primary focus of the NANO-IBCT project was the use of ion radiotherapy as an alternative to conventional photon radiation, since it promises significantly reduced the side-effects due to a highly confined dose deposition [3–6], ARGENT, in addition to ion radiotherapy, is also involved with research into the application of nanoparticles as a radiosensitizing agent.

In recent years nanoparticles (NPs) (particles with a maximum dimension of 100 nm) have emerged as a possible supplement to traditional cancer treatment protocols and have formed the basis of the field "nano-oncology" — the branch of medicine which exploits advances in nanotechnology for the treatment of cancer [7]. Several avenues are being pursued to increase the effectiveness of cancer treatment using NPs including: selective toxicity of the NPs to cancer tissue [8–10], NPs acting as drug carriers [11–14], or NPs aiding in the diagnosis by improving magnetic resonance imaging of tumors [15, 16]. This thesis focuses on the area of radiosensitizing NPs, that is, NPs which have the capability to locally increase the effect of radiation thereby allowing a lower total dose to be applied which ultimately means a lower risk of side-effects [5, 17–19].

The idea of using NPs as radiosensitizing agents first gained widespread attention after the promising results presented by Hainfeld *et al.* in 2004 [20], see Fig. 1.1. They demonstrated that the application of gold NPs to cancer tumors in mice in combination with X-ray radiotherapy lead to a drastically reduced tumor volume compared to X-ray treatment alone. Now more than a decade later, the field has advanced significantly on many fronts. How-

1 European COST Action "Nanoscale insights into Ion-Beam Cancer Therapy", http://www.cost.eu/COST_Actions/mpns/nano-ibct/

2 EU FP7 Initial Training Network Project "Advanced Radiotherapy Generated by Exploiting Nanoprocesses and Technologies", http://www.itn-argent.eu

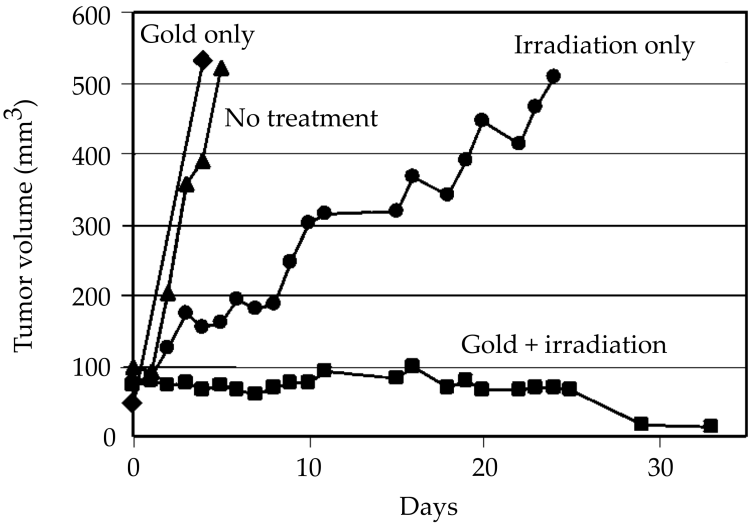

Figure 1.1: Average tumor volume in mice versus time after either no treatment, gold NPs only, X-ray irradiation only, or both gold NPs and irradiation as reported by Hainfeld *et al.* [20]. Figure adapted from [20].

ever, radiosensitizing NPs are still not used as a standard compliment to radiotherapy, despite clear experimental evidence of radiosensitization from a wide range of different NPs, due to a lack of a thorough quantitative understanding of these processes [21, 22].

The challenge of understanding the interplay between the NPs and the biological environment during radiation treatment is a highly multidisciplinary problem and requires input from the fields of physics, chemistry, biology, pharmaceutical engineering, and medicine. One of the main difficulties is the complex interplay between a large number of factors. Different types of cancer cell lines respond differently to the same treatment, results vary based on radiation modality for both photon radiation (photon energies) and for ion radiation (different ions and energies). Adding to the complexity the use of radiosensitizing NPs opens up even more questions. Optimizing the design of NPs for radiotherapy requires a full understanding of the specific impact of physico-chemical properties of NPs such as size, shape, material, and coating. These design parameters affect the physical response to the radiation (production of secondary electrons, interaction with radiation), the chemical response (production of radicals), and biological interactions (uptake to cells, localization inside cells, lifetime of NPs) [21, 23–26].

Performing controlled experiments to systematically vary one parameter at a time is nearly impossible due to the man power and money required for such a number of experiments. Computational modeling provides a complement to experiments and is increasingly being used to shed light onto the molecular-level mechanisms underlying radiosensitization [4, 27] and to evaluate theoretically the potential of a given NP [28, 29]. Provided the simulations capture the relevant effects, the design parameter-space can be efficiently sampled to weed out the less qualified proposals and suggest promising candidates for further experimental studies and may also provide insights into the processes underlying radiosensitization by NPs which happen on scales in time and space which are difficult to probe experimentally.

A realistic procedure to modeling such a complex problem should involve the theoretical descriptions of the key phenomena and explain their connections within a unified framework. During the past decade such an approach has been developed within the so-called multiscale approach to the physics of radiation damage with ions [4, 30]. One of the highlights so far was the accurate prediction of survival rates for a range of cell types irradiated with ions including effects such as production and transport of secondary species generated by the ionizing radiation as well as the repair rates of the various cell types [31].

There have also been attempts at evaluating the potential of NP designs using computational modeling [24, 28, 29, 32] but so far the effect of coating on radiosensitization has received little attention and NPs have been modeled as "naked" spheres of the material in question. As demonstrated experimentally, coatings do in fact have a significant effect on the potential of a given NP to act as a radiosensitizer [33, 34] and since all NPs used *in vivo* are coated, because naked NPs otherwise will be quickly cleared from the blood stream, it is therefore important to include this effect when estimating theoretically the radiosensitization capability of NPs.

The present thesis is concerned with this challenge. Extending the multiscale approach [4] with the inclusion of NPs to the evaluation of biological damage due to ion radiotherapy, we outline a framework for the accurate modeling of coating structure and its effect on the production of secondary species which determines the effectiveness of a NP as a radiosensitizing agent. As a case study the focus will be on system of a poly(ethylene glycol) coated AuNP which is a commonly investigated combination [8, 35] but we stress that the presented framework is completely general and we therefore expect it to provide a useful means for evaluating any coated NP proposal and therefore to be a convenient tool to guide the rational design of NPs and their coatings.

Below, the main principles of radiotherapy and the mechanisms of NPs acting as radiosensitizing agents are briefly summarized. We then outline some of the main challenges in field of optimizing the design of radiosensitizing NPs and how we address these problems in the present thesis.

1.1 PRINCIPLES OF RADIOTHERAPY

Radiotherapy is based upon the deposition of energy in the tissue under irradiation by ionization of the medium ultimately leading to the death of irradiated cells after delivery of a sufficient dose. Although the radiation may ionize and damage DNA or other organelles, called "direct damage", the main interaction of the radiation is with water due to the fact that water is the main constituent of the human body. Indeed several studies have shown that the main pathway of DNA damage is mediated by the production of water radicals due to hydrolysis induced by the radiation ("indirect damage") [18, 36–38]. These radicals can aggressively interact with organelles of the cell thereby causing damage to cell-critical structures such as the mitochondria or the DNA. In addition, electrons produced during the ionization

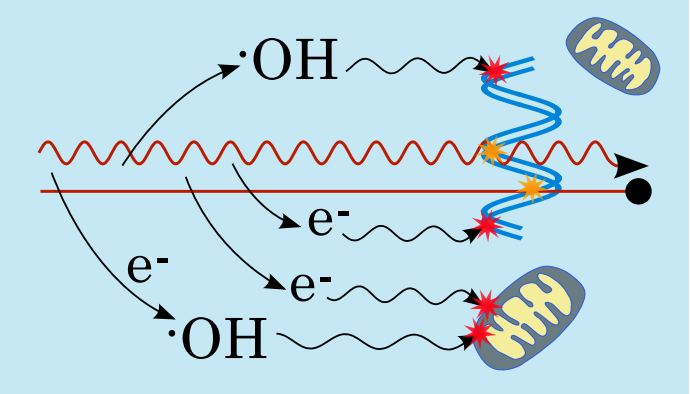

Figure 1.2: Both photon and ion radiation (red wiggly and straight lines, respectively) may directly damage DNA (marked with yellow stars) or other parts of the cell, such as mitochondria, as well as ionize the medium which may lead to the production of radicals (represented here by the OH radical) as well as secondary electrons which may both damage cell structures (red stars) or may react with the medium to further increase the number of radicals. Note that the different processes shown and the distances involved are not to scale but simply illustrate the damage pathways.

of the water medium may also cause biodamage or may further increase the radical production [37, 39, 40]. Figure. 1.2 illustrates the damage pathways.

The major difference between photon and ion radiotherapy is the manner of dose deposition. Photons traveling through biological tissue deposit energy with an exponential decay which means that tissue located in front of and behind the tumor will receive significant doses. This is the lead cause of side-effects caused by radiotherapy [41]. Ion radiation has a distinct dose deposition curve. The energy deposited to the medium by a traversing ion is inversely proportional to its velocity resulting in a low dose in the entrance channel and a sharp peak in the deposited dose at the end of the ion track [3, 4, 42], see Fig. 1.3. This peak in the deposited energy is known as the Bragg peak and leads to a highly confined dose within just a few millimeters while the position of the Bragg peak can be adjusted by selecting the initial energy of the ion. Ion radiation is therefore the preferred treatment for tumors situated close to critical organs such as eye or brain stem [3, 43], see Fig. 1.4 for an illustration of the difference in dose deposition around an irradiated tumor.

While the actual mechanisms of producing the biodamage are different, both photon and ion radiation fundamentally cause damage by ionizing the medium ultimately leading to the production of radicals which can damage biological structures and electrons which can further increase the production of radicals as well as cause damage directly. The same principles are behind radiosensitization due to NPs: While the interaction between the radiation and the NP is different for photons and ions, in both cases radiosensitization is achieved by an increased production of radicals and electrons, as will be detailed below.

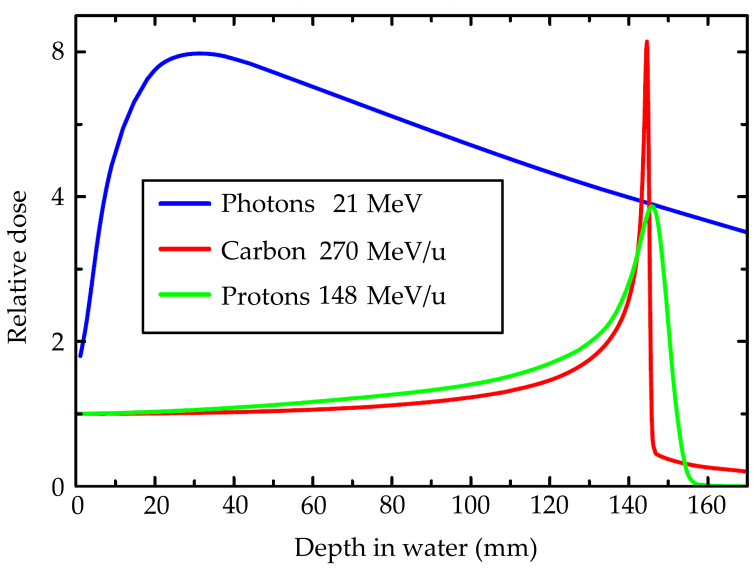

Figure 1.3: Depth dose distribution for photons, protons, and carbon ions. Figure adapted from [43].

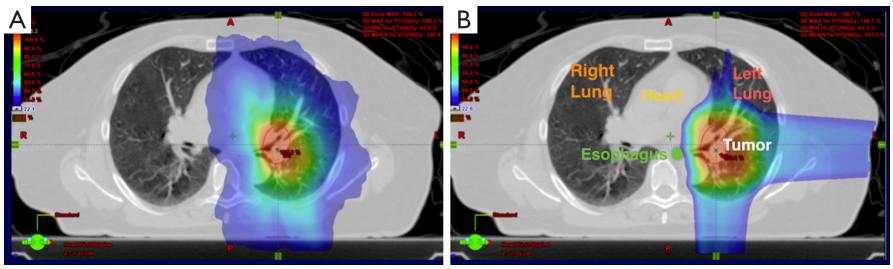

Figure 1.4: Comparative dose deposition for (A) photon and (B) proton radiotherapy (blue = low dose, red = high dose). Both modalities achieve maximum dose at the tumor site, but proton radiotherapy spares a significant amount of surrounding tissue compared to photon radiotherapy. Figure adapted from [44].

1.2 MECHANISMS OF RADIOSENSITIZING NANOPARTICLES

Exploiting the field of nanobiotechnology, suitably synthesized NPs have been shown to be efficient radiosensitizers for both photon and ion radiation [20, 36, 38, 45]. It is now widely accepted that the radiosensitizing properties of NPs depend on their ability to increase the production of water radicals. This is thought to occur due to emission of secondary electrons from the NPs which in turn leads to hydrolysis of nearby water molecules. As in the case of radiotherapy without NPs it is mainly these water radicals that attack DNA and other parts of the cell [36]. Although direct damage caused by secondary electrons is possible it has been demonstrated that the impact of secondary electrons accounts for less than 10 % of the damage to the cells versus 90 % for the radical-mediated damage [37, 38, 46] and it is thus the increasing radical yield that is the main contribution of radiosensitizing NPs.

Ionizing X-rays and gamma photons have the energy to excite core electrons of the atoms the irradiated NPs which may relax in a so-called Auger de-excitation process, emitting one or more Auger electrons, the latter being the case in Auger cascades in which NPs may emit more than 10 electrons this way [16, 47]. The electrons emitted due to photon irradiation are usually reported to have energies in the keV-range with little focus given to low-energy electrons below about 100 eV.

This is in contrast to electrons produced during ionization due to ion radiation with energy corresponding to an ion in the Bragg peak region. In this thesis the focus is on ion irradiation by carbon ions in the Bragg peak region (0.3 MeV/u) where Auger cascades are less relevant due to a small ionization cross section of inner-shell electrons [48] and because the maximum energy transfer is smaller than the ionization threshold of inner shells. In this thesis, our focus is therefore on electrons emitted from the outer shells of the NP atoms which have have kinetic energies below 100 eV [4, 49]. Low-energy electrons (below about 50 eV) have become an area of interest in the picture of biodamage since Boudaïffa experimentally demonstrated DNA strand damage as a result of interaction with 3 eV to 20 eV electrons [50]. Now actively researched to better understand their formation and interactions with surrounding medium [39, 40] their importance has also been demonstrated in the field of radiosensitizing NPs [33, 51]. For gold NPs up to 48 atoms under proton irradiation the mechanisms for emission of low-energy electrons were recently revealed theoretically by Verkhovtsev *et al.* [52] and it was shown that the production of electrons from these metal NPs with energies below about 50 eV was increased about an order of magnitude as a result of collective electronic excitation in the NP compared to a similar volume of water [51, 52]. The electric field from the passing proton excites plasmons in the NP (especially surface plasmons) and so-called atomic giant resonances in individual atoms due to the *d*-electrons and it is the relaxation of these excitations which lead to the emission of low-energy electrons.

It should be mentioned that energetic δ-electrons, with energies above 100 eV, may be emitted from NPs under ion irradiation when the ions are energetic enough. While the focus in this thesis will be kept on low-energy

electrons an estimate of the contribution from these electrons when the ion energy is increased beyond that of the Bragg peak region will be made.

1.3 AIMS OF THIS THESIS

This thesis presents a coherent modeling framework for studying the detailed structure of coated NPs and to evaluate their potential as radiosensitizing agents due to the emission of low-energy electrons (of a few tens of eV) as a result of excitation by carbon ion irradiation. A detailed procedure is provided on how to prepare the NP core and coating as well as the simulations performed in order to make it simple to apply the framework to other systems of interest. We have focused on PEG-coated gold NPs due to their widespread use in experiments but it is important to stress that the framework presented in this thesis is entirely system-agnostic and may well be used for any combination of NP core and coating material.

Providing a well-described and physically grounded framework for the accurate modeling of the structure of coated NPs and their radiosensitizing properties due to low-energy electrons will hopefully accelerate the already extensive work in optimizing the design of NPs as radiosensitizing agents.

To do this, we focus on three main problems as outlined below.

1.3.1 Problems addressed in this thesis

Coating structure

Metallic NPs for biomedical use are commonly synthesized with an organic coating to improve stability under physiological conditions, reduce toxicity, and to improve targeting capabilities of NPs post administration. One of the most popular coating molecules is the polymer poly(ethylene glycol) (PEG) [14, 35, 53–55]. PEG coatings have been shown to increase blood circulation time, improve stability, and reduce toxicity. Furthermore since it is relatively easy to attach PEG molecules to the surface of NPs during synthesis and PEG can be purchased in a wide range of lengths, there is considerable research to optimize the PEG coating structure and to understand the mechanisms of radiation/PEG interactions [56–62].

Recent studies agree that the thickness of the PEG coating and the surface density (PEG molecules per surface area) play key roles in the coating's ability to protect the NP *in vivo* [54, 55, 63]. However, finding the optimal design is complicated by the fact that the length of the individual PEG molecules as well as the size and shape of the NP play important roles in the resulting structure, and therefore effectiveness, of coatings as well [55, 64, 65]

To estimate theoretically the conformation and thickness of PEG coatings it is common to apply the framework outlined originally by de Gennes [66, 67] for the study of the conformation of polymers attached to surfaces [55, 68, 69]. In this picture the conformation of the polymers depends on the distance between their attachment points and will tend to attain a more linear conformation with increasing surface density resulting in a thicker coating. The issue is that this framework assumes polymers attached to flat

surfaces and since it is well established that the curved surfaces of NPs can accommodate more PEG molecules per area than a flat surface [56, 62, 63] it is questionable whether the de Gennes-framework should be relied on for estimating NP coating thicknesses.

Besides being important for the protection of the NP *in vivo*, the thickness of the coating is important because the total size of the NP affects uptake into cells [26, 70]. In addition, since one may expect a dense coating to be less permeable to water, which has been shown to be important for the radiosensitizing capabilities of coated NPs [33, 34], it is necessary to predict the detailed coating structure and hydration as a function of surface density.

In Chapter 3, it is demonstrated how to prepare the NP core, obtain and manipulate coating input files, attach the coating, apply a water box, and perform molecular dynamics simulations of gold NPs of 1.6 nm diameter coated with between 4 and 60 PEG molecules corresponding to a range in surface densities found in literature. By performing atomistic simulations the detailed structure of the coating is obtained as a function of surface density by calculating the radial density distribution function of the elements of the PEG coating as well as the water content of the coating. We show that the total thickness of the coating is independent of surface density within the studied range which is in contrast to the de Gennes-framework. On the other hand we find that the water content of the coating depends on the surface density with high PEG surface density leading to a low water density especially near the NP surface.

Energetics of coating formation

One of the issues with the design of PEG coatings is that it is difficult to verify how many PEG molecules are on the surface of the NP and therefore the surface density of the PEG molecules [55, 61]. A number of methods for estimating this exist but measurements of the loading are often imprecise [61]. Dynamic light scattering is widely used to characterize the size of coated NPs but it cannot tell the number of bound PEGs. Another method is to measure the PEG concentration in solution before and after being mixed with NPs, but this fails to take into account PEGs which are nonspecifically bound, meaning they are not directly bound to the surface but are entangled in the coating or bound to the surface by the "tails" of the PEG molecule. This method therefore tends to overestimate the PEG surface density.

Therefore even if an optimal surface density can be established, it is not easy to verify the resulting NP structure post synthesis. As mentioned above, results on the thickness and detailed structure of PEG coatings as a function of surface density will be presented in Chapter 3. A range of attached PEG molecules have been applied according to surface densities reported in literature and we show that the surface density has a significant effect on the hydration of the coating. There is, therefore, a need for a more precise procedure for predicting the surface density.

Besides a need for a better understanding of the optimal number of attached molecules, there is a need for being able to investigate the lifetime of the coating. It is known that the coating of a NP introduced to cells *in vivo* will gradually be exchanged with more prevalent molecules found in the

biological environment such as glutathione [71, 72]. The rate of exchange is likely to depend on the energetics of the binding of these molecules and a methodology of quantifying the energetics may therefore be able to predict the lifetime of a PEG coating in the biological environment.

In Chapter 4, the energetics of the attachment of a PEG molecule to a gold surface will be studied and this will be related to the free energy associated with the bond formation using two different methods. In the first method, a variation of molecular dynamics known as metadynamics simulations are performed [73, 74]. Being an "enhanced sampling method", the principle of metadynamics is to map out the free energy surface of a chosen reaction coordinate. By choosing the z-component of the sulfur atom of the PEG molecule, which is the direction normal to the gold surface, it is possible to reconstruct the free energy landscape associated with the adsorption of the PEG molecule and from it the change in free energy associated with the binding event. Metadynamics inherently includes all entropic contributions and surface adsorption configurations and we therefore use this result as the reference value.

In the second method we make a semi-analytical estimate of the Helmholtz free energy change when binding to the surface by calculating the potential energy change from the PEG molecule being in solution to being adsorbed on the gold surface and adding to it an analytical estimate of the entropy change associated with the binding.

Both methods indicate that the binding of the PEG molecule is energetically favorable with a binding energy somewhere between the strength of a physisorbed bond and a covalent bond. The differences in the results of the two methods are discussed as well as how this first step may be taken forward for calculations of the binding free-energy in more complicated scenarios, e.g. during the synthesis of a NP coating.

Radiosensitizing properties of coated NPs

The radiosensitizing properties of coated NPs have been demonstrated experimentally [36, 75, 76]. However, the optimal design of such NPs is still not clear and a systematic optimization of the design of NPs for radiosensitization is made difficult by the highly complex interplay between a large number of factors such as radiation type and energy; size, shape, and material of NP core; and type and structure of coating. While computer simulations may aid in sampling the design-parameter space and thus accelerate the process of screening suitable candidates, current models neglect the influence of the coating [24, 28, 29, 32]. Following the results of recent experiments which demonstrated the significant impact of coatings in the picture of radiosensitization [33, 34, 37], there is a need for a modeling approach which takes the coating into account. Current Monte Carlo simulations, in addition to neglecting coating of NPs, are also restricted to considering higher energy electrons emitted from NPs under irradiation. For this reason, most Monte Carlo simulation consider Auger electrons of energies in the range of 10^2 eV to 10^3 eV due to a lack of cross section parameters for lower energies [24, 28, 29, 32].

In Chapter 5 a unified framework of several discrete areas of theory is outlined to estimate the radiosensitizing capabilities of a PEG-coated gold NP due to low-energy electron emission as a result of carbon ion irradiation. Here an extension to the multiscale approach [4] is presented combining the following previously published work on the relevant processes and effects: (i) calculations of the energy spectrum and number of low-energy electrons emitted from a gold NP under ion irradiation by considering two main contributions to the excitation of the NP by the ion, namely plasmon-type excitations and collective excitation of 5*d* electrons in individual atoms of the NP [51], (ii) a model for describing the transport of low-energy electrons as a diffusion process [77], and (iii) calculations of the elastic and inelastic mean free paths of low-energy electrons with organic media [78, 79] to obtain the parameters to describe the diffusion process after having derived the solution to the diffusion equation for electrons emitted from a the surface of the NP diffusing into two media (the NP core and the PEG coating).

Combined with the methodology of simulating the structure of coatings, presented in Chapter 3, two resulting structures are considered and it is shown that the water content of the coating is a critical parameter of a coating structure for the production of water radicals. Since almost all electrons emitted from the NP will inelastically scatter before escaping the coating, with the majority doing so within just 0.3 nm to 0.5 nm from the NP surface, the ability of the coating to allow water to reach the surface has a major impact on the water radical production induced by electrons emitted from the NP.

By varying the ion energy and the water content, the radical production compared to having no NP present is calculated. By varying the ion energy it is found that the radical production compared to the case of no NP present increases with energy and that the energy of the ion which leads to the highest water radical production is significantly higher than what is realized in the Bragg peak. This indicates that PEG-coated gold NPs of similar dimensions to the one studied are more efficient radiosensitizers in the entrance channel than in the Bragg peak region. Second, it is demonstrated, by approximating the coating as a homogeneous material with a variable water content, that a small but even water content in the coating leads to a higher radical production than a higher average water content if no water is present at the NP surface.

To the best of our knowledge, this is the first study showing how the detailed structure of the coating affects secondary species production mediated by low-energy electron emission due to ion irradiation. Since this framework is completely general and may be applied to any NP core and coating type and for ions of any energy we expect this general framework to be a useful tool for experimentalists and theoreticians to screen proposed NP designs and gain an understanding of some the mechanisms behind radiosensitization.

1.4 OUTLINE OF THESIS

The thesis is organized as follows. In Chapter 2 the theory behind the modeling techniques applied in this thesis is introduced along with the used software. Here the principles of molecular dynamics simulations are presented including the basic assumptions of such algorithms, the mechanisms of thermostats, and how interatomic interactions are parametrized with interatomic potentials. In addition the variation of molecular dynamics simulations known as metadynamics simulations is presented. Belonging to the family of "enhanced sampling" techniques metadynamics can be effectively used to probe rare events such as desorption of a strongly bound adsorbate from a surface. Finally, the theory of diffusion and related concepts such as flux and fluence are briefly introduced.

Chapter 3 presents the results of the research carried out on the modeling of the coating structure of a PEG-coated gold NP. This includes the thickness of the coating as a function of the number of coating molecules attached and a detailed radial distribution of the coating elements and degree of water penetration from the solvent.

Chapter 4 presents the work performed in estimating the binding free energy of a PEG coating on a gold surface aiming at being able to estimate the number of coating molecules that will attach to a NP during synthesis as well as estimating the stability of the coating which, *in vivo*, has been shown to have a limited lifetime due to exchange with molecules present in the biological environment. In this chapter the binding free energy is estimated by metadynamics simulations as well as by employing a semi-analytic description of Helmholtz free energy change associated with the binding of a molecule to the surface and compare these two distinct methods.

In Chapter 5 a unified framework for modeling the transport of low-energy secondary electrons through the coating of an carbon ion-irradiated NP is presented and the production of radicals as a result of inelastic collisions between the electrons emitted from the surface of the NP and the water medium in which the NP is solvated is estimated. By varying the water content of the coating and the ion energy the radical production is explored for a range of situations compared to having no NP present.

Finally, Chapter 6 will conclude this thesis and provide an outlook of the work undertaken as well as outline how the work may be continued in the future.

2 METHODOLOGY

In order to improve the radiosensitization performance of nanoparticles (NPs) many experimental studies have been performed but it is difficult to replicate exact experimental conditions and so comparisons between different data sets are often of little value. Computer simulations provide a method for providing well characterized input parameters that can be replicated in a suite of models while also often being faster and cheaper than experiments.

Investigating the fundamental processes underpinning radiosensitization of NPs requires spatial resolution on the Ångström (10^{-10} m) scale (e.g. densities of produced radicals and electrons, atomistic geometry of the NPs and coatings) and temporal resolution on the femtosecond (10^{-15} s) scale (the timescale for transport of electrons and formation of radicals). The challenge is that, although the smallest features are on these scales, the field of radiosensitization involves not only physical but also chemical and biological processes which increase the relevant spatial scales to µm and mm (10^{-6} m to 10^{-3} m) (dimension of cells and tumors) and the temporal scales to seconds or even days (the timescale of biological processes such as repair of damage or cell death).

This thesis is focused on a number of problems which can be analyzed by considering the atomistic structure and dynamics of NPs and their coating using molecular dynamics simulations. In Section 2.1 we introduce this theory and argue why this is a suitable methodology for studying the structure of coated NPs.

In order to study the energetics of forming a coating and its resulting stability, we use a variation of molecular dynamics called metadynamics introduced in Section 2.2. This method allows computational sampling of events which may take too long to observe with ordinary molecular dynamics such as the desorption of molecules bound strongly to a surface as in the case of a poly(ethylene glycol) molecule bound to a gold surface. The result of this calculation is compared with a semi-analytical estimate of the Helmholtz free-energy change associated with the binding of such a molecule to a gold surface by considering separately the potential energy change and an analytical estimate of the entropy change of the binding event.

Finally, to analyze the transport of low-energy electrons emitted from a gold NP under ion irradiation, we apply a diffusion model. Combining this with the results of the coating structure simulations, as well as other theories previously published by colleagues in the ARGENT project, it is demonstrated how the radical production of a PEG-coated gold NP under ion irradiation compared to having no NP present can be calculated. A brief introduction to the theory of random walks and diffusion is given in Section 2.3.

2.1 MOLECULAR DYNAMICS

This section serves as an introduction to the theory of molecular dynamics (MD) simulations followed by a brief summary of the main theoretical concepts and aims at supplying the reader with a foundation for appreciating the capabilities of this type of simulation and the practical elements that one must consider while performing them. The following introduction is by no means a thorough treatment of the subject. Excellent introductory texts about MD simulations are written by Frenkel & Smit, Rapaport, and Allen [80–82].

The aim of MD is to model the behavior of matter at the atomic level by following the time evolution of a set of atoms by integrating the equations of motion for the system. An fundamental description of the interactions of atoms requires the solution of the Schrödinger equation for the system but even with numerical methods this becomes very time-consuming when approaching system sizes of 10^2 to 10^3 atoms. Since the mass of nuclei are thousands of times larger than that of electrons it is possible to make an approximate solution by considering the dynamics of the electrons as independent of the velocity of the nuclei such that it only depends on their positions. This is known as the Born-Oppenheimer approximation [83] and it follows that the dynamics of nuclei may, to a good approximation, be treated using classical mechanics and can thus be described by Newton's equation of motion

$$\mathbf{F}_i = m_i \mathbf{a}_i = m_i \frac{\mathrm{d}^2 r_i}{\mathrm{d}t^2}, \tag{2.1}$$

where m_i is the mass of atom i and $\mathbf{a}_i$ is the acceleration resulting from the force $\mathbf{F}_i$ acting on atom i. The force is given by

$$\mathbf{F}_i = -\boldsymbol{\nabla} U(\mathbf{r}_i), \tag{2.2}$$

where $U(\mathbf{r}_i)$ is the potential at position $\mathbf{r}_i$.

All information about the system obtained via MD simulations comes from the motion of the atoms and the description of the potential is therefore a critical element of MD simulations. The potential is, in classical MD, approximated by interatomic potential functions parametrized to capture the relevant contributions to the potential felt by the atoms of the system being simulated and since the motion of the atoms is based on the forces acting on them the ability of a MD simulation to yield realistic results rests on the interatomic potentials being a good descriptor of the dynamics of the system in question. A brief introduction to this concept is presented in Section 2.1.1, however it should be mentioned that the formulation of such interatomic potentials is itself a wide field of research and a full treatment goes beyond the scope of this thesis.

A simple MD simulation proceeds as follows: From an initial starting point forces are calculated on all atoms using Eq. (2.2) which leads to an acceleration of all atoms, as given by Eq. (2.1), and the positions of all atoms are then advanced by integration of the equation of motion, this is discussed in Section 2.1.2.

The simple Newtonian MD simulation models a system in which energy is conserved, but in a realistic environment it is not the energy of the system

but the temperature which is controlled. Temperature control is not possible in Newtonian dynamics but requires the use of a "thermostat" which introduces some degree of stochastic dynamics to the system to model the random motion of particles at finite temperatures. Different types of thermostats are often realized by solving the Langevin equation instead of Newton's equation of motion, this is discussed in Section 2.1.4. Before introducing temperature control it is useful to briefly introduce some relevant concepts of statistical mechanics which form the connection between the microscopic state of the simulated system (positions and velocities of atoms) and macroscopic properties such as heat capacity, pressure, and also temperature. This is discussed in Section 2.1.3.

For the sake of completeness two different kinds of MD simulations are briefly presented in Section 2.1.5 namely *ab initio* MD and coarse-grained MD. In the most accurate forms of MD the forces acting on the nuclei of the system are calculated by electronic structure calculations at every step in the simulation by solving the Schrödinger equation. This is the basis of *ab initio* MD (AIMD) to which a short introduction is given in Section 2.1.5. AIMD simulations are relatively computationally demanding for large systems (beyond about 10^3 atoms) and since the systems considered in this thesis are on the order of 10^4 atoms, classical MD simulations were performed in this thesis. Finally, it is possible to simplify the calculations by reducing the degrees of freedom of the system to allow for larger systems and longer simulations. This is done by treating groups of atoms, for instance each water molecule, as a single virtual particle. This type of MD is called coarse-grained MD (CGMD) and is also briefly discussed in Section 2.1.5.

2.1.1 Interatomic potentials

Although the interactions between atoms and ions stem from electronic interactions, and as such fundamentally are quantum mechanical in nature, classical MD sees atoms as hard spheres with point masses and bonds as a complex network of springs. The main motivation for this approach is that it is simpler, and therefore faster, than a full quantum mechanical description and works very well with correct fitting.

One of the simplest classes of interatomic potentials are the pairwise potentials which are, in general, given by

$$U_{\text{tot}} = \frac{1}{2}\sum_{i}^{N}\sum_{j\neq i}^{N} U(r_{ij}), \tag{2.3}$$

where U_{tot} is the total potential energy of the system, comprising N atoms, summed up as the potential energy $U(r_{ij})$ between all pairs of atoms i and j separated by the distance r_{ij}. An example of a such a potential is the Lennard-Jones potential [84] which describes a nonbonded, pairwise interaction between particles for which the potential is attractive at long distances, due to van der Waals forces, and repulsive at short distances, representing

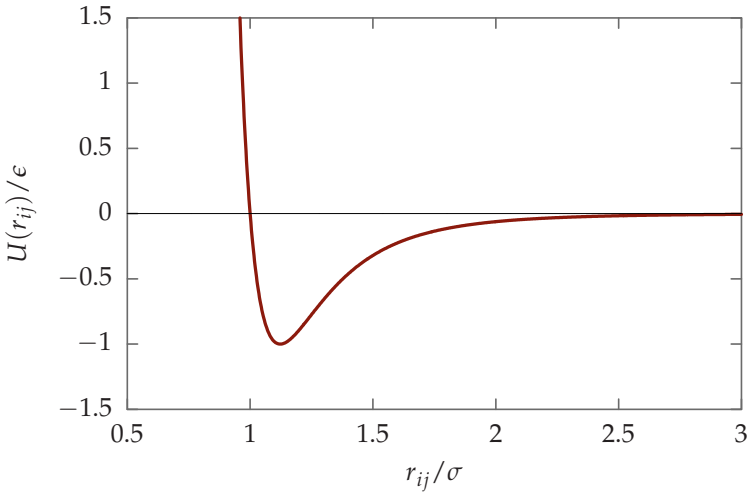

Figure 2.1: The Lennard-Jones potential $U(r_{ij})$ versus distance r_{ij} between two atoms i and j as given by Eq. (2.4). Shown in dimensionless units.

the Pauli exclusion principle. The potential energy $U(r_{ij})$ is in this case given by

$$U(r_{ij}) = 4\epsilon\left[\left(\frac{\sigma}{r_{ij}}\right)^{12} - \left(\frac{\sigma}{r_{ij}}\right)^{6}\right], \tag{2.4}$$

where ϵ is the potential well depth, $2^{1/6}\sigma$ is the pair equilibrium distance, and r_{ij} is the distance between the i'th and the j'th atom, see Fig. 2.1. The Lennard-Jones potential works reasonably well for describing weakly interacting noble gases but for condensed systems a simple pair potential is usually not enough. In the case of silicon Stillinger-Weber extended a pair potential description with a $\left(\cos\theta_{jik} + \frac{1}{3}\right)^2$ term (where θ_{jik} is the angle between three connected atoms j, i, and k) to discriminate in favor of the tetrahedral bond angle, which turned out to be a good description of ideal face-centered cubic (FCC) crystals, such as silicon [85]. Another example is the Tersoff potential [86] which extended the simple pair description to include a bond order term, thus taking into account the local environment, which could also describe the structure of silicon.

For metallic systems the pair potentials are too simple because the bond strength between an atom i and another atom j depends on how many bonds i and j have already formed with other atoms — something which is not taken into account by pair potentials. In metals "embedded atom model"-type potentials are commonly used [87]. In this thesis one such potential is used to describe the gold core of the NPs, namely the Sutton-Chen potential which has the form [88, 89]

$$U_{\text{tot}} = \epsilon\sum_i\left[\frac{1}{2}\sum_{j\neq i}\left(\frac{a}{r_{ij}}\right)^n - c\sqrt{\rho_i}\right], \tag{2.5}$$

where

$$\rho_i = \sum_{j\neq i}\left(\frac{a}{r_{ij}}\right)^m, \tag{2.6}$$

c is a dimensionless parameter, ϵ is a parameter with dimensions of energy, a is the lattice constant of the bulk phase for the metal, r_{ij} is the distance

between the i'th and the j'th atom, and m and n are positive integers with $n > m$.

In this thesis the CHARMM force field, which is widely used to describe the interactions of biological molecules, is used to describe the interactions of the coating molecules [90, 91]. It relies on an extensive parametrization of the interactions of atoms based on their local bonding environment. A carbon atom in a benzene ring is parametrized differently than a carbon atom in an aliphatic compound, for instance.

The contributions to the total energy in the CHARMM force field from bonded interactions are

$$U_{\text{bond}} = \sum_{\text{bonds}} K_{\text{b}} \left(b - b^0\right)^2 \tag{2.7a}$$

$$U_{\text{angle}} = \sum_{\text{angles}} K_\theta \left(\theta - \theta^0\right)^2 \tag{2.7b}$$

$$U_{\text{UB}} = \sum_{\text{UB.}} K_{\text{UB}} \left(b^{1-3} - b^{1-3,0}\right)^2 \tag{2.7c}$$

$$U_{\text{dihedral}} = \sum_{\text{dih.}} K_\varphi \left(1 + \cos\left(n\varphi - \varphi^0\right)\right) \tag{2.7d}$$

$$U_{\text{improper}} = \sum_{\text{impr.}} K_\omega \left(\omega - \omega^0\right)^2, \tag{2.7e}$$

where K_i is a force constant for the interaction type i and $b - b^0$, $\theta - \theta^0$, and $\omega - \omega^0$ is the difference from equilibrium for the bond length, bond angle, and improper angle respectively. The Urey-Bradley (UB) term takes into account the separation and angle between atoms 1 and 3 (that is, next-nearest neighbors). In the dihedral angle term, n is the multiplicity indicating the number of minima and $\varphi - \varphi^0$ is the difference from equilibrium.

The nonbonded interactions are

$$U_{\text{LJ}} = \sum_{\text{nonbon.pairs}} \epsilon_{ij} \left[\left(\frac{r_{\text{min},ij}}{r_{ij}} \right)^{12} - 2 \left(\frac{r_{\text{min},ij}}{r_{ij}} \right)^{6} \right] \tag{2.8a}$$

$$U_{\text{C}} = \sum_{\text{nonbon.pairs}} \frac{q_i q_j}{k_e r_{ij}}, \tag{2.8b}$$

where U_{LJ} is the Lennard-Jones interaction as described above. The depth of the energy well ϵ_{ij} for a bond between atoms of type i and j and the equilibrium distance for the bond $r_{\text{min},ij}$ are found from the CHARMM library which lists values of ϵ and r_{min} for all the defined atom types and which are then combined using the combination rules

$$\epsilon_{ij} = \sqrt{\epsilon_i \epsilon_j} \tag{2.9a}$$

$$r_{\text{min},ij} = \frac{r_{\text{min},i} + r_{\text{min},j}}{2}. \tag{2.9b}$$

The other nonbonded interaction U_{C} is the Coulomb interaction between two particles with partial charges q_i and q_j separated by a distance r_{ij} and $k_e = 1/(4\pi\varepsilon_0\varepsilon_r)$ is the Coulomb constant with ε_0 and ε_r being the vacuum permittivity and relative permittivity of the medium, respectively.

It should be noted that the bonded interactions of the CHARMM force field are all harmonic approximations (apart from the dihedral interaction),

effectively meaning that they reproduce only small deviations from equilibrium accurately. A consequence of this fact is that the CHARMM force field cannot be used to model bond breaking and formation.

To describe the water medium in the simulation, the CHARMM force field is used with parameters for water from the TIP3P water model [92, 93].

2.1.2 Integration of equations of motion

Classical molecular dynamics is in the simplest case the solution of Newton's equations of motion for a set of atoms defined by the interactions between them due to the applied interatomic potentials. From an initial starting point forces are calculated on all atoms, which leads to an acceleration of all atoms as given by Newton's first law, Eq. (2.1).

It is a fairly simple task to write an algorithm that integrates the equations of motion but not all algorithms do this well, in the sense that results are comparable with expectations based on experiments. It is not a trivial task to define exactly what a good algorithm is, should it for example be able to predict the precise position of all atoms for any time duration, or should it for example be able to predict the exact time at which a solid melts?

Knowing that we are (in the simple case) solving Newton's equations of motion a better quantity to observe, when judging the quality of an MD algorithm, is the total energy of the system. A reasonable requirement of a good MD algorithm is then that the total energy of the system be conserved.[1]

Many factors influence the ability of an algorithm to do this, for example rounding errors when computers store floating point numbers, but one critical element in this consideration that the user can choose is the distance in time between calculations or the integration length, called the timestep size Δt which determines the resolution of the simulation. The strong repulsion at very short distances means that if atoms are allowed, by a large timestep size, to move very close together before the forces on them are recalculated, unrealistic dynamics will follow. Choosing a small Δt generally yields more accurate results but comes at the price of increased computational expense. Deciding a suitable timestep size is largely an empirical matter based on trial and error, but an educated guess may be made by considering the elements of the simulation — heavier elements do not require as small Δt as light elements do. The important thing is that Δt should be of such a magnitude that the vibrations between atoms can be resolved, which in most cases means that $\Delta t \approx 1\,\text{fs}$ is a good choice. To illustrate the idea, we briefly introduce a commonly applied integration algorithm.

1 This is of course only true in the simplest case, the microcanonical ensemble. Ensembles of constant temperature are mentioned below.

The Verlet algorithms

A popular integration algorithm is the Verlet algorithm [94]. From a basic Taylor expansion of the position $\mathbf{r}$ of all atoms around the time t one has

$$\mathbf{r}(t+\Delta t) = \mathbf{r}(t) + \mathbf{v}(t)\Delta t + \frac{\mathbf{a}(t)}{2}\Delta t^2 + \frac{\mathbf{j}(t)}{6}\Delta t^3 + \mathcal{O}(\Delta t^4) \tag{2.10a}$$

$$\mathbf{r}(t-\Delta t) = \mathbf{r}(t) - \mathbf{v}(t)\Delta t + \frac{\mathbf{a}(t)}{2}\Delta t^2 - \frac{\mathbf{j}(t)}{6}\Delta t^3 + \mathcal{O}(\Delta t^4), \tag{2.10b}$$

where $\mathbf{r}(t)$, $\mathbf{v}(t)$, $\mathbf{a}(t)$, and $\mathbf{j}(t)$ are the positions, velocities, accelerations, and jerk (the rate of change of the acceleration) of all atoms at time t, respectively. By adding Eqs. (2.10a) and (2.10b) one obtains

$$\mathbf{r}(t+\Delta t) = 2\mathbf{r}(t) - \mathbf{r}(t-\Delta t) + \mathbf{a}(t)\Delta t^2 + \mathcal{O}(\Delta t^4), \tag{2.11}$$

which is the basic Verlet algorithm for advancing the positions of all atoms with time.

One of the strengths of the Verlet algorithm is that the error is of order Δt^4 even though third derivatives are not explicitly calculated. At the same time, the Verlet algorithm is exactly time reversible and stable, meaning that it closely follows the ideal system, and the total energy is not subject to a large drift even for long time scales, all of which makes the Verlet algorithm a popular choice.

In most practical MD simulations one is interested in the kinetic energy and temperature of the system. To calculate the kinetic energy, and from it the temperature, the velocities of the atoms are required. A problem of the basic Verlet algorithm is that velocities are not directly generated and require an extra calculation, for example $\mathbf{v}(t) = [\mathbf{r}(t+\Delta t) - \mathbf{r}(t-\Delta t)]/2\Delta t$ with an associated error of order Δt^2. A variant of the basic Verlet algorithm called the velocity-Verlet algorithm is therefore often used instead [95] and is the one used for all MD simulations in this thesis:

$$\mathbf{r}(t+\Delta t) = \mathbf{r}(t) + \mathbf{v}(t)\Delta t + \frac{\mathbf{a}(t)}{2}\Delta t^2 \tag{2.12a}$$

$$\mathbf{a}(t+\Delta t) = -\frac{1}{m}\nabla U(\mathbf{r}(t+\Delta t)) \tag{2.12b}$$

$$\mathbf{v}(t+\Delta t) = \mathbf{v}(t) + \frac{\mathbf{a}(t) + \mathbf{a}(t+\Delta t)}{2}\Delta t. \tag{2.12c}$$

The two algorithms give the same trajectories of the atoms but the velocity-Verlet algorithm is different in that it generates the velocities at each timestep. Additionally, it is not necessary to simultaneously store the positions of the atoms at two timesteps.

Note, that in Eq. (2.12b) the acceleration is found from the negative gradient of the potential $-\nabla U$. This is where the interatomic potentials, covered in the previous section, come into play.

2.1.3 Ensembles and statistical mechanics

The way to relate the microscopic properties of the system simulated with MD to macroscopic, thermodynamic properties is through statistical mechanics and the concept of statistical *ensembles*, which denotes the conceptual

collection of all available microstates of a system. If the system is isolated such that number of particles (N), volume (V), and energy (E) are kept fixed, then all available microstates will belong to the *microcanonical* ensemble (or, NVE ensemble) and the collection of all microstates of the system form the ensemble.

The fundamental assumption is that an isolated system in equilibrium in a given macrostate has an equal probability of being in any of the microstates corresponding to that macrostate. On this basis it can be shown that the entropy of an isolated composite system is maximum when the different parts of the system are in thermodynamic equilibrium which defines the concept of temperature as the quantity which is equilibrated in this case. The entropy S is defined as the Boltzmann constant times the log of the number of microstates Ω available to the system:

$$S = k_{\mathrm{B}} \ln \Omega \tag{2.13}$$

and it follows that an isolated system tends to maximize entropy which is realized when the number of available microstates is a maximum.

In a more realistic scenario the temperature (T) is kept fixed instead of energy and the system will be in the *canonical* ensemble (NVT) which corresponds to a system in contact with a heat bath. The probability $P(E_i)$ of being in a microstate i with energy E_i is given by the canonical distribution

$$P(E_i) = \frac{e^{-E_i/k_{\mathrm{B}}T}}{Z}, \tag{2.14}$$

where Z is the "partition function" which is the sum of all microstates

$$Z = \sum_i e^{-E_i/k_{\mathrm{B}}T}. \tag{2.15}$$

The partition function acts both as a normalizing factor for the probability of being in a given microstate and enters also in the definition of the concept of "free energy" which is discussed below.

Free energy

An important concept for the description of systems in contact with a heat bath is the "free energy" of the system from which several other quantities can be derived. The thermodynamic definition of the free energy F is

$$F = E - TS, \tag{2.16}$$

where E is the internal energy, T the temperature, and S the entropy of the system, as defined in Eq. (2.13). The equilibrium state of a system at temperature T is thus the state which minimizes the free energy. This implies that at low temperatures a system will tend to be in a state which minimizes its internal energy (as in a solid) whereas for high temperatures the system will tend to maximize entropy (as in a gas). The free energy is a useful descriptor of a system because changes in the free energy can be considered as the "driving force" which drives a system from one state to another more favorable state.

From a statistical mechanics point of view, the free energy can be related to the partition function by the relation

$$F = -k_B T \ln Z \tag{2.17}$$

and the free energy F_A associated with a subset A of the microstates is then given via the partition function Z_A which is the sum of the states relevant for that subset

$$Z_A = \sum_{i \in A} e^{-E_i/k_B T}. \tag{2.18}$$

Considering the microstates as dependent on a continuous distribution of the $3N$ coordinates of the N atoms of the system the partition function may be expressed by an integral over those of the coordinates that correspond to the microstate A

$$Z_A = \int_A e^{-E(\mathbf{r})/k_B T} \, \mathrm{d}^{3N}\mathbf{r}\,. \tag{2.19}$$

If the set of microstates A can be described as a region of space, say, when some molecule is located in the range of the z-coordinate between $z = a$ and $z = b$, then the integral can be rewritten as

$$Z_A = \int_a^b \mathrm{d}z \int \delta(z - z(\mathbf{r})) e^{-E(\mathbf{r})/k_B T} \, \mathrm{d}^{3N}\mathbf{r}\,, \tag{2.20}$$

where the delta function has the property that it picks out the coordinates which belong to a certain value of z. The latter integral can be redefined as $e^{-F(z)/k_B T}$ with $F(z)$ being the free energy as a function of the z-coordinate. The probability of finding the system at a given z-value is [96–98]

$$P(z) = \frac{e^{-F(z)/k_B T}}{Z} \tag{2.21}$$

and the total free energy F_A of state A is then given by

$$F_A = -k_B T \ln \int_a^b \mathrm{d}z \, e^{-F(z)/k_B T}. \tag{2.22}$$

This procedure will be applied in Chapter 4 to calculate the free-energy change associated with the adsorption of a PEG molecule to a gold surface.

2.1.4 Temperature control and Langevin dynamics

As discussed above the dynamics resulting from solving Newton's equations of motion correspond to having the system in the NVE ensemble and there is no immediate way to affect the temperature of the system. However, most real experiments either belong to the NVT ensemble or the NPT (constant pressure) ensemble, so in order to compare results from MD simulations with experiments we need some way to impose temperature and/or pressure control.

The *instantaneous* temperature of the system is found from the total kinetic energy of all atoms by use of the equipartition theorem, which states that the

kinetic energy will be shared equally among all atoms, such that the average temperature of the system T is given by

$$T(t) = \sum_{i=1}^{N} \frac{m_i v_i^2(t)}{k_B N_f}, \tag{2.23}$$

where i is the index of the N atoms in the system, m_i and v_i are the mass and velocity of atom i, respectively, k_B is the Boltzmann constant, and N_f is total the degrees of freedom of the system.

To control the temperature during MD simulations it is therefore necessary to modify the equations of motion according to which the system evolves to couple the system to a heat bath of a desired temperature. The most common way is to implement some variation of Langevin dynamics where the equation of motion takes the general form

$$m_i \mathbf{a}_i = \mathbf{F}_i - \gamma m_i \mathbf{v}_i + \mathbf{R}_i, \tag{2.24}$$

with $\mathbf{F}_i$ calculated as in Eq. (2.2), γ being a friction coefficient with units of inverse time which removes kinetic energy from the system, and $\mathbf{R}_i$ being a stochastic force which introduces energy to the system. The stochastic force term is proportional to the friction term and has a mean square given by

$$\left\langle \mathbf{R}_i^2 \right\rangle = 2 m_i \gamma k_B T_0, \tag{2.25}$$

where T_0 is the temperature of the heat bath to which the system is coupled.

The specific implementation of temperature control is referred to as the *thermostat* of the simulation and below a few of the well-known thermostats will be reviewed to illustrate the idea.

It should be mentioned for completeness that it is also common to find pressure control algorithms (*barostats*) to allow constant pressure simulations, for example in the grand canonical ensemble (NPT) although since all the simulations performed in this thesis were NVT simulations this concept will not be reviewed here.

Berendsen thermostat

One of the simplest thermostats is the Berendsen thermostat [99] which couples the system to a heat bath through purely frictional contact, meaning that $\mathbf{R}_i = 0$ in Eq. (2.24). The rate of change of the temperature is given by

$$\frac{dT}{dt} = \frac{1}{\tau}(T_0 - T), \tag{2.26}$$

where $1/\tau$ describes the strength of the coupling to the heat bath such that a large τ results in a weak coupling and thus a longer time is required to reach T_0. The Berendsen thermostat results in an exponential decay (or rise) of the system temperature towards the temperature of the heat bath and will therefore suppress fluctuations in the average temperature of the system. Such a system will not represent the canonical ensemble and it is therefore mainly useful to equilibrate the temperature to a heat bath after which another thermostat should be applied.

Andersen thermostat

Another relatively simple thermostat is the Andersen thermostat [100]. In this algorithm interaction with the heat bath is simulated without a friction term by stochastically rescaling the velocities of a random fraction of atoms every few timesteps to a Maxwell-Boltzmann distribution around the heat bath temperature. If ν is the frequency for the stochastic collisions of the atoms with the heat bath, and the collisions are uncorrelated, then the distribution of time intervals between successive collisions $P(t, \nu)$ is of the Poisson form

$$P(t, \nu) = \nu \exp(-\nu t), \tag{2.27}$$

where $P(t, \nu)\, \mathrm{d}t$ is the probability that a collision will happen in the time interval $[t, \mathrm{d}t]$. The strength of the coupling to the heat bath is adjusted by the collision frequency ν [80]. This method controls the temperature well and can be shown to produce the canonical ensemble, however, the stochastic changes in the velocities of the system lead to a discontinuous, non-physical evolution of the system.

Langevin thermostat

If the Langevin equation is applied with both the friction and stochastic term as given by Eq. (2.24) the result is the Langevin thermostat. In this situation all atoms of the system can be considered to be embedded in a sea of fictional particles which have a kinetic energy given by the heat bath temperature [101, 102]. When using the Langevin thermostat the coefficient γ in Eq. (2.24) denotes the inverse damping time which is the characteristic time of energy exchange between the atoms of the system and the heat bath. The choice of γ is important. A too small γ, meaning weak coupling, will lead to a poor temperature control and a long time will be needed to equilibrate to the target temperature (and for $\gamma = 0$, the NVE ensemble is realized, obviously with no temperature control), whereas a too large γ will cause the stochastic forces to dominate over the Newtonian dynamics. While momentum transfer is lost due to the stochastic collisions, as in the Andersen thermostat, the benefit of the Langevin thermostat is that it reproduces the canonical ensemble [101, 103].

The Langevin thermostat was available in the MBN Explorer package and was therefore used for all MD simulations presented in this thesis.

2.1.5 Other types of molecular dynamics

Besides the classical, atomistic MD described above, there are several other important types of MD simulations, which should be briefly described for the sake of completeness, namely *ab initio* MD (AIMD) and coarse-grained MD (CGMD). AIMD is the most precise method usable mostly for small systems while CGMD employs simplifications to allow enormous systems for extended trajectories.

Ab initio molecular dynamics

As mentioned in the introduction to Section 2.1 classical molecular dynamics makes use of the Born-Oppenheimer approximation to separate the nuclear dynamics from the electron dynamics which are parametrized by use of interatomic potentials. The most precise dynamical simulation of molecules is performed when, instead of using an interatomic potential parametrized for the system, the interatomic forces are derived on a quantum mechanical basis, usually using density functional theory, see for instance Refs. [104, 105] and references therein. Still making use of the Born-Oppenheimer approximation that the dynamics of the nuclei and the electrons can be decoupled due to the much faster electrons, the time-independent Schrödinger equation is solved as given by

$$\hat{H}(\mathbf{r}, \mathbf{R})\Psi(\mathbf{r}, \mathbf{R}) = E\Psi(\mathbf{r}, \mathbf{R}), \tag{2.28}$$

where $\hat{H}$ is the Hamiltonian of the system which depends on positions of all electrons $\mathbf{r}$ and all nuclei $\mathbf{R}$ of the system, $\Psi(\mathbf{r}, \mathbf{R})$ is the ground-state wave function of the system, and E is its total energy. Having calculated the energy of the system and considering it to be a function of the nuclear coordinates the forces are calculated from the gradient of the potential energy, as in classical MD. The positions of the atoms are then updated as described above, for example using the velocity-Verlet algorithm.

The benefit is that AIMD does not require the extensive fitting that is needed to prepare good interatomic potentials and as such may be performed on novel systems. In addition, chemical bonding is automatically accounted for in AIMD and accurate modeling of chemistry is therefore possible. Common to all of the AIMD methods is that the solution of the Schrödinger equation is computationally expensive for large systems and AIMD is therefore currently restricted to relatively small systems on the order of 10^3 atoms.

A full discussion of the topic of AIMD methods goes beyond the topic of this thesis. The interested reader is referred to reviews on the topic for example in Refs. [104, 105].

Coarse-grained molecular dynamics

Lastly the type of MD simulation known as coarse grained MD (CGMD) is briefly mentioned. In this kind of MD simulation several atoms are grouped together as one unit (a virtual atom), for example all functional groups on an amino acid or all water molecules. This procedure vastly reduces the degrees of freedom of the system compared to conventional all-atom simulations and therefore greatly increases the length of the trajectory and size of the system which it is possible to simulate in a given length of CPU time, for example several microsecond long trajectories and systems on the order of 10^6 atoms, see e.g. Refs. [106, 107] and references therein. The way to coarse-grain a given system determines how well the results can be related to atomistic simulations and real experiments but, if done well, large systems may be modeled effectively. Atomistic MD simulations are often performed in order to properly parametrize the CGMD potentials.

CGMD is performed mainly for biomolecular systems with examples including protein structure [107], cell membranes, and transport of molecules or NPs through cell membranes [108, 109]. CGMD can also be performed in combination with atomistic models in a procedure called hybrid all-atom/coarse grained molecular modeling, for instance by modeling all water molecules of a system as virtual atoms with the rest of the atoms modeled atomistically [110].

2.2 METADYNAMICS

In general calculating statistical ensemble averages from MD simulations can only be expected to give meaningful results if the resulting trajectory is long enough for the system to explore all relevant configurations. If these are separated by high free-energy barriers the configuration space may suffer from poor sampling — indeed the transition from one locally stable state to another may be such a rare event that it will in practice never happen during an MD simulation. For some biological processes such events may on average take place on the time-scale of milliseconds and since a typical MD simulation timestep is on the order of femtoseconds, this would require about 10^{12} simulation steps which is practically unfeasible. Regions in phase space separated by free-energy barriers are denoted "metastable" states and procedures for exploring them using MD simulations, generally known as "enhanced sampling techniques", are currently a hot topic. The interested reader is referred to the recent reviews on such techniques by Abrams & Bussi and Bernardi *et al.* [111, 112].

When studying the adsorption of molecules to a surface the desorption may never be observed during standard MD simulations if the binding energy is sufficiently strong. For this reason, a type of enhanced sampling known as metadynamics [73, 113] was performed to study the binding free-energy of poly(ethylene glycol) to gold in Chapter 4. An excellent review of this technique can be found in Ref. [74] and will be briefly summarized below.

2.2.1 The method of biasing the potential

In 2002, Laio & Parrinello published the method known as metadynamics (metaD) as a way to enhance sampling along selected "collective variables" and thus explore the full phase space more efficiently [73]. In metaD simulations, which are a variation of standard MD simulations, a history-dependent bias potential V_{bias} is added to the Hamiltonian of the system H

$$H = T + V + V_{\text{bias}}, \tag{2.29}$$

where T and V are the kinetic and potential energy components, respectively. The bias potential can be written as a sum of Gaussian potential hills along the trajectory of the collective variable (CV) in question. The CV is a general term and can refer to any selected degree of freedom of the system, for instance the distance between selected atoms, the position of selected atoms,

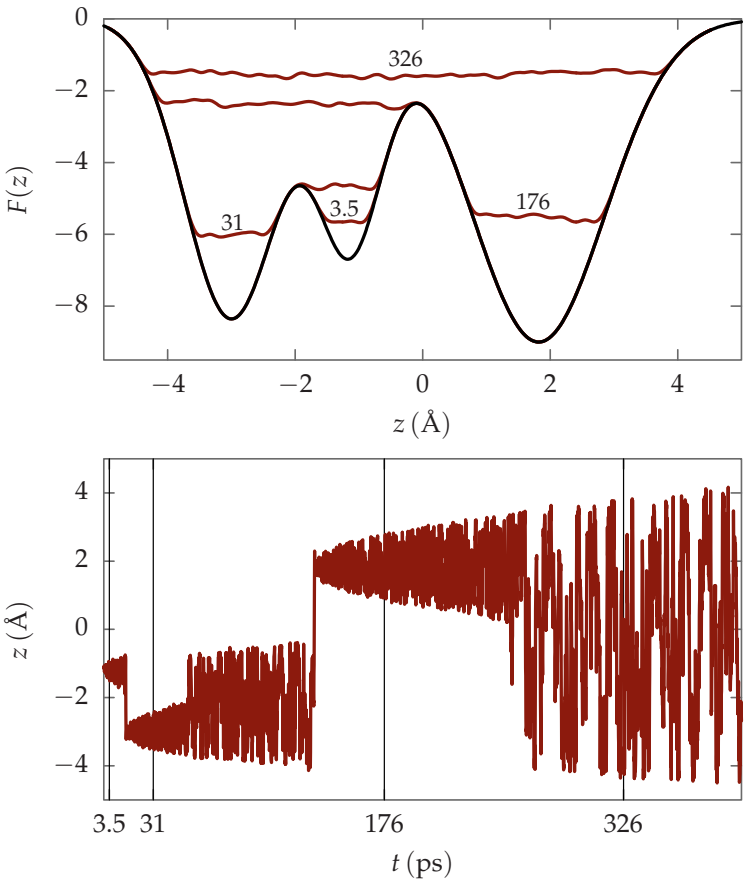

Figure 2.2: Example of a one-dimensional metaD simulation calculated using ATK-ForceField. (Upper) The free-energy profile $F(z)$ versus collective variable z shows the progressive filling of the potential (black line). Gaussian hills are added along the trajectory and their sums are shown with red lines at the indicated times. (Lower) The position of the collective variable z versus simulation time t.

bond angles, dihedral angles, and so on. By adding a bias potential along the previously visited trajectory the system is pushed out of any local potential minimum in which the system may be located with respect to the given CV. When a sufficient number of "hills" have been added, thereby increasing the local potential to the same height as the free energy barrier along the selected CV, the system is free to explore configurations which would otherwise be inaccessible.

An example of a metaD simulation of a particle moving in a one-dimensional potential landscape was calculated using ATK-ForceField [114] and is shown in Fig. 2.2. Comparing the upper and lower panels it is illustrated how the particle, initially located in a the shallow, central valley, is enabled to explore the other valleys one by one as the filling of the potential landscape progresses. In the end all potential valleys have been filled rendering the effective free-energy landscape flat enough so that the particle is free to diffuse in the whole range of z.

The bias potential is in general a function of a set S of CVs S_1 to S_d which in turn are a function of the configuration of the system R

$$S(R) = (S_1(R), \ldots, S_d(R)). \tag{2.30}$$

The bias potential at time t for the set of CVs S is then given by

$$V_{\text{bias}}(S,t) = \int_0^t \mathrm{d}t' \, \omega \exp\left(- \sum_{i=1}^{d} \frac{[S_i(R) - S_i(R(t'))]^2}{2\sigma_i^2} \right), \tag{2.31}$$

where $\omega = W/\tau_{\text{bias}}$ is an energy rate given by the Gaussian height W (with units of energy) and the deposition time interval τ_{bias} (with units of time) and σ_i is the Gaussian width of the bias potential hills for the i'th collective variable S_i.

In the case of the one-dimensional example, shown in Fig. 2.2, $d = 1$ and the collective variable $S(R)$ is the z-component of the position of the particle. Gaussian potential hills of height W and width σ are then added every $\tau_{\text{bias}}/\Delta t$ simulation steps (where Δt is the timestep in the simulation) along the z-direction of the trajectory. The parameters W, τ_{bias}, and σ are chosen before the simulation starts. Choosing suitable values requires some empirical knowledge of the system similar to choosing the timestep and thermostat parameters in ordinary MD simulations. By choosing large W, σ, or $1/\tau$ the bias potential is increased more rapidly, but the system will, at the same time, be farther from equilibrium due to the rapidly added perturbations. It is thus a compromise between efficient and reliable simulations, a recurring theme in MD simulations [74, 113, 115]. It should also be mentioned that there are no general recommendations for choosing suitable CVs and these are generally developed *ad hoc* based on experience and according to the process under investigation, e.g. the distance between the center of mass of two bonding molecules or the torsional angle in a molecule for studying conformations [74, 111].

If a novel system is under consideration one does not usually know the free energy landscape and the position of metastable states — after all if we did there would be no need to sample it anyway. Since the metastable states cannot be found using normal MD simulations one of the main benefits of metaD simulations is therefore that, under certain conditions, no prior knowledge of the free energy surface is necessary. This is because metaD simulations automatically explore low free-energy regions first which is in contrast to e.g. the umbrella sampling method, which requires some estimate of the free energy surface [73, 74]. In addition it can be shown that the accumulated bias potential converges to the real free energy surface $F(S)$ with opposite sign plus some arbitrary constant C [74, 115, 116]

$$\lim_{t\to\infty} V_{\text{bias}}(S,t) = -F(S) + C. \tag{2.32}$$

The result is that the potential energy surface becomes flat thus making all states in the CV-space equiprobable.

2.2.2 Well-tempered metadynamics

An inherent issue with metaD simulations is that it is in general difficult to determine when to stop the simulation. If one is interested only in surpass-

ing the nearest free energy barrier one should stop when this happens but, if the whole free energy surface is to be explored, the metaD algorithm will keep adding hills after all local minima have been visited which is called overfilling of the free energy surface. In this case the simulation may be stopped when the motion of the collective variable becomes diffusive, as shown in Fig. 2.2.

The tendency to overfill may be overcome with the introduction of "well-tempered" metaD simulations [113]. In these simulations, the Gaussian height W is decreased with simulation time

$$W(t') = W_0 \exp\left(-\frac{V_{\text{bias}}(S(R), t')}{k_B \Delta T}\right), \tag{2.33}$$

where W_0 is the initial Gaussian height, k_B is the Boltzmann constant, and ΔT is an input parameter with dimensions of temperature. In well-tempered metaD simulations the hills added at a given position of the CV will then have an exponentially decreasing height ensuring a converging bias potential with time. For $\Delta T \to 0$ the height of the hill vanishes and the result is an ordinary MD simulation whereas for $\Delta T \to \infty$ a normal metaD simulation is recovered. A choice somewhere in between will regulate how much of the free-energy surface will be explored and how quickly. If ΔT is too small the Gaussian height will decrease so fast that even the initial, local potential minimum will not be overcome whereas, for too large ΔT, the free energy profile may take an unnecessarily long time to converge.

With well-tempered metaD the converged bias potential does not fully correspond to the free energy surface of the system but converges to

$$V_{\text{bias}}(S, t \to \infty) = -\frac{\Delta T}{T + \Delta T} F(S) + C, \tag{2.34}$$

where C is an arbitrary constant.

The metaD simulations performed in Chapter 4 were of the well-tempered kind.

2.3 DIFFUSION

Particles whose motion are independent and governed by random collisions, which reset momentum after some characteristic distance, are said to be undertaking a "random walk" and the collective motion of a large number of such particles can be modeled in a relatively straightforward way as a diffusion process. It has been shown, by Surdutovich & Solov'yov, that the motion of low-energy electrons with energy below about 50 eV can be modeled as a diffusion process [77] and such a model is therefore applied in Chapter 5 for the transport of low-energy electrons emitted from a NP under ion-irradiation. In this section, the most important points about the theory of random walk and diffusion are briefly reviewed.

2.3.1 Random walk

To develop the theory of diffusion let us start by considering a one-dimensional process in which a particle can move left or right with equal

probability. If one supposes that the step length is L then position x_N after N steps is

$$x_N = k_1 L + k_2 L + \ldots + k_N L, \tag{2.35}$$

where k_j is the direction of step j which is equally likely to be ± 1. While the average displacement is clearly zero, because the average of every step is zero, it should also be intuitively clear that it is increasingly unlikely to end up at the initial position as N increases. We can reconcile this by considering the mean square displacement which is

$$\left\langle x_N^2 \right\rangle = \left\langle (k_1 L + k_2 L + \ldots + k_N L)^2 \right\rangle. \tag{2.36}$$

The square of the sum will result in N terms of the type $\langle k_j^2 L^2 \rangle$ and the rest will be of the type $\langle k_j L \times k_i L \rangle$. The former will be simply L^2 because $(\pm 1)^2 = 1$ while the latter will be zero because the average value of $k_j k_i$ is zero for k_j and k_i both equally likely to be ± 1. We therefore have

$$\left\langle x_N^2 \right\rangle = NL^2. \tag{2.37}$$

If the time between jumps is Δt we can redefine the number of jumps N made after time t as $N = t/\Delta t$. Defining the *diffusion coefficient* D as $D = L^2/2\Delta t$ we can then write the mean square displacement after time t as

$$\left\langle x_t^2 \right\rangle = 2Dt. \tag{2.38}$$

In two dimensions the average step length is $\sqrt{2}L$ while in three dimensions it is $\sqrt{3}L$ which results in a mean square displacement of $\left\langle x_t^2 \right\rangle = 4Dt$ and $\left\langle x_t^2 \right\rangle = 6Dt$ for a random walk in two and three dimensions, respectively.

Equation (2.38) is an important result because it allows for statistical predictions of a random process: Even though each jump is random we can, *on average*, expect the particle to arrive at position p after a time $t = p^2/2D$, even though p may be much larger than L. Figure 2.3 illustrates the result and shows the mean square displacement of a single random walk process and the average of 50 random walk processes versus the step number. It is clearly seen that one cannot predict the displacement of a single random walking particle but when averaging over many such particles a clear trend is seen.

2.3.2 Fick's law and the diffusion equation

If we imagine a large number of particles each doing a random walk independently then their individual motion can be described according to Eq. (2.38) but this does not tell anything about the overall distribution of particles which is usually more informative. If one instead monitors their density or concentration $c(\mathbf{r}, t)$ at position $\mathbf{r}$ at time t, it can then be shown that the flux of particles $\mathbf{J}(\mathbf{r}, t)$ is related to the gradient of the concentration as given by

$$\mathbf{J}(\mathbf{r}, t) = -D\boldsymbol{\nabla} c(\mathbf{r}, t). \tag{2.39}$$

This relation is known as Fick's first law of diffusion and states that diffusion will tend to even out any "structure" in the concentration because particles

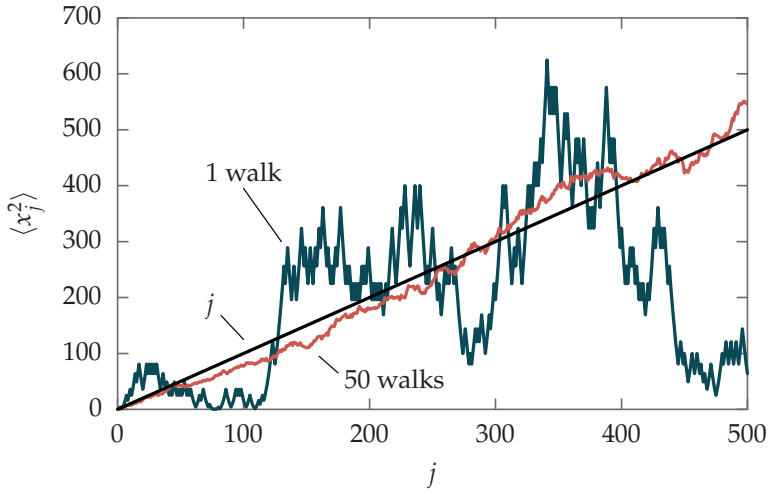

Figure 2.3: Mean square displacement $\langle x_j^2 \rangle$ versus step number j for a single random walk and for 50 walks of 500 steps with step length $L = 1$. Also shown is j itself.

will move from high concentration towards lower concentrations and that this will happen more quickly for faster diffusing particles.

This relation can be combined with the continuity equation, given by

$$\frac{\partial c(\mathbf{r}, t)}{\partial t} = -\boldsymbol{\nabla} \mathbf{J}(\mathbf{r}, t), \tag{2.40}$$

to obtain the general diffusion equation which relates the evolution of the concentration in time to its evolution in space and is, in the case of constant diffusion coefficient, given by

$$\frac{\partial c(\mathbf{r}, t)}{\partial t} = D \nabla^2 c(\mathbf{r}, t). \tag{2.41}$$

Depending on the geometry of the problem, as well as the initial and boundary conditions of the situation, the solution to the diffusion equation will take different shapes. In the simplest one-dimensional case, with all particles initially positioned at $x = 0$, the solution is a Gaussian profile given by

$$c(x, t) = \frac{N}{\sqrt{4\pi D t}} \exp\left(-\frac{x^2}{4Dt}\right), \tag{2.42}$$

where N is the number of particles initially at $x = 0$. This solution obeys the boundary conditions that the number of particles is constant in all space ($\int_{-\infty}^{\infty} \mathrm{d}x\, c(x, t) = N$) and that the number density far away from the origin vanishes ($\lim_{x \to \infty} c(x, t) = 0$). The solution is plotted in Fig. 2.4.

In Chapter 5, the diffusion equation is derived and solved for the emission of electrons from a spherical shell in the case where electrons are absorbed exponentially as a function of time due to inelastic scattering events.

2.3.3 Fluence

The fluence is the time integral of the flux and thus gives the number of particles which pass some distance per area. This is used in Chapter 5 to

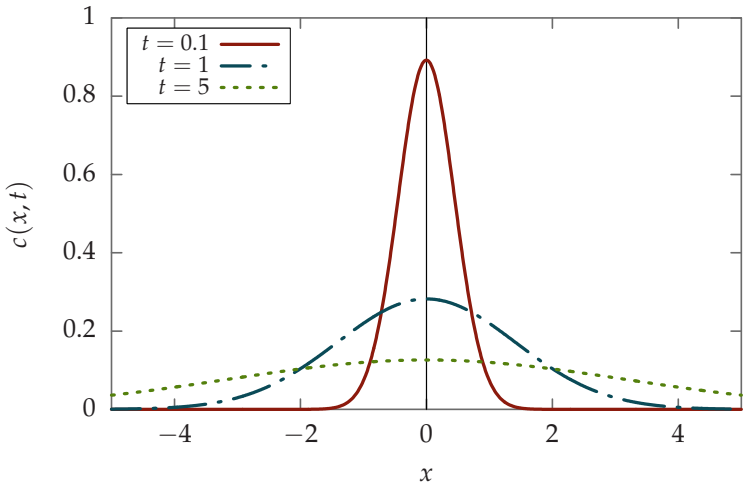

Figure 2.4: Gaussian diffusion profile showing the concentration $c(x,t)$ versus position x plotted for different times t in arbitrary units.

calculate the total number of electrons emitted from the NP surface which escape the coating. Considering the boundary of the coating as a concentric sphere with surface area A outside the NP core from which the electrons are emitted the number of electrons escaping the coating can be found by evaluating the *integral* fluence $F(r)$ at the end of the coating by integrating over the surface area A. The integral fluence (from here on just referred to as fluence) is defined as

$$F(r) = \int_A \mathrm{d}\mathbf{A} \int \mathrm{d}t\, \mathbf{J}(\mathbf{r},t), \tag{2.43}$$

where $\mathbf{J}(\mathbf{r},t)$ is the flux as given by Eq. (2.39). In the radially symmetric case, as in the diffusion of electrons from the surface of a NP, the area integral gives a factor $4\pi r^2$.

2.3.4 Other transport theories

It should be mentioned that calculating the transport of electrons is a wide field of research and may be modeled using a wide variety of frameworks. The study of electronic current in semiconductors, for instance, is an important topic for the design of modern transistors and may be modeled with *ab initio* models such as density functional theory (DFT) [117, 118] or with classical procedures such as Monte Carlo models [27, 119]. While the DFT frameworks work well for describing the transport of electrons in solids with high accuracy, these methods are much too computationally demanding for the situations we consider in the present thesis for which reason the diffusion model was applied.

2.4 USED SOFTWARE

For all MD simulations relating to the structure of the coating in Chapter 3, MESO BIO NANO EXPLORER (2.0) [101] was used. Coating and wa-

ter molecules were added using the software VISUAL MOLECULAR DYNAMICS[2] [120]. MARVIN SKETCH[3] was used to draw the coating molecules while VIRTUAL NANOLAB [114] was used for creating the metal cores of the NPs and for setting up the system simulated in Chapter 4 where ATK-FORCEFIELD [114] was used with the PLUMED[4] plugin [121] for all MD and metaD simulations. Lastly, MATHEMATICA[5] was used for the numerical calculations in Chapter 5 and GNUPLOT[6] [122] was used for all plots while INKSCAPE[7] was used for all illustrations presented in this thesis.

2 VISUAL MOLECULAR DYNAMICS 1.9.1, http://www.ks.uiuc.edu/Research/vmd/
3 MARVIN 15.4.27.0, 2015, ChemAxon, http://www.chemaxon.com/
4 PLUMED 2.2, https://plumed.github.io/
5 MATHEMATICA 11.1.1, Wolfram Research, Inc., (https://www.wolfram.com/mathematica/)
6 GNUPLOT 5.0, http://gnuplot.sourceforge.net/
7 INKSCAPE 0.92.2, https://inkscape.org/en/

3 STRUCTURE OF A MOLECULAR COATING ON A NANOPARTICLE

Two of the most important practical questions regarding the design of nanoparticles (NPs) for use in radiotherapy are: (i) how to ensure the arrival of the NPs to the tumor region and (ii) how to ensure a sufficiently long lifetime of the NPs that they are present during the subsequent irradiation [123, 124]. The first may be overcome by directly injecting the NPs into the tumor but when this route of administration is impractical it is necessary to ensure that intravenously injected NPs automatically find the tumor region in sufficient concentration. The second issue is two-fold and requires both that the NPs not disintegrate, aggregate, or otherwise lose their integrity and that the NPs not be removed from the blood stream by the immune defense system before reaching their intended destination. Additionally, the NPs should naturally also be radiosensitizing to be useful agents during radiotherapy treatment. These challenges involve the interactions between the NPs and their biological environment and researchers have discovered that these challenges can be met simultaneously by applying a coating layer to the NPs prior to administration, meaning a layer of molecules attached to the surface of the NP, most commonly consisting of poly(ethylene glycol) (PEG) [14, 53, 54, 125].

One of the characteristics of cancer tissue is that it forms new blood vessels to supply its growth, a phenomenon called angiogenesis. These blood vessels differ from those of healthy tissue in that they are leaky, meaning that there are pores in their walls. Additionally, tumor tissue has poor lymphatic drainage which leads to a retention of macromolecules that make their way there. These two features, the leaky, porous blood vessels and the increased retention has been named the "enhanced permeability and retention" (EPR) effect [7, 126]. Carefully designed PEG coatings, when used *in vivo*, prolong the blood circulation time of the NPs and through the EPR effect allow NPs to be taken up preferentially by cancer cells and to avoid adverse reactions from the immune defense system [14, 53, 54] but the ability of the coating to function according to the requirements mentioned above depends largely on the structure of the coating which is a complicated function of the surface density and length of the PEG molecules in combination with material, size, and shape of the NP core [55, 65]. The multiparametric nature of this problem makes it a highly complex task to investigate experimentally all possible combinations, both in terms of time and money required, and a complete understanding of the interplay of all factors has yet to be realized. This can be evidenced by the large variations in the experimental data reported to date [55]. The fact that these properties of the coating also impact the radiosensitizing abilities of coated NPs [33, 34] makes it all the more important to fully understand these mechanics and to be able to predict the structure of a proposed coating-core design.

In this chapter a new methodology to investigate, computationally, the geometry of the NP coating is presented and used to simulate the effect of coating surface density on the thickness of the coating. In addition the radial distribution of the elements of the coating is calculated and thereby a detailed description of the degree to which water is able to penetrate the coating as a function of surface density is evaluated since this has been proposed to be a determining factor for the radiosensitizing capabilities of PEG-coated NPs [34].

The characteristic length scales are of the order of a few nanometers with the number of atoms in the simulations being on the order of tens of thousands. This is important to consider because it puts constraints on the methods that can be applied to the problem. On one hand the complexity of the system in terms of size and number of atoms by far exceeds the practical limits of precise *ab initio* methods which explicitly treat the electron dynamics for the system. On the other hand we are not, for the purposes of this chapter, interested in the detailed electronic structure of the coating but seek a resolution on the level of individual atoms in order to monitor the conformation of the coating molecules and the degree to which the water solvent penetrates the coating. This makes classical molecular dynamics (MD) simulations a suitable approach to this problem and all simulations performed for the results presented in this chapter were thus performed using the software package MBN Explorer [101] with the CHARMM force field [90, 91]. The simulations were run on computer clusters at The Open University, Milton Keynes and at Goethe University, Frankfurt.

The chapter is outlined as follows: In the following section, the system under consideration in this chapter is presented. In Section 3.2 the procedure for creating the NP and the coating, how to attach the coating to the NP surface, and how to solvate the system in water is presented as well as how to obtain and prepare all the necessary input files for this kind of simulation. Section 3.3 presents how the simulations were carried out and in Section 3.4 the results are described, namely how the thickness of the coating depends on the surface density of the coating molecules and we calculate the radial distribution of the coating elements including the water content of the coating. The findings of this chapter are summarized and concluded in Section 3.5.

It is important to stress that this procedure is entirely system agnostic and may be applied to any combination of NP core and coating molecule provided that they can be accurately modeled with force fields. It is therefore also possible to extend the complexity of the model by including ions, proteins, or cell membranes to the simulation to approach a more realistic environment as experienced by a coated NP *in vivo*.

3.1 SIMULATED NANOPARTICLE AND COATING

Due to the wide variety of NP core materials and coating molecules there is practically an endless number of combinations which may be investigated. One of the most widely researched coating molecules is poly(ethylene glycol) (PEG) which is commonly used to coat gold NPs. PEG provides increased

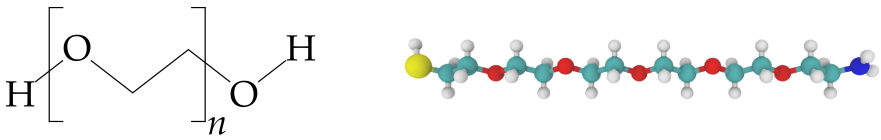

(a) (b)

Figure 3.1: (a) Chemical formula of the PEG molecule. (b) PEG molecule with thiol group on the left end and amine group on the right end. The colors indicate sulfur (yellow), hydrogen (white), oxygen (red), nitrogen (blue), and carbon (teal).

lifetime of the NPs in the blood stream and has been used for passive targeting since research on this type of coating started several decades ago [54, 55, 61, 127, 128], see Fig. 3.1 for an illustration of the PEG molecule. Much research has focused on studying the interactions of PEG-coated NPs with the biological environment and optimizing the design of PEG-coated NPs by tuning the length of the PEG molecules and their surface density both experimentally and theoretically, see e.g. Refs. [53, 60, 62, 129–131]. However, there is still disagreement in the field on the optimal method of measuring the coating surface density and thickness [55] which results in a wide variety of reported surface densities, see Table 3.1, and there is a need for more precise methods. We therefore simulate the combination of a PEG-coated gold NP (AuNP) with a diameter of the core of approximately 1.6 nm, corresponding to 135 atoms, to allow for experimental comparisons with another early stage researcher in the ARGENT project who has performed multiple experiments with PEG-coated AuNPs of similar dimensions at The Open University.

In the experimental community it is customary to classify different lengths of the PEG molecule by the molecular weight of the molecule, commonly in units of Daltons ($1\,\mathrm{Da} = 1\,\mathrm{g\,mol^{-1}}$). They usually range between 2 kDa to 20 kDa but can be as large as 50 kDa. In this project a relatively small PEG molecule of 0.27 kDa was used corresponding to five subunits of the polymer with a length of about 2.2 nm, which was also the size of PEG molecules used in experiments performed in the ARGENT project. The PEG molecule was functionalized at one end with a thiol group, which is the most common strategy for bonding to gold surfaces due to the relatively strong bond between gold and sulfur. On the other end the PEG molecule was functionalized with an amine group, again in accord with experiments performed in the ARGENT project. The rationale behind attaching an amine group to the PEG molecule has to do with the overall charge of the coated NP which will become slightly more positive with amine groups attached. This is thought to promote the uptake by cells due to their slightly negative membrane as demonstrated experimentally by Verma & Stellacci [134].

It should be mentioned, for the sake of completeness, that research into the design of coatings is an intense field of research by itself. The interested reader is directed to the reviews in Refs. [135–137].

Table 3.1: Summary of some experimentally estimated PEG coating surface densities θ for various AuNP diameters d and PEG weights W including what was used in this chapter.

d (nm)	W (kDa)	θ (nm^{-2})	Ref
15	2.1	3.93	[56]
	5.4	2.4	
	10.8	1.57	
	19.5	0.75	
	29.5	0.46	
	51.4	0.32	
30	10.8	1.29	
62.5		0.8	
93		0.96	
115		1.25	
30	2	9.2	[57]
	5	3.7	
	10	1.3	
	20	1.1	
60	1	1.4	[59]
	5	0.16	
	20	0.05	
17	5	0.85	[132]
2.8	5	2.9	[133]
1.6	0.27	0.5 to 7.5	This work

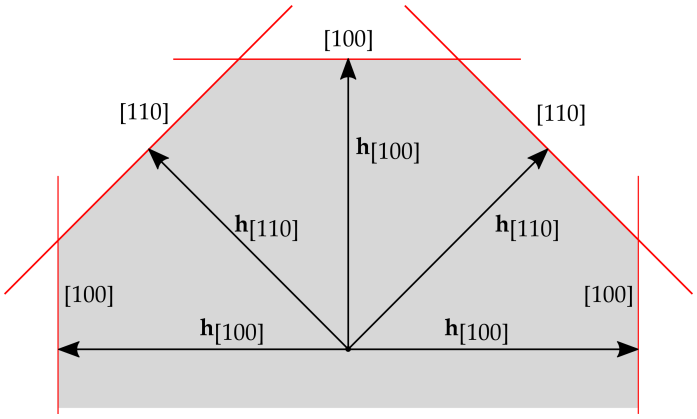

Figure 3.2: Wulff construction in 2D (only upper half shown). The nanoparticle (gray area) will be the smallest area enclosed by the red lines, see text.

3.2 PREPARATION OF SAMPLES

A well-prepared sample is a prerequisite for extraction of useful results from simulations and the sample preparation can take a considerable amount of time. In the present context "samples" refers to the NPs with or without coating, water solvation etc., and the "preparation" refers to generating the necessary files needed for the simulations and performing preparatory simulations. The preparation steps for the coated NP system are as follows: (i) definition of the NP core structure, (ii) definition of the coating, (iii) attachment of the coating to the NP surface, (iv) solvation of the system, (v) annealing and energy minimization, and finally (vi) equilibration of the system. At this stage the system will be ready for the simulations from which results can be extracted.

3.2.1 Definition of nanoparticle

The NP core was created using the software VIRTUAL NANOLAB [114]. As part of my work at QuantumWise, one of the available plugins used for creating the NP core was refined and updated (see also Appendix B). The plugin builds the NP using the so-called the Wulff Constructor which is a simple theoretical framework for deciding the area of each facet of the crystal based on the surface energy of the given facet [138]. The idea is that the length of a vector $\mathbf{h}_j$, drawn from the center of the NP normal to crystal face j, will be proportional to the surface energy γ_j of the face: $|\mathbf{h}_j| \propto \lambda\gamma_j$, where λ is a constant which scales the overall volume of the NP. In a similar fashion to the creation of the primitive Wigner-Seitz cell, well known from solid state physics, the NP will be the smallest volume enclosed by the facets drawn normal to, and at the end of, the mentioned vectors, see Fig. 3.2 for a 2D example. In the present case surface energies of equal magnitude were used which results in an NP as close to spherical as is possible with this method. While this procedure provides only a rough approximation to the true NP shape at such small sizes, the precise shape of the initial NP is not crucial due to the subsequent annealing after which the initial crystal structure will be lost.

3.2.2 Preparation of coating files

A prerequisite for performing computational modeling of coatings is to get the right structure files of the coating molecules and a description of the interactions between its constituents, i.e., the correct parameters for the force fields. In this work the CHARMM force field [90, 91] was used to describe the interactions of the PEG molecule, as detailed below. To perform MD simulations with this force field using the MBN EXPLORER software package, a number of specific files are necessary as input. Due to several competing conventions on how to format such files it is not always straightforward to convert between them in the way required by the simulation software to be used. The procedure to obtain these files in the format necessary for the present simulations is described in a six-step process[1] illustrated in the flowchart in Fig. 3.3 and with more details explained below.

1. Obtain `mol2` file for the PEG molecule from a molecule drawing software. Alternatively many molecules can be found in online databases.
2. Upload the `mol2` file to the SWISSPARAM website to obtain `pdb` file for the PEG molecule.
3. Upload the `mol2` file to the CGENFF website to obtain `str` file for the PEG molecule. Check the option to "Include parameters already in GCenFF".
4. Split the `str` file into an `rtf` file and an `inp` file.
5. Add nonbonded interactions from CHARMM library files to the `inp` file.
6. Run the built-in VMD plugin `psfgen` using the `pdb` file from the SWISSPARAM website along with the `rtf` files from the CHARMM library and from the `str` file from the CGENFF website to generate the `psf` file and an updated `pdb` file with corrected format.

In step 1 the software MARVIN SKETCH[2] was used to draw the molecule and obtain its structure in the `mol2` file format. Several similar types of software exist and common to all of them is that they have a built-in database of the possible bonds and angles between different atoms which allows for the drawing of any molecule. Alternatively the file may be directly downloaded from a database such as the ZINC database[3] which hosts the coordinate files for a vast collection of molecules and one can freely download their corresponding configuration in a number of formats.

The `mol2` file was then uploaded to the SWISSPARAM website[4] [139] in step 2 to convert it to the `pdb` format which is the format used to describe the atomic coordinates when running MD simulations with the CHARMM force field. There are many ways to convert between these two file formats but the

1 Adapted from the tutorial given here: http://alma.karlov.mff.cuni.cz/bio/99_Studenti/2015_2016/Charamza_Lukas/vmd_ligand.doc — Accessed Jan 30, 2018.
2 MARVIN 15.4.27.0, 2015, ChemAxon, http://www.chemaxon.com
3 http://zinc.docking.org/
4 http://www.swissparam.ch/

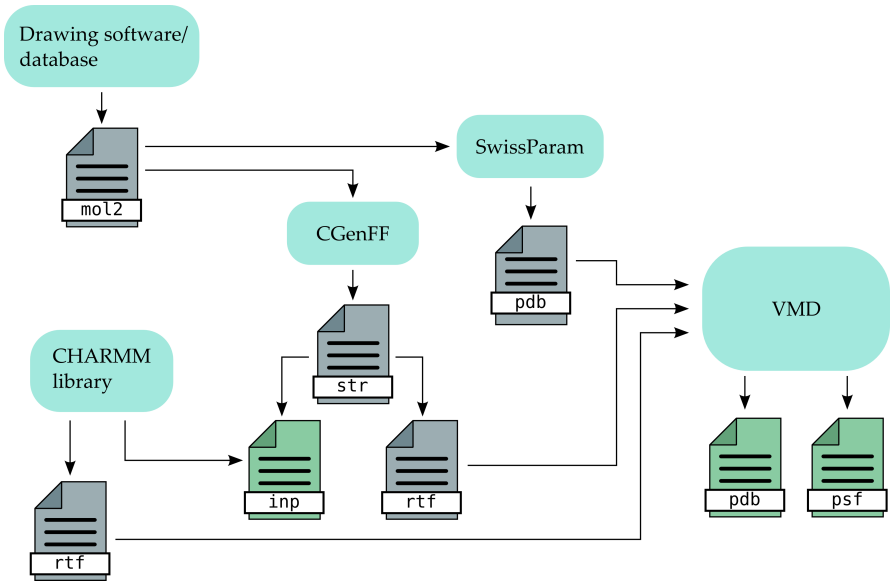

Figure 3.3: Flowchart illustrating the file preparation procedure. The gray files are intermediate files while the green files will be input to the MBN software during simulation.

SwissParam site is specifically optimized to work with the CHARMM force field and is therefore suitable for the present purposes.

In step 3 the `mol2` file from step 1 was uploaded to the CGenFF website[5] which generates a "stream file" containing the topology (partial charges and list of bonds, angles, and dihedrals) and the force field parameters for all atom types of the configuration based on the CHARMM force field library. The website interprets the environment of each atom from the `mol2` file and compares it with the CHARMM molecule library. Based on this information it assigns partial charge and bond information for each atom and outputs this in a `str` file.

This file needs to be split up for further use so in step 4 the `str` file was divided up into `rtf` and `inp` files. Since nonbonded force field information is not automatically added to the `inp` file this was done manually in step 5 by reading through the nonbonded section of the CHARMM parameter library[6] and adding to the `inp` file all the nonbonded entries which apply for the atom types found in the current molecule.

Finally, in step 6 the built-in plugin `psfgen` from the program VMD was executed to produce the `psf` file and a modified `pdb` file. It takes as input the `rtf` file produced in the previous step, the `rtf` file from the CHARMM library, and the `pdb` file produced in step 2.

This completes the procedure of generating the files necessary for running MD simulations using MBN Explorer with the CHARMM force field (the resulting `pdb`, `psf`, and `inp` files are listed in Appendix D). The same procedure can be conveniently followed for preparing simulations with the CHARMM force field of any other organic molecule.

5 https://cgenff.paramchem.org/

6 The topology and parameter files needed can be found here: http://mackerell.umaryland.edu/~kenno/cgenff/program.php — Accessed Jan 30, 2018.

3.2.3 Adding the coating to the nanoparticle

When creating the coating from the prepared molecule files three choices must be made: (i) How densely to pack the surface of the NP with coating molecules, (ii) where to place the molecules on the surface of the NP, and (iii) how to define the bond between the NP surface and the coating molecules. Regarding (i), the surface density of coating molecules simulated in this project was selected as a range based on experimental values found in literature [56–59, 133], as summarized in Table 3.1. For a core of diameter 1.6 nm this range of densities correspond to between 4 and 60 PEG molecules.

For the second question the point of attachment of the PEG molecules to the AuNP surface must be decided. When dealing with nanoscopic structures the precise topology of a surface is important because the local electronic structure depends strongly upon it. This means that corners and edges of a NP have different reactivities than flat crystal faces — an effect exploited in catalysis, for example — and this will result in an uneven distribution of the coating molecules [140, 141]. As a first approximation this fact was disregarded in the present study and the PEG molecules were attached evenly on the surface of the AuNP in such a way as to ensure approximately equal distances between the PEG molecules. This was done because the AuNP surface structure was disorganized after annealing simulations and there was therefore no clear definition of faces or edges.

Finally, regarding (iii) only a small selection of metals are parametrized in the CHARMM library which primarily contains parameters for biological molecules. This means that the parameters of the bond between metals and coating molecule have to be either calculated using quantum chemistry methods or parametrized using some other reference. However, for the purposes of the simulations performed in this chapter the bond strength was not important since the focus was on interaction of the tails of the PEG molecules and the resulting overall structure of the coating and its permeability to water and because breaking and formation of bonds was not simulated. The Au–S bond was therefore parametrized using a simple Lennard-Jones potential with equilibrium bond length set to 3.0 Å as an average between the reported values for this bond in Refs. [142] and [143]. A bond strength of 3 eV was used but, since the bond is unbreakable in the currently used force field, this plays a minor role. A more careful modeling of this bond is performed in Chapter 4 where the binding free energy of PEG on a gold surface is studied using the GoLP-CHARMM extension to the CHARMM library [143] for a well-adjusted parametrization of the gold-sulfur bond. This was impractical for the simulations in this chapter, however, because the GoLP-CHARMM extension should be used for flat gold surfaces.

The sulfur atom of the terminating thiol group of the PEG molecule is passivated by a hydrogen atom which, in experiments, will detach upon bond formation with the gold surface [144, 145]. Since the force fields used do not allow for bond formation and breaking this hydrogen atom was removed manually from the structure files. To ensure a neutral total charge in the system the partial charge associated with the removed on the hydrogen atom q_{H} was then applied evenly to the gold atoms of the AuNP such that every

gold atom of the NP was assigned a partial charge of $q_{Au} = N_{PEG}q_H/N_{Au}$, where N_{PEG} is the number of attached PEG molecules and N_{Au} is the number of atoms in the AuNP. This procedure assumes, to a first approximation, that there will be no significant charge reorganization of the PEG molecule due to the hydrogen dissociation and bond formation and that the partial charge of the hydrogen atom will be fully transfered to the AuNP. While the CHARMM force field does not include charge recalculations this could, in principle, be implicitly taken into account with *ab initio* MD simulations, but that is beyond the scope of this study and it is assumed that the partial charges near the sulfur atom have only a small effect on the conformation of the overall PEG molecule and resulting coating structure.

3.2.4 Solvation of coated nanoparticle

To approximate the environment experienced experimentally by NPs inside a cell the coated NP was solvated using the VMD software, meaning that water molecules were added to the system.

The water added in a simulation is often referred to as the "water box". The size of the water box can be chosen freely as long as it is big enough to fully contain the coated NP with the additional requirement that the distance from the coating to the wall of the water box be large enough that the coated NP not interact with its own periodic image when performing the simulation with periodic boundary conditions. The distance from the coating to the wall of the water box is referred to in the following text as the "padding". One method to decide on a padding thickness is to evaluate the Coulomb interaction between a given atom of the coating and the nearest mirror image atom and compare this energy E_C to the thermal energy of the water box k_BT at the temperature of the system with the understanding that the Coulomb interaction can be safely ignored if $E_C \ll k_BT$. This comparison is done in the next section. As will be explained in Section 3.3.2 an additional factor for choosing the padding was that the density of water resulting from using the VMD plugin did not correspond to water at atmospheric pressure at room temperature. Since MBN Explorer does not allow for pressure equilibration simulations a water box was created with a thick padding from which a smaller box could be cut out after density equilibration in vacuum.

The interactions of the water molecules are defined by the chosen "water model", which is a set of parameters designed to yield realistic macroscopic properties such as boiling temperature and density. In this project we used the TIP3P water model [93] which is supported by the used CHARMM force field.

The finished initial structure for the case of $N_{PEG} = 32$ is shown in Fig. 3.4.

3.3 SIMULATIONS

When performing MD simulations it is necessary to ensure that the simulated systems are properly equilibrated thermally before any results can be

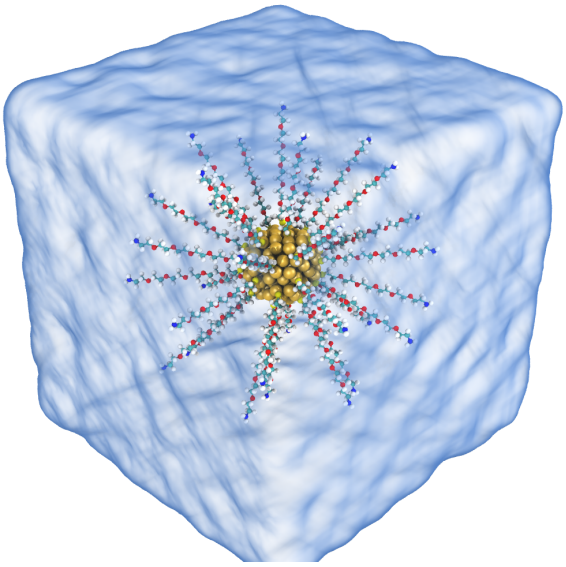

Figure 3.4: AuNP coated with 32 PEG molecules attached before simulations are carried out.

meaningfully extracted (not considering nonequilibrium situations which may also be studied). In this section the simulations performed to equilibrate the system and the final annealing simulations, from which results are extracted, are described. The equilibration stage consisted of a series of energy minimization and equilibration simulations: First, the naked metal core of the NPs was optimized by annealing, then the coating was applied and the system solvated after which an energy minimization was performed on the whole system. Afterwards, the solvated system was equilibrated and then the final annealing simulations were carried out. All simulations are performed using MBN Explorer [101].

3.3.1 Annealing of nanoparticle core

A widely used method to geometrically optimize structures is annealing. This method is originally an experimental technique used in metallurgy to minimize imperfections due to lattice mismatches when a layer of one material is deposited on top of another but the procedure is essentially the same when used in simulations. The process consists of first heating up the sample, then keeping the temperature elevated for a period of time before slowly cooling the sample down. The procedure of keeping an elevated temperature for an amount of time followed by a slow cool down is designed to allow atoms trapped in a local minimum in the potential energy surface to escape and find a lower optimum.

Ensuring that the final configuration is the global minimum is a nontrivial problem when the number of atoms exceeds a few tens since for a NP comprising just 100 atoms the number of local minima is estimated to be on the order of 10^{43} [146]. Analyzing all of the configurations is obviously impossible however it is not required in the present analysis that the system be in the global minimum, a reasonably optimized structure will do. To eval-

uate how well the final configuration has been optimized the total energy of the system was compared with the theoretical predictions provided by the liquid drop model which describes the total internal energy E_N of a NP comprising N atoms in terms of volume energy, surface energy, and curvature energy

$$E_N = -\lambda_V N + \lambda_S N^{2/3} - \lambda_R N^{1/3}, \tag{3.1}$$

where λ with the subscripts V, S, and R denote the contributions to the total energy from volume, surface, and curvature, respectively [147]. A fit based on this model is used below to evaluate configurations obtained after annealing.

The annealing procedure of the NP core was the following:

1. Thermalize at 300 K for 50 ps to stabilize the system.
2. Heat up to 1400 K and maintain this temperature for a total of 400 ps.
3. Cool down to 0 K in steps of 100 K per 50 ps.

The temperature was controlled with the Langevin thermostat, see Eq. 2.24, using a damping time of $1/\gamma = 0.2$ ps, the timestep was $\Delta t = 1$ fs, and the Sutton-Chen force field was used with parameters for gold as given in Ref. [88] for the Au–Au interactions. To plot the total energy as a function of number of atoms a range of sizes was simulated having sizes between 10 and 4501 atoms corresponding to a diameter of up to approximately 5 nm for the largest size.

The total energy per atom was calculated for AuNPs comprising between 10 and 4501 atoms. The energies were compared with a fit based on the liquid drop model Eq. (3.1) to global minima of AuNPs with between 10 and 80 atoms taken from the Cambridge Cluster Database[7] (CCB) which is an online database of global minima calculated for many different systems of nanoclusters, the results are presented in Fig. 3.5. It is seen that the calculated energies $-E_N/N$ are slightly lower than the values predicted by the liquid drop model. This is natural since it cannot reasonably be expected to arrive at the global minimum using a simple annealing procedure. However, the general trend of the calculated energies is similar to the theoretically predicted trend which indicates that the dynamics of the simulated NPs follow the expected behavior and it can therefore be assumed that the NPs, after annealing, are in a configuration relatively close to the global minimum.

At this stage the coating was applied to the surface of the NP and the system was ready for solvation and further equilibration.

3.3.2 Energy minimization and equilibration of coated nanoparticle

Before the final annealing simulations were performed an energy minimization of the systems of solvated and coated AuNPs was performed, then an equilibration simulation of the water density, and then another energy minimization before the final annealing simulations were carried out. The details of this procedure are described below.

7 http://www-wales.ch.cam.ac.uk/CCD.html

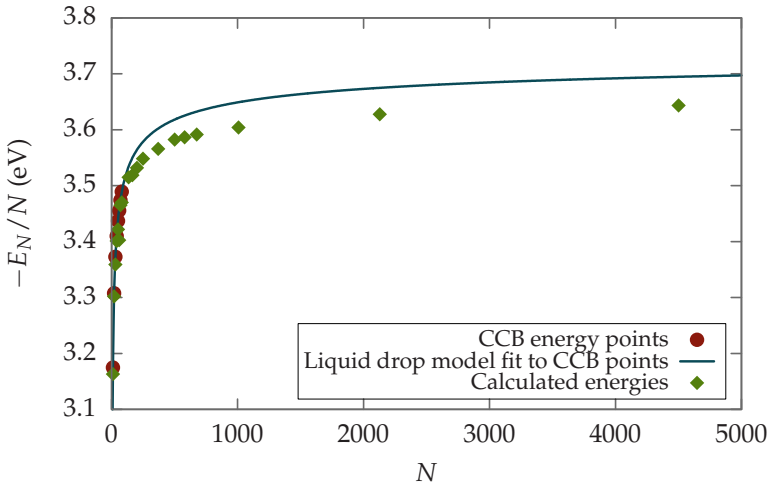

Figure 3.5: The total energy per atom $-E_N/N$ versus number of atoms N in AuNPs at the end of an annealing simulation with N varying between 10 and 4501 atoms as well as a fit of Eq. (3.1) to the CCB data points.

Energy minimization

Energy minimization is the process in which atoms are gradually moved from their initial positions until the total force on each atom is below some threshold value. The aim of such an optimization is not to find global minima but to approach a reasonable starting point for a MD simulation. Energy minimizations are also used to avoid overlapping atoms or atoms with very small distances between them, which could cause the system to explode or otherwise misbehave due to the strong repulsion at small distances.

The energy minimizations performed in this chapter employed the velocity quenching optimization algorithm included in MBN Explorer with a timestep of $\Delta t = 0.1\,\text{fs}$. In this method the kinetic energy is monitored for each particle as their positions are advanced using the chosen timestep. When the kinetic energy reaches a maximum, implying that the particle is in a potential minimum, the velocity of the particle is set to zero. In this way the potential energy of the system is gradually absorbed. The optimization was performed until the force on each particle was below a defined threshold of $\epsilon_\text{F} \approx 8 \times 10^{-16}\,\text{N}$ or after a maximum number of optimization steps of 20 000.

Equilibration of water density

As mentioned in Section 3.2.4, the density of the water box created by VMD did not have the correct density comparable with experiments at room temperature and atmospheric pressure. Since constant pressure simulations were not available with MBN Explorer the density was equilibrated in the following way, illustrated in Fig. 3.6:

1. Making a water box larger than what is needed for final simulations.
2. Equilibrating the water box in vacuum until a constant water density is obtained.

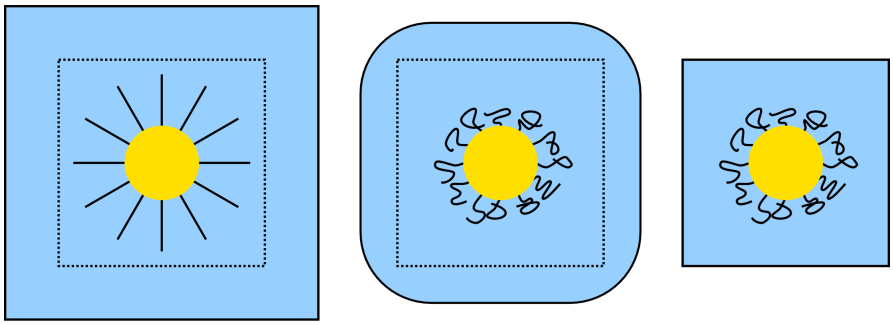

(a) (b) (c)

Figure 3.6: Illustration of the water density equilibration procedure as described in the text. (a) The dimensions of the water box are chosen such that a smaller box (dashed lines) can be cut out from its interior while still ensuring that interactions between atoms across the periodic boundary when using this box will be negligible. The water box for the equilibration is larger than this to allow the water density to equilibrate. (b) After the equilibration simulation in vacuum the water density is increased leading to a shrinking of the whole system and a rounding of the outer water box corners. The PEG molecules are coiled up further increasing their distance to the water box walls. (c) The final system is cut out from the equilibrated system (dashed lines in (b)) to be used in subsequent simulations.

3. Cutting out the interior of the equilibrated water box to use for subsequent simulations

These simulations are intended to simulate a coated NP in bulk water and it is therefore important that the coating atoms closest to the boundary do not interact with coating atoms of the periodic image. The size of the final water box to be used in subsequent simulations is therefore chosen such that the distance between a nitrogen atom (which is the outermost atom of the PEG molecules and also the one with highest partial charge and therefore largest interaction energy) and another periodic image nitrogen is at least 20 Å which requires a water padding of 10 Å in the initial structure. The Coulomb interaction energy E_C at this distance between two nitrogen atoms in water at 310 K is given by

$$E_C = \frac{k_C q_N^2}{r \epsilon_r} = 5.4\,\text{meV}, \tag{3.2}$$

where $k = 1/(4\pi\epsilon_0) = 8.99 \times 10^9\,\text{N}\,\text{m}^2\,\text{C}^{-2}$ is the Coulomb constant, $q_N = -0.775\,|\text{e}|$ is the partial charge on the nitrogen atoms, $r = 20\,\text{Å}$ is the distance between them, and $\epsilon_r = 80$ is the relative permittivity of water at room temperature. This result should be compared with $k_B T$ at 310 K which is approximately 27 meV. Since E_C is significantly lower than $k_B T$ the Coulomb interaction between the atoms is negligible compared to the thermal energy of the atoms so this is a sufficient water padding. In practice the distance between the edge of the coating and the nearest image will be larger than 20 Å because the PEG molecules will tend to coil during the simulation thereby increasing their distance to the boundary of the simulation box, as illustrated in Fig. 3.6 (b).

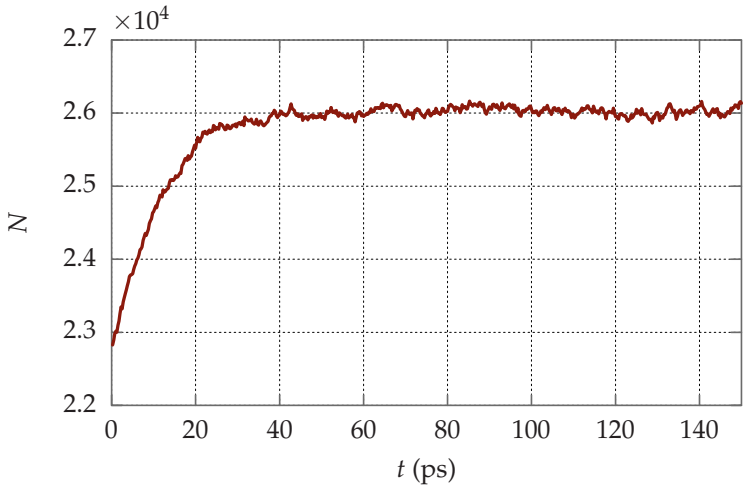

Figure 3.7: Number of atoms N in the volume, denoted by dashed lines in Fig. 3.6, versus time t for the equilibration simulation of $N_{\mathrm{PEG}} = 32$.

A cubic water box equilibrated in vacuum will tend to form a spherical droplet to reduce its surface area. This is inconvenient when performing MD simulations with periodic boundary conditions because this will lead to regions of vacuum in the corners so the water box cannot be used immediately after the density equilibration. Therefore a water padding of 20 Å was added initially which allowed for the extraction of a smaller rectangular box with an effective padding of 10 Å without rounded corners after the density equilibration.

With the dimensions of the water box determined the density equilibration was performed using a timestep of $\Delta t = 1\,\mathrm{fs}$ for a total duration of 400 ps. The temperature of 310 K was controlled by the Langevin thermostat, with a damping time of $1/\gamma = 0.2\,\mathrm{ps}$. To ensure a converged water density the number of atoms inside the volume, which would be cut out after the equilibration, was monitored during the simulation to make sure that it stabilized around a constant value. The result of one example system is presented in Fig. 3.7 which shows that the density of water molecules converged after about 40 ps.

Finally, the water box (illustrated by dashed lines in Fig. 3.6 (b)) was cut out from the interior of the equilibrated water box and an optimized with periodic boundary conditions using the velocity quenching algorithm.

3.3.3 Annealing simulation of coating structure

The simulations of the coating structure were performed as an annealing procedure consisting of a constant temperature simulation at 700 K for 400 ps followed by a gradual cooling down to 400 K in steps of 100 K per 100 ps and the final step from 400 K to 310 K also in 100 ps.

After the annealing simulations were carried out a clear change in the structure of the coating was observed, as seen in Fig. 3.8 which shows a coated AuNP with $N_{\mathrm{PEG}} = 32$ after annealing and cooling down to 310 K (compare with Fig. 3.4). The main difference is that the PEG molecules have

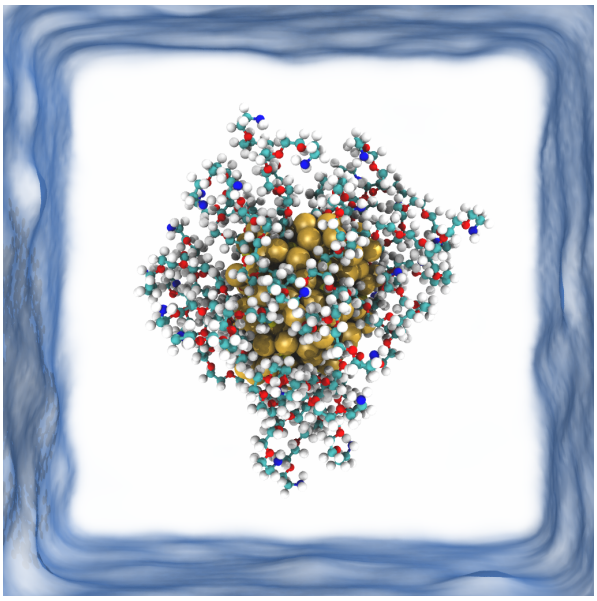

Figure 3.8: AuNP with $N_{PEG} = 32$ after optimizations, equilibration, and final annealing simulations as described in the text.

all coiled up to varying degrees resulting in a more compact structure. The details of the coating structure are analyzed below.

3.4 RESULTS AND DISCUSSION

Two main properties of the coating structure are analyzed: The thickness of the coating and the radial distribution of the elements of the coating medium including its water content — both as a function of the number of coating molecules N_{PEG}. The relationship between coating thickness and coating surface density will be compared with a commonly used theoretical framework for predicting the thickness of a polymer attached to a flat surface. The thickness and the degree of water penetration will be discussed in light of the potential use of the coated NP as a radiosensitizer which is the topic of Chapter 5.

3.4.1 Coating thickness

The thickness of the coating is important for a number of reasons. The size of the NP affects the uptake into cells as well as the blood circulation time which is an important part of the tumor targeting capabilities of NPs, as discussed in Chapter 1. The coating thickness can influence the radiosensitizing properties of NPs by affecting the distance secondary electrons emitted from the NP surface, as well as radicals produced inside the coating, have to travel before they escape the coating. This is important for estimating the total number of radicals produced by NPs under radiation which is predictive for its radiosensitizing abilities. Being able to accurately predict the size of a given combination of NP core and coating molecule, as well as the coating's

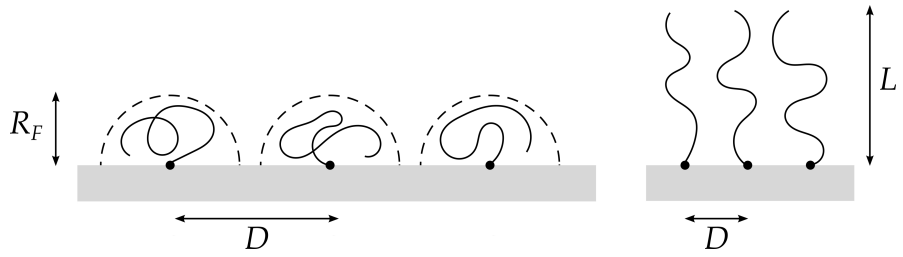

Figure 3.9: Illustration of (left) the mushroom and (right) the brush regime of polymer conformation realized when the distance between attachment points D is larger or smaller than the Flory radius R_F, respectively.

water content, is therefore an important tool for efficiently synthesizing NPs for medical use.

To evaluate the conformation of polymers attached to a surface and the resulting thickness of polymer coatings it is customary to apply the theoretical framework detailed by de Gennes [66]: For polymers in good solvents (solvents in which the polymers act like free chains) two regimes are defined, the first being the low-density regime where the surface density of the attached polymers is so low that the polymers are essentially isolated and free to coil around themselves without interacting with any neighboring molecules. Freely suspended in a liquid, a polymer tends to form a spherical "blob" whereas polymers attached to a surface tend to form a semi-spherical "mushroom" shape, see Fig. 3.9. The mushroom regime is realized when the average distance D between polymer attachment points is larger than the Flory radius R_F of the resulting mushroom given by [148]

$$R_F = a\mathcal{N}^{3/5}, \tag{3.3}$$

where a is the monomer length and $\mathcal{N}$ is the number of monomers in the polymer. In the mushroom regime the thickness of the coating L will be equal to the Flory radius R_F.

In the high-density regime, realized when $D < R_F$, the repulsive interaction between the closely spaced polymers cause them to attain a more linear shape stretching up from the surface and this is therefore referred to as the "brush" regime, see Fig. 3.9. The resulting coating thickness L is given by [66]

$$L = \mathcal{N}a\left(\frac{a}{D}\right)^{2/3}. \tag{3.4}$$

The distance between attached molecules D can be calculated by approximating the AuNP as a spherical particle with diameter d and surface area $S = 4\pi(d/2)^2$. Further approximating the average surface area per molecule $A = S/N_{\mathrm{PEG}}$ as circular, D is then the diameter of this circle

$$D = 2\sqrt{\frac{S}{\pi N_{\mathrm{PEG}}}} = 2\frac{d}{\sqrt{N_{\mathrm{PEG}}}}. \tag{3.5}$$

It follows, by insertion of Eq. (3.5) into Eq. (3.4), that $L \propto N_{\mathrm{PEG}}^{1/3}$:

$$L = \mathcal{N}a\left(\frac{a}{2d}\right)^{2/3} N_{\mathrm{PEG}}^{1/3}. \tag{3.6}$$

With these approximations, and using for the simulated PEG molecule $\mathcal{N} = 5$ and $a = 0.35\,\text{nm}$ [56] with with the NP diameter $d = 1.6\,\text{nm}$, the transition from mushroom to brush regime should happen around $N_{\text{PEG}} = 12.1$ where $D = R_{\text{F}} = 0.92\,\text{nm}$.

To evaluate the thickness of the coating from the simulations the starting and ending points of the coating are defined. Due to the initial annealing simulations the gold core was not perfectly spherical, so the beginning of the coating was defined as the average distance of the sulfur atoms to the center of mass of the system, $\bar{r}_{\text{S}}$. The end of the coating was defined as the distance from the center of mass inside which 97 % of the PEG molecules resided, $r_{97\%}$. The thickness of the coating t_{coat} is then $t_{\text{coat}} = r_{97\%} - \bar{r}_{\text{S}}$. The results are shown in Fig. 3.10 which presents the measured coating thickness t_{coat} as well as the Flory radius R_{F} based on Eq. (3.3) and the theoretical brush thickness L based on Eq. (3.4). In addition, the average distance between the sulfur and the nitrogen, that is, the average end-to-end distance of the PEG molecules $\bar{r}_{\text{S-N}}$, for each case of N_{PEG}, is shown to illustrate the degree of coiling of the PEG molecules for each coating density. As can be seen from the figure, t_{coat} does not follow the trend predicted by either of the regimes mentioned above and instead fluctuates between around 1.3 nm and 1.45 nm. In the highest coating density at $N_{\text{PEG}} = 60$, where $D = 0.41\,\text{nm}$, well below the Flory radius, the thickness is virtually the same as in the lowest coating density where $D = 1.6\,\text{nm}$ which is significantly larger than R_{F}.

To probe how coiled the PEG molecules are we can compare the average end-to-end distance $\bar{r}_{\text{S-N}}$ with R_{F}. The fact that the end-to-end distance is larger than the Flory radius, but not as large as the coating thickness, indicates that the PEG coating considered here is in a mixed state between mushroom and brush. The results agree with experimental measurements of coating thickness carried out by Tsai *et al.* who found that even for high PEG coating surface densities the brush regime is realized primarily near the NP surface, while a coiled conformation was seen for the outer portion of the PEG coating [59]. For *in vivo* applications it has been suggested that the optimal conformation is indeed one which is between brush and mushroom [149, 150] since this is associated with a larger permeability to water which is important for its ability to increase their lifetime and stability.

To explain why the results diverge from the theory of de Gennes, it is useful to recall that the framework of de Gennes is based on a couple of assumptions, most importantly that the polymer chain is long and that the surface is flat. The discrepancy between the observed coating thickness and the predictions is most likely not due to the short chain length, however. Zimmt *et al.* have shown that a Gaussian spatial distribution, which is assumed for the framework by de Gennes, is still a valid description for polymers with as few as three monomers [151]. Instead it is likely the shape of the surface that is the most important factor. Despite the mushroom and brush regimes being defined only for flat surfaces, this framework is commonly applied for coatings on spherical NPs, see e.g. Refs. [55, 56, 58]. In the present study, a AuNP with diameter 1.6 nm was simulated which means that the surface is highly curved and that will lead to a significantly reduced steric repulsion between the PEG chains compared to a flat surface with similar coating surface density. This effect has been confirmed experimentally [62] and the-

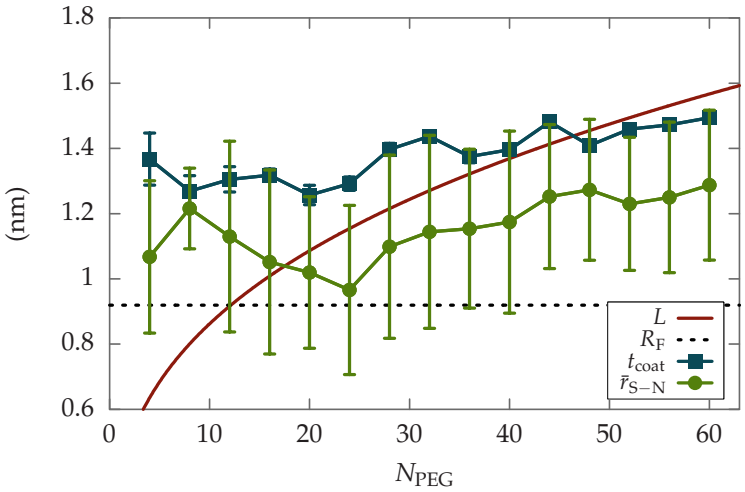

Figure 3.10: Theoretical brush regime thickness L (Eq. (3.4)) as well as the thickness of the coating t_{coat} versus the number of attached PEG molecules N_{PEG}. Also shown are the average end-to-end distance $\bar{r}_{S-N}$ for each value of N_{PEG} and the Flory radius R_F (Eq. (3.3)). The standard deviation is shown by vertical bars.

oretically [152, 153]. The framework may be refined to take into account the effect of the curved surface, although that goes beyond the scope of the work presented here. The most important conclusion is then, that the de Gennes framework cannot naively be used without further modifications for a precise prediction of the thickness of a polymer coating on small spherical NPs.

It should be reiterated that the applied force field was chosen based on its accurate parametrization of the interactions between organic molecules. The lack of precise interaction parameters for the PEG–Au interactions will likely play a negligible role for high coating surface densities where the PEG molecules are largely hindered from interacting with the NP surface, but for the low surface densities, it is possible that a more precise parametrization of the PEG–Au interactions will result in different conformations and therefore different coating thicknesses in this regime. In Chapter 4 the more detailed force field CHARMM-GoLP was applied to accurately model the PEG–Au interaction. This force field can only be applied for adsorption of molecules to flat surfaces so could not be used for the simulations presented in the present chapter, and the current force field was applied as an approximation.

3.4.2 Radial density distribution of coating

As mentioned in the previous section, one of the desirable properties of a PEG coating is that it be permeable to water. This is believed to be a deciding factor in its ability to function as a stabilizer and repellant of blood serum proteins, the two most important reasons why PEG is used as a coating molecule in the first place [69, 129, 154]. In addition it has been suggested, based on experiments, that coatings permeable to water allow for the greatest radical production during irradiation [34], a critical part of radiosensitization by NPs.

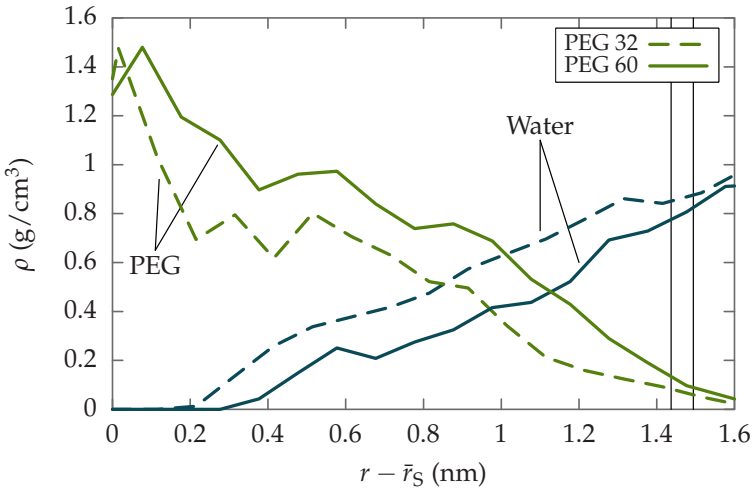

Figure 3.11: Radial density distribution ρ of the coating medium for $N_{\mathrm{PEG}} = 32$ and $N_{\mathrm{PEG}} = 60$ versus distance from the beginning of the coating $r - \bar{r}_{\mathrm{S}}$ showing both the density of the PEG molecules and the water content in the respective coating. The vertical lines on the right denote the coating thickness t_{coat} for 32 and 60 PEG molecules attached (in order from the left), respectively.

To gain more insight into the details of the coating structure, including the water content, the radial density distribution was calculated for different surface coating densities. By counting the number of atoms in concentric shells of thickness $\Delta r = 1.0\,\text{Å}$ around the center of mass of the system the radial density distribution function was obtained. Multiplying the number of atoms in the i'th shell by their atomic weight and dividing by the volume of the i'th shell $V_i = \frac{4}{3}\pi((i\Delta r)^3 - ((i-1)\Delta r)^3)$, the radial density distribution was obtained. The results for $N_{\mathrm{PEG}} = 32$ and $N_{\mathrm{PEG}} = 60$ are shown in Fig. 3.11.

The trend is that the density of the coatings increases with N_{PEG} which leads to a lower degree of water penetration and extends the region near the surface of the NP which is completely devoid of any water.

3.5 CONCLUSION

In this chapter, the structure of PEG-coated AuNPs was studied for varying coating surface densities by attaching between 4 and 60 PEG molecules of five monomers to a 1.6 nm diameter gold core. It was found that the thickness of the coating was fluctuating between around 1.3 nm and 1.45 nm with no clear dependence on the coating surface density which is in contrast to the prediction of the framework of de Gennes for the conformation of polymers attached to surfaces which is commonly used in literature to study PEG coatings on AuNPs. This is most likely due to the curvature of the NP surface in our work which allows the PEG molecules to coil even in the highest surface densities considered thus reducing the thickness of the coating. The PEG molecules were found to be in a conformation state between mushroom and brush — the two extremes predicted by the frame-

work for low and high surface densities, respectively. This is in accordance with experimental findings [59] and is indeed suggested as the preferable conformation for a PEG coating which should both permeable to water in order to protect the NP [149, 150].

However, to be a good radiosensitizer the PEG coating should be permeable to water all the way to the NP surface [34]. This was investigated by taking a detailed look on the internal composition of the coating medium by calculating the radial density distribution for $N_{\mathrm{PEG}} = 32$, and $N_{\mathrm{PEG}} = 60$. In this view the degree to which water was able to penetrate the coating was shown and it was clearly seen that increasing the coating surface density decreased the amount of water in the coating. For both cases of 32 and 60 PEG molecules attached the region immediately outside the NP (the first about 0.3 nm) was completely devoid of water with a slightly larger water-free region in the case of 60 PEG molecules attached. The consequence of this lack of water near the NP surface is investigated in Chapter 5 where the radical production is quantified as a function of coating structure.

The permeability of the PEG coating to water is an important property for the reasons mentioned above and the presented framework may therefore serve as a useful means of evaluating the structure of PEG coating with a given surface density.

4 CALCULATION OF BINDING FREE-ENERGY OF PEG TO GOLD

The radiosensitivity of nanoparticles (NPs) is strongly dependent upon the structure and composition of any coating that they may have [33, 34]. In Chapter 3 the structure of poly(ethylene glycol) (PEG) coatings on gold NPs (AuNPs) was studied as a function of the number of attached PEG molecules and it was shown that, for PEG molecules composed of five subgroups attached to a AuNP of diameter 1.6 nm, the thickness of the coating was independent of the number of attached PEG molecules within the range of 4 to 60 PEG molecules. In contrast the amount of water present in the coating depended on the number of PEG molecules attached: As the surface density of attached PEG molecules increases the ability of the surrounding water to penetrate the coating decreases leading to a region completely devoid of water near the NP surface for high coating surface densities.

The permeability of a coating to water is therefore a key property for a PEG coating to effectively protect the NP *in vivo* [69, 129, 154]. It has been suggested that coatings which are too dense for water to reach the NP surface may adversely affect the radiosensitizing abilities of the NP [34] and since the number of attached coating molecules partly determines the water content of a PEG coating and, in turn, its radiosensitizing properties, it is important to estimate and control this number during the synthesis of NPs.[1]

Several previous studies have focused on the parameters that govern how PEG coatings are formed and this has proven to be a highly complex problem. First, the synthesis process is dependent on a large number of parameters, e.g. the length of the coating molecules, their concentration in solution during synthesis, the size of the NP, the temperature and salinity of the solvent, and duration of the process [69, 129, 154]. Second, it is hard to verify the result of the synthesis because of the difficulty in measuring the number of molecules on the surface of the NP or, equivalently, the surface density of coating molecules. Table 3.1 summarized a number of experimentally estimated surface densities for PEG on AuNPs and one of the striking features of this table is the range in densities reported, which is partly due to the lack of accurate, standard methods for measuring the surface density of an attached molecule. Finally, the bond between gold and sulfur is surprisingly complex, making a detailed theoretical calculation of coating formation on gold surfaces a highly nontrivial exercise, see e.g. Refs. [141, 155] and references therein.

In addition to the need for understanding the precise structure of the PEG coating, it is necessary to gain information about the lifetime of the coating *in vivo*. Research has shown that PEG-coated NPs *in vivo* experience a gradual exchange of their coating molecules with more prevalent proteins found in the biological environment, such as the molecule glutathione [71, 72]. This

1 In Chapter 5 the effect of the water content of the coating on the radiosensitizing ability of the NP will be investigated.

exchange is dependent on the binding energy of the two kinds of molecules and an accurate calculation of the energetics of the PEG-coating formation may provide insights into both the optimal number of molecules on the surface of an NP and the lifetime of the resulting coating.

In this chapter two different methods to analyze the energetics involved in the binding of PEG on gold are presented. In the first method the adsorption and desorption processes are simulated using the metadynamics (metaD) technique which yields the free-energy profile associated with the adsorption of a PEG molecule onto a gold surface. In the second method a semi-analytical estimate of the free-energy change associated with the binding of a PEG to the surface is made by making a theoretical estimate of the entropy change and calculating the potential energy change with molecular dynamics simulations. Here the metadynamics value is used as a reference value to assess the accuracy of the semi-analytical approximation.

The chapter is outlined as follows: In the following section, the simulated system is presented together with the force field which was used for all simulations performed in this chapter. In Section 4.2 the metaD approach to the free-energy estimate is presented while in Section 4.3 the semi-analytical approach is presented. A summarizing conclusion of the two approaches is given in Section 4.4.

4.1 SYSTEM AND FORCE FIELDS

To enable a comparison between the two methods employed in this chapter the calculations are performed on the same system using the same force fields which are discussed below.

4.1.1 System geometry

Calculating the binding free-energy associated with forming a PEG coating is a complex matter. In nature one can imagine the first few PEG molecules that attach to the NP surface being essentially noninteracting with each other but as more molecules attach a monolayer will begin to form and new PEG molecules have to penetrate the layer of already attached molecules. This may lead to reorganization of the attached molecules to reduce the average repulsion between them and here the exact surface morphology of the NP core will play a significant role, as has been demonstrated experimentally and theoretically [65, 156, 157].

To tackle the complexity of this problem a step-by-step approach is used starting from the simple problem of a single molecule on a flat surface. The complexity can later be gradually increased by introducing more than a single adsorbed molecule and finally transferring the protocol to NPs. The situation is therefore initially simplified by considering a single PEG molecule adsorbing on a flat (111) gold surface in a water medium and we discuss how this method may be extended to the case of a spherical NP. The system was set up using VIRTUAL NANOLAB [114] with the dimensions of the gold slab being $34.6\,\text{Å} \times 30.0\,\text{Å}$ in cross-sectional area and about $18\,\text{Å}$ thick. A

water layer of about 82 Å was added on top of the Au slab with a density of about 1 g cm^{-3}. These dimensions ensured that the PEG molecule would not interact with its own periodic image no matter the conformation.

The PEG molecule was identical to the one used in Chapter 3 and consisted of five monomers with an amine group at one end and a thiolate group at the other end. The procedure of acquiring the necessary input files was the same as explained in Section 3.2.2.

When a thiol group binds to a gold surface the thiol group becomes a thiolate group due to the dissociation of the S–H bond [144, 145]. However, the used force field used did not allow for modeling of chemistry and the situation was therefore approximated without the S–H dissociation in this chapter.

4.1.2 Force field

For the simulations performed in this chapter the GolP-CHARMM force field was used to model the interaction between the gold surface and the PEG molecule and water medium [143]. This force field combines the GolP force field, which is parametrized for the adsorption of organic molecules to gold surfaces [158], with the CHARMM force field [91]. For the water–water interactions the TIP3P water model was used [93] while the gold atoms were kept fixed to reduce the complexity.

The simulations for this chapter were carried out using ATK-ForceField (2017.1) [114] and implementing the GolP-CHARMM force field for this software was a significant part of the work for this study. For the metadynamics simulations the PLUMED plugin version 2.2 [121] was used within ATK-ForceField. This is an extensive library of functions and tools to perform metadynamics simulations which is integrated in ATK-ForceField as well as in other major MD codes.

Below the two main innovative features of the GolP and GolP-CHARMM force fields are briefly introduced, namely the concept of virtual sites and image charges, which were both implemented in the ATK-ForceField code for the first time as a part of the research done for this chapter.

Virtual sites

The parametrization of the GolP force field was based on DFT studies which found that thiol groups bind more favorably to top sites[2] compared to hollow or bridge sites of Au (111) and (100) surfaces [143, 158]. A simple pair potential tends to favor hollow binding sites so to alleviate this, and reproduce the top site binding while still using classical pair potentials, "virtual sites" were added to the gold surface layer in the hollow sites of the gold atoms, see Fig. 4.1 (a). Pair interactions between the original surface gold atoms and the rest of the system were switched off and were instead applied to the virtual site gold atoms Au_{vs} using a Lennard-Jones interaction potential (see Eq. (2.4)). Since the hollow site of the virtual atoms correspond

2 In the context of adsorption of molecules to surfaces "top" refers to binding on top of a surface atom, "bridge" refers to binding between two atoms, and "hollow" refers to binding in the middle of three or more atoms.

Table 4.1: Parameters for Lennard-Jones interactions between atoms of the PEG molecule and either virtual site gold atoms or bulk gold atoms. Combinations not listed here were calculated based on combination rules as given by Eqs. (2.9a) and (2.9b) using the parameters for Au listed in the last row.

	ϵ (kJ mol^{-1})	σ (Å)
Au–N	0.90	2.90
Au–S	3.20	2.85
Au–O	0.70	3.10
Au–H	0.28	2.70
Au	0.48	3.80

to the top site of the original atoms the correct bonding geometry is recovered.

Parameters for the bond between Au_{vs} atoms and the elements H, O, S, and N atoms of the PEG molecule were taken from [143], see Table 4.1. For the C atoms of PEG, as well as the H and O atoms of the water molecules, the Lennard-Jones parameters were found from the combination rules as given by Eqs. (2.9a) and (2.9b) using values for ϵ and σ taken from the CHARMM library [91] with those for gold taken from the last row of Table 4.1. The Au atoms beneath the surface layer make only a small contribution to the interaction with adsorbed molecules and it is therefore not necessary to discriminate between the parameters for virtual sites and bulk Au atoms [143, 158]. For both virtual site Au and bulk Au atoms, values for ϵ and σ were therefore identical and are given in the last row of Table 4.1.

Image charges

The polarization of gold atoms upon binding of molecules to the surface has been shown by DFT calculations to be an important effect [159, 160]. Polarization is not trivial to take into account using classical force fields but Iori & Corni made a simple approximation [160], which was introduced in the GolP-CHARMM force field, in order to include polarization in classical MD simulations. They included a dipole effect by bonding a "dummy atom" through a stiff harmonic bond to each gold atom and then adding a positive charge q to the dummy atom and the opposite charge $-q$ to the host atom which results in a freely rotating dipole on each gold atom. The dynamics of the dipole can be adjusted by setting the mass m of the dummy atom as well as the equilibrium distance l_0 between the host gold atom and the dummy atom. Fig. 4.1 (b) illustrates this concept. The parameters used were $q = 0.3\,|e|$ and $m = 0.5\,$amu for the charge and the mass of the dummy atom, respectively, and $l_0 = 0.7\,$Å for the equilibrium distance as recommended in the original publication of the concept [160].

The implementation of virtual sites and image charges with the parameters given leads to binding energies for hollow, bridge, and top sites that are in good agreement with DFT simulations for a number of alkanes and peptides [143, 158]. The approach of adding virtual sites and simple dipole approximations through dummy atoms has the benefit that it can be included

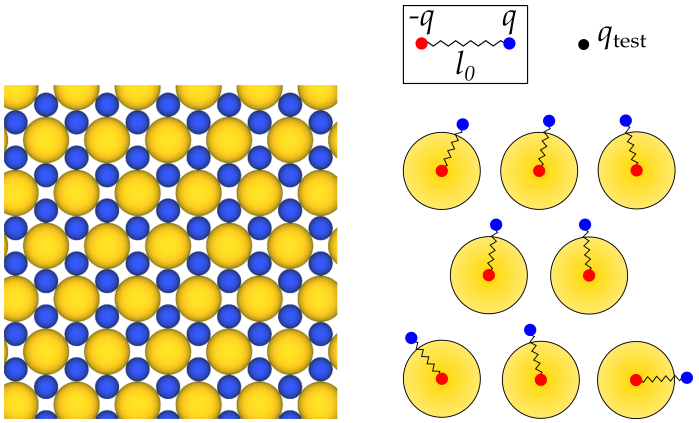

Figure 4.1: (a) Virtual sites (blue atoms) are added in the hollow sites formed by the gold atoms (yellow atoms) in the surface layer. (b) Dipoles are included by adding a dummy atom (blue) tightly bound to the center (red) of each host atom (yellow) with equilibrium distance l_0. The dummy atom and host atom are given opposite charges, q and $-q$, and the dummy atom can freely rotate thus mimicking a dipole. Illustrated is the partial orientation of the dipoles induced by test charge.

in the standard force fields for biomolecular systems which are available in almost all MD simulation codes simply by modifying the configuration and does not require a complicated implementation of the actual virtual site and image charge concept in the code itself.

4.2 ESTIMATE OF FREE ENERGY WITH METADYNAMICS

When calculating adsorption free-energy differences from MD simulations a common approach is to use the probability ratio method [96–98]. Here the exponential relationship between the probability of a state and the associated free energy (see Eq. (2.21)) is exploited by defining the free-energy difference as

$$\Delta F = -k_{\text{B}} T \ln \frac{P_{\text{ads}}}{P_{\text{sol}}}, \tag{4.1}$$

where P_{ads} (P_{sol}) denotes the average probability density or concentration in the adsorption region (in bulk solution) as given by

$$P_{\text{sol}} = \int_{\text{sol}} \mathrm{d}z \, \frac{P(z)}{Z} \tag{4.2}$$

$$P_{\text{ads}} = \int_{\text{ads}} \mathrm{d}z \, \frac{P(z)}{Z}, \tag{4.3}$$

where the adsorbed region (solution region) is the range in the z-coordinate which corresponds to the bonded state (solution state) to be defined below. Note that the partition function Z cancels out in the ratio of probabilities in Eq. (4.1) and thus does not have to be evaluated.

Table 4.2: Parameters used for the metaD simulations.

Parameter	Value
W_0	20 meV
σ	0.2 Å
τ_{bias}	200 fs
T	300 K
ΔT	300 K

Metadynamics settings

Metadynamics (metaD) simulations can be used to directly calculate the free-energy profile for a chosen collective variable from which the free-energy change associated with the binding can be calculated.

The simulations were performed for a total trajectory of 17 ns which was enough to result in a converged free-energy surface in the bulk region of the water medium. The simulations were performed as NVT simulations with temperature control provided by the Langevin thermostat (see Eq. 2.24) with the temperature of the heat bath set to 300 K and the damping time $1/\gamma = 0.1$ ps.

The well-tempered metaD bias was applied to the sulfur atom of the PEG molecule in the z-direction normal to the gold surface. The metaD parameters used for the simulations are summarized in Table 4.2.

4.2.1 Results

In Fig. 4.2 the z-position of the center of mass of the PEG molecule is shown as a function of simulation time, it is seen that the PEG molecule diffuses between $z = 0$ Å and $z \approx 35$ Å. The position $z = 0$ Å corresponds to the middle of the water region where a "wall restraint" was applied using the PLUMED plugin to restrict the phase space only to the part relevant for adsorption to one of the surfaces, which increases the efficiency of the metaD simulation. Since the simulation box is symmetric around $z = 0$ Å the transition from bound state to bulk state can thus effectively be sampled twice as fast without loss of generality. The position of the center of mass around $z = 35$ Å corresponds to the case when the PEG molecule is bonded to the gold surface.

The PLUMED program provides a convenient functionality to convert the output where all the Gaussian hills are added along the trajectory into information on the free-energy landscape. In Fig. 4.3 the free-energy landscape associated with the z-position of the sulfur atom of the PEG molecule is shown. The relatively flat free energy from $z = 0$ Å and $z \approx 19.5$ Å indicates a converged free-energy landscape and that the PEG molecule is noninteracting with the gold surface in this region. Between 19.5 Å and 36.4 Å the free energy is decreasing due to interaction between the "tail" of the PEG molecule with the gold surface which leads to an unstable "semi-bonded" state. Finally, a narrow valley in the free-energy surface is seen between 36.4 Å and 38.6 Å which is the position of the bonded state where the sulfur

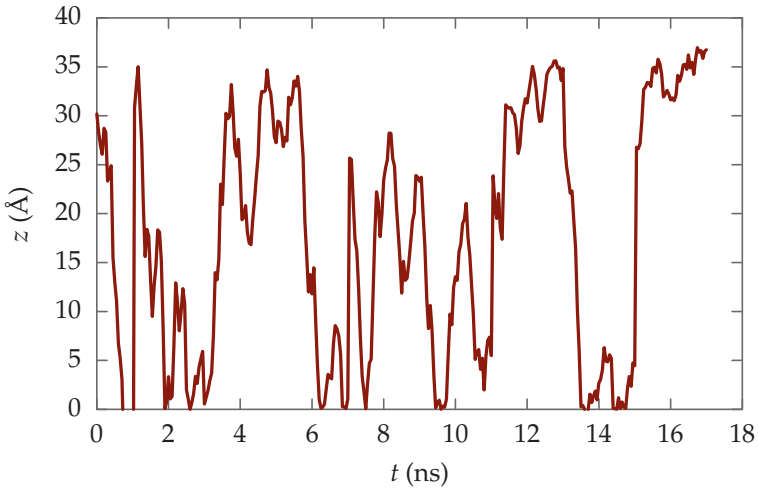

Figure 4.2: The z-position of the center of mass of the PEG molecule versus simulation time t.

atom is bonded to the gold surface. In the semi-analytical approach, discussed in Section 4.3, only the nonbonded and bonded states are simulated and so to make the two approaches more comparable, the metastable state, where the tail of the PEG is interacting with the gold surface, is ignored for the calculations in this section.

The solution volume was chosen to match the concentration used by Tsai *et al.*, who studied the bonding of PEG molecules to AuNPs, of 20 mmol L^{-1} which corresponds to one PEG molecule per 83 nm^3 [59]. This was done by extrapolating the calculated free-energy surface $F(z)$ such that the range in z for the nonbonded region times the surface area in the simulation gave a volume of 83 nm^3. The solution region in Eq. (4.2) was thus taken from $z = -60.5$ Å to $z = 19.5$ Å and the free-energy surface was assumed to be zero in this extrapolated range. The adsorbed region in Eq. (4.3) was from $z = 36.4$ Å to $z = 38.6$ Å.

The free-energy difference, calculated using the probability ratio method, as given by Eq. (4.1), is then $\Delta F = -1.27$ eV. This estimate agrees well with experimentally reported results of a binding energy of alkylthiols to gold surfaces of -1.30 eV which were independent of the alkyl length [161].

4.3 SEMI-ANALYTICAL ESTIMATE OF FREE ENERGY

When estimating the likelihood for a molecule to adsorb onto a surface it is customary to consider the free-energy change associated with the event [143, 159]. The Helmholtz free-energy change (or Gibbs free-energy change if pressure is fixed) indicates the degree of spontaneity of a given process with a more negative value reflecting that the process is energetically more favorable. The free-energy change ΔF associated with the binding event is given by

$$\Delta F = \Delta U - T\Delta S, \tag{4.4}$$

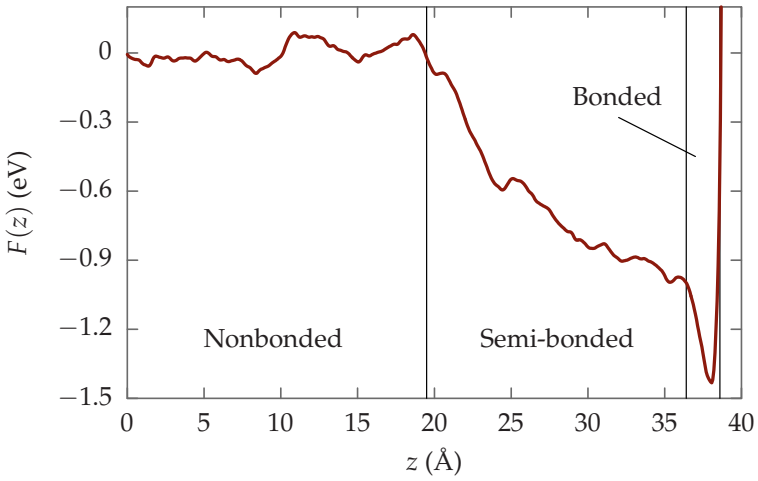

Figure 4.3: The resulting free-energy landscape $F(z)$ for CV defined as the z-position of the sulfur atom after 17 ns of simulation versus the CV position z. The vertical lines indicate the borders between nonbonded, semi-bonded, and bonded states.

where U is the total internal energy of the system, T is the absolute temperature, and $S = k_B \ln \Omega$ is the entropy of the system defined as the Boltzmann constant k_B times the log of the number of microstates of the system Ω.

The problem of estimating the free-energy change semi-analytically is divided into two parts: (i) calculating the internal energy change ΔU and (ii) calculating the entropy change ΔS. In both cases the change is evaluated between the situation where the PEG molecule is bonded to the surface and when it is free in the bulk part of the water medium.

4.3.1 Internal energy change

The change in internal energy associated with the binding of the PEG molecule is calculated as the difference in internal energy between when the PEG molecule is at the surface and when the PEG molecule is in the bulk water region in the same system. For the adsorption simulation, the PEG molecule was placed in proximity to the Au surface and a simulation of 2 ns was performed which was long enough that the PEG conformation was converged. The PEG molecule did not desorb during the simulation. For the bulk simulation the PEG was placed in the middle of the water region sufficiently far from the surface that there was no interaction and the simulation was performed for a similar duration of 2 ns. To avoid unwanted adsorption of the PEG molecule throughout the course of the simulation the PLUMED plugin of ATK-ForceField was used to apply a harmonic spring "restraint" with force constant 50 eV Å^{-2} between the center of mass of the PEG molecule and the center of the bulk water region in the z-direction, perpendicular to the gold surface. It was checked that other values of the force constant resulted in the same total energy estimate within statistical uncertainty. Movement in the xy-plane as well as rotation was not constrained.

The potential energy was monitored every 20 ps during the simulation trajectory and output from the last half of the trajectory was used to calculate the average potential energy of the system in both the adsorbed state and solution state. The potential energy change ΔU was

$$\begin{aligned}\Delta U &= U_{\text{ads}} - U_{\text{sol}} \\ &= -3.16\,\text{eV}\end{aligned} \tag{4.5}$$

with a standard error of mean of 0.61 eV.

4.3.2 Entropy change

The change in entropy ΔS associated with the adsorption of a coating molecule is given as the difference between the entropy of the adsorbed state S_{ads} and that of the coating molecule in solution S_{sol}

$$\Delta S = S_{\text{ads}} - S_{\text{sol}}. \tag{4.6}$$

To estimate the change in entropy the change in number of available microstates was calculated by calculating the ratio of the volumes available to the PEG molecule in the adsorbed and solution states. The adsorbed state is confined to the binding sites on the surface and the accessible volume can therefore be estimated as

$$V_{\text{ads}} = N_{\text{site}} V_{\text{site}}, \tag{4.7}$$

where N_{site} is the number of binding sites and V_{site} is the volume around each binding site which the molecule may explore due to vibrational motion at finite temperatures. This volume is estimated by observing the position of the sulfur atom during the trajectory to find the variance of the position in each direction, σ_x^2, σ_y^2, σ_z^2, respectively. Assuming a Gaussian distribution in all directions an ellipsoid shape of V_{site} is assumed and σ_x, σ_y, and σ_z are then taken as the principal semi-axes of this ellipsoid. The volume around each binding site is then given by

$$V_{\text{site}} = \frac{4}{3}\pi\sigma_x\sigma_y\sigma_z. \tag{4.8}$$

All top sites on the surface are potentially equal binding sites when using the GolP-CHARMM force field, so N_{site} is given by the number of gold atoms in the surface layer which was 144 in this simulation.

In the free state the molecule can move continuously so available volume V_{sol} is based on concentrations from literature. In the synthesis performed by Tsai *et al.*, who studied the bonding of PEG molecules to AuNPs, a concentration of PEG molecules of 20 mmol L^{-1} was used which corresponds to one PEG molecule per 83 nm^3 [59] which is used in the following as the value for V_{sol}.

The change in number of available microstates is approximated by the relative change in available volume and the entropy change associated with binding on the surface is then estimated as

$$\Delta S = k_{\text{B}} \ln\left(\frac{V_{\text{ads}}}{V_{\text{sol}}}\right). \tag{4.9}$$

From the simulation trajectory where the PEG molecule was bound to the surface the variances were $\sigma_x = 0.15\,\text{Å}$, $\sigma_y = 0.18\,\text{Å}$, and $\sigma_z = 0.08\,\text{Å}$, respectively. With $N_{\text{site}} = 144$ binding sites the entropic contribution to the free energy at $T = 300\,\text{K}$ is

$$-T\Delta S = 0.29\,\text{eV}. \tag{4.10}$$

In this estimate only the translational entropy change was considered which is the simplest to estimate and the contributions from rotational and conformational degrees of freedom as well as the entropy change associated with the displacement of water when the molecule binds to the surface have therefore been ignored as a first approximation.

4.3.3 Total change in free energy

The change in free energy associated with the binding of a single PEG molecule on a flat Au surface finally calculated by adding the contributions of the potential energy change and the entropy change:

$$\begin{aligned}\Delta F &= \Delta U - T\Delta S \\ &= -3.16\,\text{eV} + 0.29\,\text{eV} \\ &= -2.87\,\text{eV}.\end{aligned} \tag{4.11}$$

The positive contribution of the entropy term is outweighed by the negative potential energy change which indicates that the adsorption is energetically favored.

This estimate should be compared with the estimate calculated from the metaD method above which was $\Delta F_{\text{metaD}} = -1.27\,\text{eV}$. The relatively large discrepancy may be partly explained by the fact that the calculated entropy change included only the translational degrees of freedom and thus neglected contributions from rotational and conformational degrees of freedom which may be significant for a molecule such as PEG which is relatively flexible. Furthermore, since the adsorbed situation was calculated from a simulation without enhanced sampling, it is possible that the potential energy estimate results from a particular low-energy configuration, whereas the enhanced sampling in metadynamics takes into account a broad range of adsorbed configurations.

To achieve a more precise estimate via the semi-analytical approach more entropic contributions may be added. The distribution of the angle of the end-to-end-vectors may be evaluated and hence an estimate of the change in rotational entropy upon adsorption determined. In addition simulations of an ensemble of adsorbed states should be performed to ensure that a single low-energy configuration does not lead to misleading estimates of the adsorbed potential energy.

4.4 CONCLUSION

This chapter presented and compared two different methods for calculating the free-energy change associated with the adsorption of a PEG molecule on a flat (111) gold surface.

In the first method the free-energy surface associated with the position of the PEG molecule along the direction perpendicular to the gold surface was calculated. The free-energy change calculated with this method was $\Delta F_{\text{metaD}} = -1.27\,\text{eV}$. As metaD simulations inherently include several adsorbed conformations as well as all entropic contributions their results should be considered more precise, assuming that the simulations have reached convergence and that the force field describes the interaction, particularly between gold and sulfur, with sufficient accuracy. The calculated result agrees well with experimentally reported values where a binding energy of alkylthiols on gold of $-1.30\,\text{eV}$ was found independent on the alkyl length [161].

In the second method the free-energy change was estimated in a semi-analytical manner by calculating the potential energy change associated with the adsorption of the molecule and adding to it an analytical estimate of the entropy change via the loss of translational freedom of the molecule as it binds to the surface. In this case the free-energy change was calculated as $\Delta F_{\text{SA}} = -2.87\,\text{eV}$ which is dominated by the potential energy contribution with the entropy term playing a minor role.

One of the reasons for the discrepancy between the two methods could be an underestimate of the entropic contribution to the binding which results from only considering the translational loss of freedom. In reality, there will be contributions to the entropy change also from rotational and conformational loss of freedom of the PEG molecule as well as a contribution due to the displacement of water molecules upon adsorption of the PEG molecule none of which were included in this model. However, this is not likely to be responsible for the entire discrepancy. Another potential cause is the fact that only a single calculation of the PEG adsorbed to the surface was performed. To minimize the probability that the PEG was located in a particular low-energy configuration, more simulations should be performed and an average value taken to enhance the statistical sampling of the adsorbed state.

The adsorption free-energy suggests, in both cases, a relatively strong binding of the PEG molecule to the gold surface, which exceeds in magnitude the simulation results of many other, primarily physisorbed peptides, even those that are thought to bind relatively strongly to gold (about 0.3 eV) [143, 162]. The free-energy difference is, however, lower than the binding energy of a typical covalent bond (about 3 eV to 9 eV) which means that there is a likelihood that the molecule may be replaced by other molecules on longer timescales, e.g. inside the human body.

In both of these estimates a simplified model system was considered and the procedures presented should be seen as first steps in the direction of modeling the coating formation of spherical NP. To approach the case of a PEG-coated AuNP, one may run several metaD simulations with varying amounts of pre-adsorbed molecules on the surface to take into account the effect of finite surface coverage and to obtain the adsorption free-energy as a function of this coverage. The same protocol could be transferred from a planar surface to a spherical NP. As the metaD simulations might be more challenging under these additional conditions using the semi-analytical approach seems more appealing given that the additional contributions can be

accounted for by one of the methods suggested above. This procedure may then be applied to cases in which the metaD simulations would become too cumbersome due to the involved degrees of freedom and geometry, for instance in the case of coating formation on a spherical NP. Here, the semi-analytical approach may be conveniently used once contributions from rotational and vibrational entropy are included as well as contributions from interactions between PEG molecules during adsorption.

5 TRANSPORT OF ELECTRONS AND PRODUCTION OF RADICALS

Nanoparticles (NPs) have been studied as radiosensitizing agents for cancer therapy for more than a decade and it is now accepted that the increase in cell damage caused by radiosensitizing NPs is related to an increased production of secondary electrons which cause hydrolysis of the surrounding water medium and facilitate the formation of water radicals which form the main pathway of cell damage [4, 6, 37, 163]. In addition to the facilitation of water radical production, the potential of very low-energy electrons, of less than 15 eV, to cause damage directly to biological molecules through the mechanism of dissociative electron attachment has also been demonstrated [33, 40, 50, 163]. The radiosensitizing potential of a given NP thus hinges on its ability to increase the production of secondary electrons compared to a similar volume of pure water.

Due to the vast number of physicochemical properties which can be varied to optimize the radiosensitizing potential of a given NP (size, shape, and composition of its core, type and amount of coating molecules attached, etc.), it is virtually impossible to experimentally screen all combinations in the search for the optimal design. For this reason, computer simulations are often utilized to provide insights into the fundamental mechanisms responsible for the radiosensitization and to evaluate the structural properties and the radiosensitizing potential of a proposed NP-coating combination.

A thorough theoretical evaluation of the radiosensitizing potential of a suggested NP system should capture all the relevant effects of ion radiation interaction with biological media happening at different temporal, spatial, and energy scales including the ionization of the medium by the passing ion, the formation and transport of secondary particles (electrons and radicals), chemical interactions, thermo-mechanical pathways of biodamage, and heuristic biological criteria for cell survival and should also include the effects of the NP in this scenario. A popular method of simulating the production and transport of secondary electrons and free radicals created due to NPs and to evaluate the resulting biodamage is by means of Monte Carlo simulations (see e.g. Refs. [28, 29, 32]). These studies usually approximate the NPs as naked spheres and therefore fail to take into account the effect of the coating. NPs are always coated *in vivo*, either by design or by blood serum proteins which quickly cover any foreign body introduced to the blood stream [135, 164]. Although experiments have clearly demonstrated the radiosensitizing potential of coated NPs (see e.g. Refs. [36, 75, 76]) several experimental studies investigating the effect of coating in this scenario have indicated that the presence of a coating may strongly suppress the biodamage caused by NPs exposed to radiation [33, 34, 37]. This suggests that naked NPs are too crude an approximation and that simulations of naked NPs may not be able to provide accurate results comparable with *in vivo* situations. Monte Carlo simulations are furthermore restricted by the avail-

ability of precise scattering cross sections in order to simulated the transport of electrons emitted from NPs. Since such cross sections are usually unavailable for very low-energy electrons, Monte Carlo simulations mainly consider electrons with energy on the order of 10^2 eV to 10^3 eV.

This chapter presents the combined efforts to formulate an analytical and numerical framework to evaluate the production and transport of low-energy electrons emitted from a NP through its coating and to calculate the number of produced water radicals as a result of excitations by a carbon ion with energy corresponding to that of the Bragg peak (0.3 MeV/u) as well as higher energies corresponding to the entrance channel of the ion and as a function of the structural properties of the coating. Several discrete theoretical areas are combined in the framework presented in this chapter: (i) The description of collective electron excitations due to the passing ion and the resulting production of low-energy electrons evaluated by means of the plasmon resonance approximation [51], (ii) molecular dynamics simulations of the NP core and coating structure to evaluate the thickness and water content of the coating (as presented in Chapter 3), (iii) the dielectric formalism and partial-wave analysis for calculating the inelastic and elastic scattering cross sections of electrons with the coating medium [78, 79, 165, 166] to obtain diffusion coefficients and lifetimes of the electrons in the coating, and finally (iv) a description of the transport of electrons through the coating by means of a diffusion model [77]. The general workflow is illustrated schematically in Fig. 5.1

As a case study the framework is applied to a poly(ethylene glycol) (PEG) coated gold NP (AuNP) which is a combination receiving widespread scientific attention, see for instance Refs. [8, 35] and references therein. The gold core diameter is approximately 1.6 nm in diameter, comprising 135 atoms, and the PEG polymers consist of five monomers functionalized with a thiol group at one end and an amine group at the other end. The cases of 32 and 60 PEG molecules attached to the NP surface are studied as well as the naked AuNP for control. The coated NPs are taken from the same simulations that were analyzed in Chapter 3. It is important to stress that the framework is general and may well be applied to any coated NP system to analyze the radical yield as a function of projectile ion energy and coating structure by following the methodology presented in this chapter.

The chapter is outlined as follows: In Section 5.1 the diffusion equation for the electrons emitted from the AuNP is presented and its solution derived. In Section 5.2 the theory related to the calculation of elastic and inelastic mean free paths for the system is reviewed while in Section 5.3 the theory related to the collective electron excitations and the resulting production of electrons is briefly summarized. Finally, the results are presented and discussed in Section 5.4 and the conclusions are drawn in Section 5.5.

5.1 SOLUTION TO THE DIFFUSION EQUATION

The transport of electrons can be studied using a variety of methods depending on the circumstances such as the medium, the length scales, and the energies. For the design of modern transistors, the electronic current in semi-

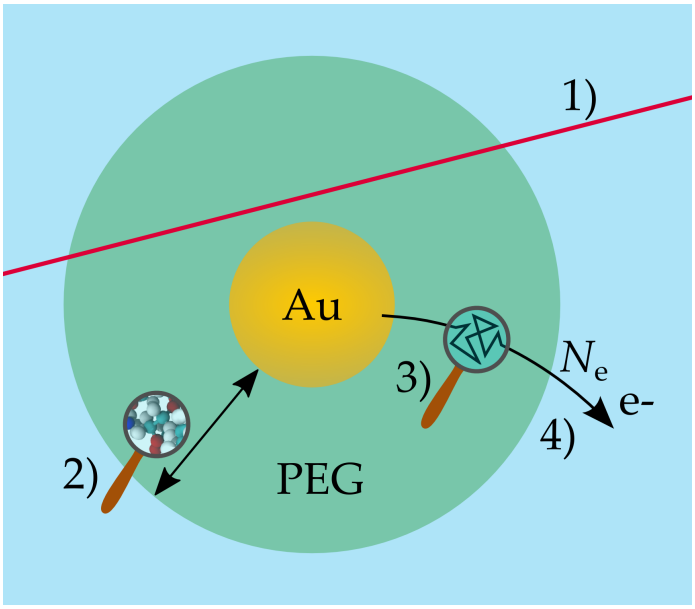

Figure 5.1: A PEG-coated AuNP in water excited by a passing ion is considered and the following workflow is applied. As a result of ion irradiation (1) N_e electrons are emitted from the metal core due to plasmon excitations and collective electron excitations in individual atoms of gold. After simulating the structure of the coated NP by means of molecular dynamics (2), the diffusion coefficients and average lifetimes of electrons diffusing through the coating are quantified by calculating elastic and inelastic scattering mean free paths (3). These numbers are used to obtain the number density of electrons passing through the coating (4) by solving the diffusion equation and to calculate the production of radicals in the coating.

conductors may be modeled accurately with *ab initio* models such as density functional theory [117, 118] as discussed in Section 2.3.4. Although highly accurate it is computationally impractical for systems with several tens of thousands of atoms as in the present case and a more approximate method is necessary. It was recently demonstrated by Surdutovich & Solov'yov that the transport of low-energy electrons, below 50 eV, can be modeled as a random walk process [77, 167] which is computationally relatively simple. The underlying assumption is that the angular dependence of the elastic and inelastic scattering cross sections for electrons with water is weak such that the collision processes can be considered isotropic [77, 168]. The random walk by each electron is therefore governed by characteristic elastic and inelastic scattering mean free paths and this picture allows for the analysis of the electron transport as a diffusion process with diffusion coefficient and average lifetime of the electrons dependent on their elastic and inelastic mean free paths. Additionally, one may estimate the production of water radicals due to the electrons from the inelastic scattering with the medium: At each inelastic scattering event with the water medium, the electron may ionize a water molecule if the kinetic energy of the electron E_1 is greater than the ionization potential of the medium I_p. In this case the inelastic collision leads to hydrolysis which may result in the production of a water radical and which produces an additional electron (referred to as the second-generation electron) and both of these electrons will share the excess energy after the ionization event [77], that is, the energy E_2, of the two second-generation electrons, is given by

$$E_2 = \frac{E_1 - I_p}{2}. \tag{5.1}$$

It should be mentioned for completeness, that there are other channels of radical formation that are not included in this framework. Dissociative electron attachment (DEA) of low-energy electrons with energy below the ionization threshold of water can also make a contribution to the production of water radicals [50], but since the probability of attachment to water is small (less than 10^{-4}) [30] this contribution is not included in the current framework. Additionally, the inelastic collisions of electrons with the PEG molecules and any products of such collisions have not been studied and are not included in this analysis.

We consider a AuNP of radius R and assume that N_e electrons are emitted uniformly from the surface at the initial time instance. These electrons are referred to as the first-generation electrons. It is further assumed that the electrons are emitted in all directions such that they can propagate both inside the AuNP core and outwards. This three-dimensional diffusion can be described by the following diffusion equation

$$\frac{\partial n_1(\mathbf{r}, t)}{\partial t} = D_1 \nabla^2 n_1(\mathbf{r}, t) - \frac{n_1(\mathbf{r}, t)}{\tau_1}, \tag{5.2}$$

where $n_1(\mathbf{r}, t)$ is the number density of first-generation electrons at point $\mathbf{r}$ and time t while D_1 is the diffusion coefficient and τ_1 is the average lifetime of first-generation electrons. The second term on the r.h.s. of Eq. (5.2) thus accounts for the decay of first-generation electrons due to inelastic collisions with the coating medium.

Because of the spherical symmetry of the problem Eq. (5.2) can be transformed to its radial form which simplifies the mathematics of the problem since the Laplacian, which in three dimensional spherical coordinates reads as

$$\nabla^2 f = \frac{1}{r^2}\frac{\partial}{\partial r}\left(r^2\frac{\partial f}{\partial r}\right) + \frac{1}{r^2\sin\theta}\frac{\partial}{\partial\theta}\left(\sin\theta\frac{\partial f}{\partial\theta}\right) + \frac{1}{r^2\sin^2\theta}\frac{\partial^2 f}{\partial\phi^2}, \tag{5.3}$$

reduces to

$$\nabla^2 f = \frac{1}{r^2}\frac{\partial}{\partial r}\left(r^2\frac{\partial f}{\partial r}\right). \tag{5.4}$$

Since the electrons can diffuse into two separate media, the gold core and the coating medium, Eq. (5.2) is rewritten to explicitly include an inner region (for $0 < r < R$), denoted by subscript "i", and an outer region (for $r \geq R$), denoted by subscript "o",

$$\frac{\partial n_1(r,t)}{\partial t} = \begin{cases} D_{1\mathrm{i}}\dfrac{1}{r^2}\dfrac{\partial}{\partial r}\left(r^2\dfrac{\partial n_{1\mathrm{i}}(r,t)}{\partial r}\right) - \dfrac{n_{1\mathrm{i}}(r,t)}{\tau_{1\mathrm{i}}}, & 0 < r < R \\ D_{1\mathrm{o}}\dfrac{1}{r^2}\dfrac{\partial}{\partial r}\left(r^2\dfrac{\partial n_{1\mathrm{o}}(r,t)}{\partial r}\right) - \dfrac{n_{1\mathrm{o}}(r,t)}{\tau_{1\mathrm{o}}}, & r \geq R. \end{cases} \tag{5.5}$$

To solve this equation, the following boundary conditions are imposed:

1. All electrons are emitted at the initial time ($t = 0$) from the surface of the NP at $r = R$
$$n_1(r,t) \propto \delta(r-R)\delta(t). \tag{5.6}$$

2. The density of electrons vanishes far from the NP
$$\lim_{r\to\infty} n_1(r,t) = 0. \tag{5.7}$$

3. The total number of electrons propagating in the medium and electrons which have been attenuated $n_{1,\mathrm{a}}$ is conserved
$$\int_0^\infty 4\pi r^2[n_1(r,t) + n_{1,\mathrm{a}}(r,t)]\mathrm{d}r = N_\mathrm{e}, \tag{5.8}$$
where the density of attenuated electrons is defined by
$$\frac{\partial n_{1,\mathrm{a}}(r,t)}{\partial t} = \frac{n_1(r,t)}{\tau_1}. \tag{5.9}$$

Below, the solution to the diffusion equation in the homogeneous case (inner and outer regions composed of the same material) is outlined to illustrate the procedure followed by the derivation of the solution in the general, inhomogeneous case in Section 5.1.2. Afterwards the solution in the homogeneous case is presented for the second-generation electrons in Section 5.1.3 and the procedure for using this result in the inhomogeneous case is explained.

5.1.1 Diffusion equation of first-generation electrons — homogeneous case

In the homogeneous case the diffusion parameters are identical in the inner and outer regions, $D_{1i} = D_{1o} = D$ and $\tau_{1i} = \tau_{1o} = \tau$, and the diffusion equation, given by Eq. (5.5), can be simplified as

$$\frac{\partial n_1(r,t)}{\partial t} = D\frac{1}{r^2}\frac{\partial}{\partial r}\left(r^2\frac{\partial n_1(r,t)}{\partial r}\right) - \frac{n_1(r,t)}{\tau}. \tag{5.10}$$

We seek a solution in the form

$$n_1(r,t) = \check{n}_1(r,t)e^{-t/\tau} \tag{5.11}$$

which is substituted into Eq. (5.10) to get

$$\frac{\partial \check{n}_1(r,t)}{\partial t} = D\frac{1}{r^2}\frac{\partial}{\partial r}\left(r^2\frac{\partial \check{n}_1(r,t)}{\partial r}\right). \tag{5.12}$$

By representing the number density as $\check{n}_1(r,t) = \xi_1(r,t)/r$, Eq. (5.12) can be further simplified:

$$\begin{aligned}\frac{\partial}{\partial t}\left(\frac{\xi_1(r,t)}{r}\right) &= D\frac{1}{r^2}\frac{\partial}{\partial r}\left(r^2\frac{\partial}{\partial r}\left(\frac{\xi_1(r,t)}{r}\right)\right)\\ &= D\frac{1}{r^2}\frac{\partial}{\partial r}\left(r\frac{\partial \xi_1(r,t)}{\partial r} - \xi_1(r,t)\right)\\ &= D\frac{\partial^2 \xi_1(r,t)}{\partial r^2}\frac{1}{r} \Leftrightarrow\\ \frac{\partial \xi_1(r,t)}{\partial t} &= D\frac{\partial^2 \xi_1(r,t)}{\partial r^2}.\end{aligned} \tag{5.13}$$

Next the Laplace transform of each side of the equation is performed, where the Laplace transform of $f(t)$, yielding $\tilde{f}(s)$, and the inverse Laplace transform of $\tilde{f}(s)$, yielding $f(t)$, are defined as

$$\tilde{f}(s) = \int_0^\infty e^{-st} f(t)\,\mathrm{d}t \tag{5.14}$$

$$f(t) = \int_{\sigma-i\infty}^{\sigma+i\infty} e^{st}\tilde{f}(s)\,\mathrm{d}s\,, \tag{5.15}$$

respectively. The Laplace transform of the l.h.s. of Eq. (5.13) can be shown to give $s\tilde{\xi}_1(r,s)$ while the Laplace transform of the r.h.s. can be solved by changing the order of the integral and the differential operators:

$$D\int_0^\infty e^{-st}\frac{\partial^2 \xi_1(r,t)}{\partial r^2}\,\mathrm{d}t = D\frac{\partial^2}{\partial r^2}\int_0^\infty e^{-st}\xi_1(r,t)\,\mathrm{d}t = D\frac{\partial^2 \tilde{\xi}_1(r,s)}{\partial r^2}. \tag{5.16}$$

Combining these terms allows for the transform of Eq. (5.13) into an ordinary differential equation

$$\frac{\partial^2 \tilde{\xi}_1(r,s)}{\partial r^2} = \frac{s}{D}\tilde{\xi}_1(r,s) \tag{5.17}$$

which has the general solution

$$\tilde{\xi}_1(r,s) = C^-(s)e^{-\sqrt{s/D}r} + C^+(s)e^{\sqrt{s/D}r}. \tag{5.18}$$

Next, $\xi_1(r,t)$ is represented as an inverse Laplace transform

$$\xi_1(r,t) = \frac{1}{2\pi i}\int_{\sigma-i\infty}^{\sigma+i\infty} \mathrm{d}s\, e^{st}\tilde{\xi}_1(r,s) \tag{5.19}$$

into which the general solution, given by Eq. (5.18), is substituted to obtain

$$\xi_1(r,t) = \frac{1}{2\pi i}\int_{\sigma-i\infty}^{\sigma+i\infty} \mathrm{d}s\, C^-(s)e^{st-\sqrt{s/D}r} + \frac{1}{2\pi i}\int_{\sigma-i\infty}^{\sigma+i\infty} \mathrm{d}s\, C^+(s)e^{st+\sqrt{s/D}r}. \tag{5.20}$$

By taking into account that electrons may travel both inside ("i") and outside ("o") the NP after being emitted from its surface leads to one obtains

$$\begin{aligned}\xi_1(r,t) =& \frac{1}{2\pi i}\int_{\sigma-i\infty}^{\sigma+i\infty} \mathrm{d}s\, C_{\mathrm{i}}^-(s)e^{st-\sqrt{s/D}r}H(R-r)\\ &+ \frac{1}{2\pi i}\int_{\sigma-i\infty}^{\sigma+i\infty} \mathrm{d}s\, C_{\mathrm{i}}^+(s)e^{st+\sqrt{s/D}r}H(R-r)\\ &+ \frac{1}{2\pi i}\int_{\sigma-i\infty}^{\sigma+i\infty} \mathrm{d}s\, C_{\mathrm{o}}^-(s)e^{st-\sqrt{s/D}r}H(r-R)\\ &+ \frac{1}{2\pi i}\int_{\sigma-i\infty}^{\sigma+i\infty} \mathrm{d}s\, C_{\mathrm{o}}^+(s)e^{st+\sqrt{s/D}r}H(r-R),\end{aligned} \tag{5.21}$$

where $H(x)$ is the Heaviside step function. The first two terms on the r.h.s. of Eq. (5.21) thus describe the space inside the NP core ($0 < r < R$) while the two latter terms describe the outside part ($r \geq R$).

To solve this equation, first the constant $C_{\mathrm{o}}^+(s)$ may immediately be set to zero to avoid exponential growth of $\xi_1(r,s)$ as $r \to \infty$. Second, since only the radial component of the problem is considered there must be reflection at $r = 0$, that is,

$$\left.\frac{\partial \check{n}_1(r,t)}{\partial r}\right|_{r=0} = 0, \tag{5.22}$$

which, remembering that $\check{n}_1(r,t) = \xi_1(r,t)/r$, implies that

$$\begin{aligned}0 &= \frac{1}{r}\left.\frac{\partial \xi_1(r,t)}{\partial r}\right|_{r=0} - \frac{1}{r^2}\left.\xi_1(r,t)\right|_{r=0}\\ &= r\left.\frac{\partial \xi_1(r,t)}{\partial r}\right|_{r=0} - \left.\xi_1(r,t)\right|_{r=0}\\ &= -\left.\xi_1(r,t)\right|_{r=0}\\ &= -\frac{1}{2\pi i}\int_{\sigma-i\infty}^{\sigma+i\infty} \mathrm{d}s\, C_{\mathrm{i}}^-(s)e^{st-\sqrt{s/D}\cdot 0} - \frac{1}{2\pi i}\int_{\sigma-i\infty}^{\sigma+i\infty} \mathrm{d}s\, C_{\mathrm{i}}^+(s)e^{st+\sqrt{s/D}\cdot 0}\\ &= -\frac{1}{2\pi i}\int_{\sigma-i\infty}^{\sigma+i\infty} \mathrm{d}s\, e^{st}(C_{\mathrm{i}}^-(s) + C_{\mathrm{i}}^+(s)) \Rightarrow\\ -C_{\mathrm{i}}^-(s) &= C_{\mathrm{i}}^+(s).\end{aligned} \tag{5.23}$$

Next, the boundary condition that the number density $\check{n}_1(r,t)$, and therefore also $\tilde{\xi}_1(r,t)$, should be continuous functions at the NP surface $r = R$ can be stated as

$$\begin{aligned}\check{n}_1(r,t)_{r\to R_-} &= \check{n}_1(r,t)_{r\to R_+}\\ \xi_1(r,t)_{r\to R_-} &= \xi_1(r,t)_{r\to R_+}.\end{aligned} \tag{5.24}$$

Applying this condition to Eq. (5.21), and using that $-C_{\mathrm{i}}^{-}(s) = C_{\mathrm{i}}^{+}(s)$, leads to the following equation

$$\frac{1}{2\pi i}\int_{\sigma-i\infty}^{\sigma+i\infty} \mathrm{d}s\, C_{\mathrm{i}}^{-}(s)e^{st}\left(e^{-\sqrt{s/D}R} - e^{\sqrt{s/D}R}\right) = \frac{1}{2\pi i}\int_{\sigma-i\infty}^{\sigma+i\infty} \mathrm{d}s\, C_{\mathrm{o}}^{-}(s)e^{st-\sqrt{s/D}R} \tag{5.25}$$

which can be rewritten as

$$\mathcal{L}^{-1}\left[C_{\mathrm{i}}^{-}(s)\left(e^{-\sqrt{s/D}R} - e^{\sqrt{s/D}R}\right)\right] = \mathcal{L}^{-1}\left[C_{\mathrm{o}}^{-}(s)e^{-\sqrt{s/D}R}\right], \tag{5.26}$$

where $\mathcal{L}^{-1}\left[\tilde{f}(s)\right]$ is the inverse Laplace transform of $\tilde{f}(s)$. From this one obtains the following relation

$$C_{\mathrm{i}}^{-}(s)\left(e^{-\sqrt{s/D}R} - e^{\sqrt{s/D}R}\right) = C_{\mathrm{o}}^{-}(s)e^{-\sqrt{s/D}R} \tag{5.27}$$

which, by using the substitutions

$$\begin{aligned} C_{\mathrm{i}}^{-}(s) &= \check{C}_{\mathrm{i}}^{-}(s)e^{-\sqrt{s/D}R} \\ C_{\mathrm{o}}^{-}(s) &= \check{C}_{\mathrm{o}}^{-}(s)e^{\sqrt{s/D}R}, \end{aligned} \tag{5.28}$$

can be rewritten as

$$\check{C}_{\mathrm{o}}^{-}(s) = \check{C}_{\mathrm{i}}^{-}(s)\left[e^{-2\sqrt{s/D}R} - 1\right]. \tag{5.29}$$

Using this relation, Eq. (5.21) can be written as

$$\begin{aligned} \xi_1(r,t) = &\frac{1}{2\pi i}\int_{\sigma-i\infty}^{\sigma+i\infty} \mathrm{d}s\, \check{C}_{\mathrm{i}}^{-}(s)e^{st}\left(e^{-\sqrt{s/D}(r+R)} - e^{\sqrt{s/D}(r-R)}\right)H(R-r) \\ &+ \frac{1}{2\pi i}\int_{\sigma-i\infty}^{\sigma+i\infty} \mathrm{d}s\, \check{C}_{\mathrm{i}}^{-}(s)e^{st}\left(e^{-\sqrt{s/D}(r+R)} - e^{-\sqrt{s/D}(r-R)}\right)H(r-R) \end{aligned} \tag{5.30}$$

which, by combining the Heaviside functions, can be further transformed into

$$\xi_1(r,t) = \frac{1}{2\pi i}\int_{\sigma-i\infty}^{\sigma+i\infty} \mathrm{d}s\, \check{C}_{\mathrm{i}}^{-}(s)e^{st}\left(e^{-\sqrt{s/D}(r+R)} - e^{-\sqrt{s/D}|r-R|}\right). \tag{5.31}$$

Because $\xi_1(r,t)$ represents the number density by $\xi_1(r,t) = \check{n}_1(r,t)r$, it must be positive, and since

$$r + R > |r-R| \Leftrightarrow \tag{5.32}$$

$$e^{-\sqrt{s/D}(r+R)} - e^{-\sqrt{s/D}|r-R|} < 0 \tag{5.33}$$

it follows that the constant $\check{C}_{\mathrm{i}}^{-}(s)$ should be negative to make sure that $\xi_1(r,t) > 0$. The constant is redefined for simplicity as $C(s) \equiv -\check{C}_{\mathrm{i}}^{-}(s) > 0$ which leads to

$$\xi_1(r,t) = \frac{1}{2\pi i}\int_{\sigma-i\infty}^{\sigma+i\infty} \mathrm{d}s\, C(s)e^{st}\left(e^{-\sqrt{s/D}|r-R|} - e^{-\sqrt{s/D}(r+R)}\right). \tag{5.34}$$

The initial condition that N_{e} electrons are emitted at the time instance $t = 0$ lets us determine $C(s)$:

$$\begin{aligned} N_{\mathrm{e}}H(t) &= \int_0^\infty \check{n}_1(r,t)4\pi r^2\,\mathrm{d}r = \int_0^\infty \xi_1(r,t)4\pi r\,\mathrm{d}r \\ &= \frac{1}{2\pi i}\int_{\sigma-i\infty}^{\sigma+i\infty} \mathrm{d}s\, C(s)e^{st} \\ &\quad \times 4\pi\int_0^\infty \mathrm{d}r\, r\left(e^{-\sqrt{s/D}|r-R|} - e^{-\sqrt{s/D}(r+R)}\right). \end{aligned} \tag{5.35}$$

The integral over r can be carried out analytically by splitting it up in two integrals over the inner region ($r = 0$ to $r = R$) and the outer region ($r = R$ to $r = \infty$):

$$\int_0^R \mathrm{d}r\, r\left(e^{\sqrt{s/D}(r-R)} - e^{-\sqrt{s/D}(r+R)}\right) = \frac{D\left(R\sqrt{\frac{s}{D}} + e^{-2R\sqrt{\frac{s}{D}}}\left(R\sqrt{\frac{s}{D}}+1\right) - 1\right)}{s} \tag{5.36}$$

$$\int_R^\infty \mathrm{d}r\, r\left(e^{-\sqrt{s/D}(r-R)} - e^{-\sqrt{s/D}(r+R)}\right) = \frac{De^{-2R\sqrt{\frac{s}{D}}}\left(e^{2R\sqrt{\frac{s}{D}}} - 1\right)\left(R\sqrt{\frac{s}{D}}+1\right)}{s} \tag{5.37}$$

the sum of which gives $2R\sqrt{D/s}$.

Combining with the rest results in the following expression

$$N_\mathrm{e}H(t) = \frac{4R\sqrt{D}}{i}\int_{\sigma-i\infty}^{\sigma+i\infty}\mathrm{d}s\,\frac{e^{st}}{s}C_0, \tag{5.38}$$

where the substitution $C_0 = \sqrt{s}C(s)$ was introduced. Since the integrand contains a singularity at $s = 0$, Cauchy's integral formula, which states that

$$\frac{1}{2\pi i}\oint_\gamma \frac{f(z)}{z-a}\,\mathrm{d}z = f(a), \tag{5.39}$$

where γ is the contour enclosing the singularity on which the integral is done and $z = a$ is the singularity, can be used to solve the integral:

$$N_\mathrm{e}H(t) = \frac{8\pi R\sqrt{D}}{2\pi i}\int_{\sigma-i\infty}^{\sigma+i\infty}\mathrm{d}s\,\frac{e^{st}}{s}C_0 = 8\pi R\sqrt{D}C_0 \Leftrightarrow \tag{5.40}$$

$$C_0 = \frac{N_\mathrm{e}}{8\pi R\sqrt{D}}. \tag{5.41}$$

By inserting $C(s) = C_0/\sqrt{s}$ into Eq. (5.34) one obtains

$$\xi_1(r,t) = \frac{N_\mathrm{e}}{16\pi^2 iR\sqrt{D}}\int_{\sigma-i\infty}^{\sigma+i\infty}\mathrm{d}s\,\frac{e^{st}}{\sqrt{s}}\left(e^{-\sqrt{s/D}|r-R|} - e^{-\sqrt{s/D}(r+R)}\right). \tag{5.42}$$

which leads to the solution for $\xi_1(r,t)$

$$\xi_1(r,t) = \frac{N_\mathrm{e}}{8\pi^{3/2}R\sqrt{Dt}}\left[e^{-(r-R)^2/4Dt} - e^{-(r+R)^2/4Dt}\right]. \tag{5.43}$$

Dividing $\xi_1(r,t)$ by r and including the exponential factor $e^{-t/\tau}$ finally leads to

$$n(r,t) = \frac{N_\mathrm{e}}{8\pi^{3/2}Rr\sqrt{Dt}}e^{-t/\tau}\left[e^{-(r-R)^2/4Dt} - e^{-(r+R)^2/4Dt}\right] \tag{5.44}$$

which is the solution for the number density of electrons emitted from the surface of a NP with radius R assuming equal diffusion coefficients and average lifetimes $D_1 = D_2 = D$ and $\tau_1 = \tau_2 = \tau$ in the inner and outer regions.

5.1.2 Diffusion equation of first-generation electrons — inhomogeneous case

In general, the diffusion constants and lifetimes in the inner and outer regions need not be equal, that is, when $D_{1\mathrm{i}} \neq D_{1\mathrm{o}}$ and $\tau_{1\mathrm{i}} \neq \tau_{1\mathrm{o}}$. Let us now turn to the case where we have two different media: the gold core ($0 < r < R$) and the coating medium ($r \geq R$) in which the electrons propagate with distinct diffusion coefficients $D_{1\mathrm{i}}$ and $D_{1\mathrm{o}}$, respectively, and have distinct lifetimes τ_{i} and τ_{o}, respectively. This situation is referred to as the inhomogeneous case and the diffusion equations is in this case given by Eq. (5.5). This section presents how the inhomogeneous diffusion equation can be solved.

First, the substitution $n_1(r,t) = \xi_1(r,t)/r$ is introduced which reduces the diffusion equation to

$$\frac{\partial \xi_1(r,t)}{\partial t} = \begin{cases} D_{1\mathrm{i}} \dfrac{\partial^2 \xi_1(r,t)}{\partial r^2} - \dfrac{\xi_1(r,t)}{\tau_{1\mathrm{i}}}, & 0 < r < R \\ D_{1\mathrm{o}} \dfrac{\partial^2 \xi_1(r,t)}{\partial r^2} - \dfrac{\xi_1(r,t)}{\tau_{1\mathrm{o}}}, & r \geq R. \end{cases} \tag{5.45}$$

Applying the Laplace transform to both sides, similarly to the procedure in the homogeneous case, transforms Eq. (5.45) to

$$s\tilde{\xi}_1(r,s) = \begin{cases} D_{1\mathrm{i}} \dfrac{\partial^2 \tilde{\xi}_1(r,s)}{\partial r^2} - \dfrac{\tilde{\xi}_1(r,s)}{\tau_{1\mathrm{i}}}, & 0 < r < R \\ D_{1\mathrm{o}} \dfrac{\partial^2 \tilde{\xi}_1(r,s)}{\partial r^2} - \dfrac{\tilde{\xi}_1(r,s)}{\tau_{1\mathrm{o}}}, & r \geq R \end{cases} \tag{5.46}$$

which can be rearranged to

$$\frac{\partial^2 \tilde{\xi}_1(r,s)}{\partial r^2} = \begin{cases} \dfrac{s + \gamma_{1\mathrm{i}}}{D_{1\mathrm{i}}} \tilde{\xi}_1(r,s), & 0 < r < R \\ \dfrac{s + \gamma_{1\mathrm{o}}}{D_{1\mathrm{o}}} \tilde{\xi}_1(r,s), & r \geq R, \end{cases} \tag{5.47}$$

where $\gamma_{\mathrm{i,o}} = 1/\tau_{\mathrm{i,o}}$, respectively.

This equation has the general solutions in the inner and outer regions, $\tilde{\xi}_{1\mathrm{i}}(r,s)$ and $\tilde{\xi}_{1\mathrm{o}}(r,s)$, respectively, as given by

$$\begin{aligned} \tilde{\xi}_{1\mathrm{i}}(r,s) &= C_{\mathrm{i}}^{-}(s) e^{-A_{\mathrm{i}} r} + C_{\mathrm{i}}^{+}(s) e^{A_{\mathrm{i}} r}, \quad 0 < r < R \\ \tilde{\xi}_{1\mathrm{o}}(r,s) &= C_{\mathrm{o}}^{-}(s) e^{-A_{\mathrm{o}} r} + C_{\mathrm{o}}^{+}(s) e^{A_{\mathrm{o}} r}, \quad r \geq R. \end{aligned} \tag{5.48}$$

where the substitutions $A_{\mathrm{i}} = \sqrt{(s + \gamma_{1\mathrm{i}})/D_{1\mathrm{i}}}$ and $A_{\mathrm{o}} = \sqrt{(s + \gamma_{1\mathrm{o}})/D_{1\mathrm{o}}}$, were introduced for brevity.

The same boundary conditions as for the homogeneous case are applied. First, the constant $C_{\mathrm{o}}^{+}(s)$ is set to zero to avoid exponential growth of the number density as $r \to \infty$. Second, reflection at $r = 0$, implying that

$$\left. \frac{\partial \check{n}_1(r,t)}{\partial r} \right|_{r=0} = 0, \tag{5.49}$$

which, recalling that $\check{n}_1(r,t) = \xi_1(r,t)/r$, leads to the following relation, in a similar way as the homogeneous case,

$$\begin{aligned} 0 &= \frac{1}{r}\left.\frac{\partial \xi_1(r,t)}{\partial r}\right|_{r=0} - \left.\frac{1}{r^2}\,\xi_1(r,t)\right|_{r=0} \\ &= r\left.\frac{\partial \xi_1(r,t)}{\partial r}\right|_{r=0} - \left.\xi_1(r,t)\right|_{r=0} \\ &= -\left.\xi_1(r,t)\right|_{r=0} \\ &= -C_{\mathrm{i}}^{-}(s)e^{st-A_{\mathrm{i}}\cdot 0} - C_{\mathrm{i}}^{+}(s)e^{st+A_{\mathrm{i}}\cdot 0} \\ &= -C_{\mathrm{i}}^{-}(s) - C_{\mathrm{i}}^{+}(s) \Leftrightarrow \\ -C_{\mathrm{i}}^{-}(s) &= C_{\mathrm{i}}^{+}(s). \end{aligned} \tag{5.50}$$

Inserting this into Eq. (5.48) with $C_{\mathrm{o}}^{+}(s) = 0$, and applying the continuity requirement at $r = R$, leads to the following relation

$$C_{\mathrm{i}}^{-}(s)\left(e^{-A_{\mathrm{i}}R} - e^{A_{\mathrm{i}}R}\right) = C_{\mathrm{o}}^{-}(s)e^{-A_{\mathrm{o}}R} \tag{5.51}$$

which, by making the following substitution

$$C_{\mathrm{i}}^{-}(s) = \check{C}_{\mathrm{i}}^{-}(s)e^{-A_{\mathrm{i}}R}, \tag{5.52}$$

can be rewritten as

$$C_{\mathrm{o}}^{-}(s) = \check{C}_{\mathrm{i}}^{-}(s)\left(e^{-2A_{\mathrm{i}}R} - 1\right)e^{A_{\mathrm{o}}R}. \tag{5.53}$$

By inserting Eqs. (5.52) and (5.53) into Eq. (5.48), one obtains

$$\begin{aligned} \tilde{\xi}_{1\mathrm{i}}(r,s) &= \check{C}_{\mathrm{i}}^{-}(s)\left[e^{-A_{\mathrm{i}}(r+R)} - e^{A_{\mathrm{i}}(r-R)}\right], \qquad 0 < r < R \\ \tilde{\xi}_{1\mathrm{o}}(r,s) &= \check{C}_{\mathrm{i}}^{-}(s)\left[\left(e^{-2A_{\mathrm{i}}R} - 1\right)e^{-A_{\mathrm{o}}(r-R)}\right], \quad r \geq R. \end{aligned} \tag{5.54}$$

The constant $\check{C}_{\mathrm{i}}^{-}(s)$ can be found from the normalization requirement that the number of propagating and attenuated electrons (those which have inelastically collided with the medium) be constant, as stated in Eq. (5.8):

$$\int_0^R 4\pi r\left[\tilde{\xi}_{1\mathrm{i}}(r,s) + \tilde{\xi}_{1\mathrm{i,a}}(r,s)\right]\mathrm{d}r + \int_R^\infty 4\pi r\left[\tilde{\xi}_{1\mathrm{o}}(r,s) + \tilde{\xi}_{1\mathrm{o,a}}(r,s)\right]\mathrm{d}r = \frac{N_{\mathrm{e}}}{s}, \tag{5.55}$$

where

$$\begin{aligned} \tilde{\xi}_{1\mathrm{i,a}}(r,s) &= \frac{\gamma_{1\mathrm{i}}}{s}\tilde{\xi}_{1\mathrm{i}}(r,s) \\ \tilde{\xi}_{1\mathrm{o,a}}(r,s) &= \frac{\gamma_{1\mathrm{o}}}{s}\tilde{\xi}_{1\mathrm{o}}(r,s) \end{aligned} \tag{5.56}$$

are the Laplace transforms of the attenuated number densities for the inside and outside regions, respectively. The normalization condition can then be rewritten as

$$\int_0^R 4\pi r\left[1 + \frac{\gamma_{1\mathrm{i}}}{s}\right]\tilde{\xi}_{1\mathrm{i}}(r,s)\,\mathrm{d}r + \int_R^\infty 4\pi r\left[1 + \frac{\gamma_{1\mathrm{o}}}{s}\right]\tilde{\xi}_{1\mathrm{o}}(r,s)\,\mathrm{d}r = \frac{N_{\mathrm{e}}}{s}. \tag{5.57}$$

Inserting the definitions for $\tilde{\xi}_{1\mathrm{i}}(r,s)$ and $\tilde{\xi}_{1\mathrm{o}}(r,s)$ from Eq. (5.54), the solution to this integral can be found analytically and $\check{C}_{\mathrm{i}}^{-}(s)$ is obtained as

$$\check{C}_{\mathrm{i}}^{-}(s) = \frac{N_{\mathrm{e}}}{s(A-B)}, \tag{5.58}$$

where

$$A = \frac{4\pi}{s}\left[e^{-2R\sqrt{(s+\gamma_{1i})/D_{1i}}} - 1\right]\left(R\sqrt{D_{1o}(s+\gamma_{1o})} + D_{1o}\right)$$
$$B = \frac{4\pi D_{1i}}{s}\left[R\sqrt{\frac{s+\gamma_{1i}}{D_{1i}}} - 1 + e^{-2R\sqrt{(s+\gamma_{1i})/D_{1i}}}\left(R\sqrt{\frac{s+\gamma_{1i}}{D_{1i}}} + 1\right)\right]. \tag{5.59}$$

Finally, inserting $\check{C}_i^-(s)$ into Eq. (5.54) will allow for the general, inhomogeneous solution by doing the inverse Laplace transform to find $\xi_{1i}(r,t)$ and $\xi_{1o}(r,t)$, and from there the number density $n_1(r,t)$ in the inner and outer regions. This is only possible to do analytically for the homogeneous case when $D_{1i} = D_{1o} = D$ and $\tau_{1i} = \tau_{1o} = \tau$ which results in the same solution as Eq. (5.44). For the inhomogeneous case, the inverse Laplace transform was performed numerically with MATHEMATICA using the Fixed-Talbot algorithm[1] described in Ref. [169].

The resulting number density of first-generation electrons n_1 is plotted in Fig. 5.9 using values for D, τ, and N_e which will be derived in the following sections.

5.1.3 Diffusion equation of second-generation electrons — homogeneous case

In the framework used here, it is assumed that each inelastic collision of a first-generation electron emitted from the surface of the NP with the coating medium leads to the formation of two second-generation electrons if the energy of the first-generation electron is higher than the ionization potential I_p of the coating medium. The diffusion equation for the second-generation electrons is

$$\frac{\partial n_2(\mathbf{r},t)}{\partial t} = D_2\nabla^2 n_2(\mathbf{r},t) - \frac{n_2(\mathbf{r},t)}{\tau_2} + 2\frac{n_{1,E>I_p}(r,t)}{\tau_1}, \tag{5.60}$$

where the subscripts 1 and 2 refer to electrons of the first and second generation, respectively. The last term represents the fact that each inelastically scattering first-generation electron with energy above the ionization threshold of the coating medium leads to the production of two second-generation electrons. In the following, the density of these first-generation electrons is denoted as $n_1(r,t)$ for brevity.

Taking advantage of the spherical symmetry of the problem Eq. (5.60) can be rewritten in the same manner as Eq. (5.5) for the first generation:

$$\frac{\partial n_2(r,t)}{\partial t} = \begin{cases} D_{2i}\dfrac{1}{r^2}\dfrac{\partial}{\partial r}\left(r^2\dfrac{\partial n_{2i}(r,t)}{\partial r}\right) - \dfrac{n_{2i}(r,t)}{\tau_{2i}} + 2\dfrac{n_1(r,t)}{\tau_{1i}}, & 0 < r < R \\ D_{2o}\dfrac{1}{r^2}\dfrac{\partial}{\partial r}\left(r^2\dfrac{\partial n_{2o}(r,t)}{\partial r}\right) - \dfrac{n_{2o}(r,t)}{\tau_{2o}} + 2\dfrac{n_1(r,t)}{\tau_{1o}}, & r \geq R. \end{cases} \tag{5.61}$$

Equation (5.61) is an inhomogeneous, linear differential equation for each region and can be solved using the Green's function method for which a short introduction is given in Appendix A. This section will present the

1 A MATHEMATICA package for the Fixed-Talbot algorithm is available at http://library.wolfram.com/infocenter/MathSource/5026/

derivation of the solution for the homogeneous case and then describe how one may approximate the inhomogeneous case.

Before the Green's function method can be applied to solve Eq. 5.61, first the Green's function for the diffusion equation must be derived. In the homogeneous case the diffusion equation for the second generation of electrons in spherical coordinates, considering only the radial component due to symmetry, is given by

$$\frac{\partial n_2(r,t)}{\partial t} = D\nabla^2 n_2(r,t) - \frac{n_2(r,t)}{\tau_2} + 2\frac{n_1(r,t)}{\tau_1}, \tag{5.62}$$

where $\nabla^2 = \frac{1}{r^2}\frac{\partial}{\partial r}\left(r^2\frac{\partial}{\partial r}\right)$ in spherically symmetric coordinates. The solution can be found with the Green's function method by solving the equation

$$n_2(r,t) = 2\int G(r-r',t-t')\frac{n_1(r',t')}{\tau_1}\,\mathrm{d}r'\,\mathrm{d}t', \tag{5.63}$$

where $G(r-r',t-t')$ is used to evaluate the response at position r and time t due to an electron which decayed at position r' and time $t' < t$.

To find the Green's function $G(r-r',t-t')$ for this problem, the linear differential operator L of Eq. (5.62) is written as

$$L(r,t) = \frac{\partial}{\partial t} - D\nabla^2 + \frac{1}{\tau}, \tag{5.64}$$

where $\tau = \tau_2$ for brevity. The Green's function is, in general, defined by the equation

$$L(r,t)G(r,t) = \delta(r)\delta(t) \tag{5.65}$$

and the idea of the Green's function is that once it is found $n_2(r,t)$ can be determined by the convolution integral given in Eq. (5.63).

By combining Eq. (5.64) with Eq. (5.65) it is seen that the Green's function $G(r,t)$ is defined by the following equation

$$\left(\frac{\partial}{\partial t} - D\nabla^2 + \frac{1}{\tau}\right)G(r,t) = \frac{1}{4\pi r^2}\delta(r)\delta(t), \tag{5.66}$$

where the factor $1/4\pi r^2$ is a normalization factor of the delta function in spherical coordinates. By introducing the following substitution $G(r,t) = g(r,t)/r$ and rewriting the Laplacian as its spherical version

$$\frac{1}{r^2}\frac{\partial}{\partial r}\left(r^2\frac{\partial}{\partial r}\right)\frac{g(r,t)}{r} = \frac{1}{r}\frac{\partial^2}{\partial r^2}g(r,t), \tag{5.67}$$

Eq. (5.66) can now be restated as

$$\frac{1}{r}\left(\frac{\partial}{\partial t} - D\frac{\partial^2}{\partial r^2} + \frac{1}{\tau}\right)g(r,t) = \frac{1}{4\pi r^2}\delta(r)\delta(t). \tag{5.68}$$

Next, the Fourier representations of the terms on both sides of Eq. (5.68) will be used to determine $g(r,t)$ and from it $G(r,t)$. We define the Fourier transform such that the relationship between a function $f(x)$ and its Fourier transform $\hat{f}(k)$ is given by

$$\hat{f}(k) = \int_{-\infty}^{\infty} f(x)e^{ikx}\,\mathrm{d}x \tag{5.69}$$

$$f(x) = \frac{1}{2\pi}\int_{-\infty}^{\infty}\hat{f}(k)e^{-ixk}\,\mathrm{d}k\,. \tag{5.70}$$

First, the factor $1/r$ is canceled out on each side of Eq. (5.68) and the Fourier transform of $\delta(r)/r$ is performed using the result

$$\mathcal{F}\left[\frac{\delta(x)}{x}\right] = ik, \tag{5.71}$$

where $\hat{f}(k) = \mathcal{F}[f(x)]$ is the Fourier transform of $f(x)$, while the Fourier transform of $\delta(t)$ gives 1.

Second, to take the Fourier transforms of the derivatives on the l.h.s. of Eq. (5.68) the following identity is used:

$$\mathcal{F}\left[\frac{\partial}{\partial x} f(x)\right] = -ik\hat{f}(k) \tag{5.72}$$

to obtain the fully Fourier transformed version of Eq. (5.68):

$$\left(-i\omega + Dq^2 + \frac{1}{\tau}\right)\hat{g}(q,\omega) = \frac{iq}{4\pi}, \tag{5.73}$$

where ω and q are the Fourier transformed coordinates of t and r, respectively. By isolating $\hat{g}(q,\omega)$ one obtains

$$\hat{g}(q,\omega) = \frac{iq}{4\pi}\frac{1}{-i\omega + Dq^2 + \frac{1}{\tau}} = \frac{iq}{4\pi}\frac{1}{-i(\omega - \omega_0)}, \tag{5.74}$$

with $\omega_0 = -i\left(Dq^2 + \frac{1}{\tau}\right)$.

Doing the inverse Fourier transform first from ω to t amounts to solving the integral

$$-\frac{1}{2\pi i}\int_{-\infty}^{\infty}\frac{e^{-i\omega t}}{\omega - \omega_0}\,\mathrm{d}\omega \tag{5.75}$$

which can be solved using the Cauchy integral formula:

$$\frac{1}{2\pi i}\oint_{\gamma}\frac{f(z)}{z-a}\,\mathrm{d}z = f(a), \tag{5.76}$$

where γ is the contour enclosing the singularity on which the integral is done and $z = a$ is the singularity. The result is

$$-\frac{1}{2\pi i}\int_{-\infty}^{\infty}\frac{e^{-i\omega t}}{\omega - \omega_0}\,\mathrm{d}\omega = e^{-i\omega_0 t} = e^{-Dtq^2 - t/\tau}. \tag{5.77}$$

The sign change occurs because the pole ω_0 is in the negative imaginary half-plane so that the contour is clockwise.

The inverse Fourier transform from q to r can be solved by "completing the squares" method as follows

$$\begin{aligned} g(r,t) &= \frac{1}{2\pi}\int_{-\infty}^{\infty} e^{-iqr}e^{-Dtq^2-t/\tau}\frac{iq}{4\pi}\,\mathrm{d}q \\ &= \frac{e^{-t/\tau}}{8\pi^2}\int_{-\infty}^{\infty} e^{-Dtq^2-iqr}iq\,\mathrm{d}q \\ &= \frac{e^{-t/\tau}}{8\pi^2}\int_{-\infty}^{\infty} e^{-Dt\beta^2-\frac{r^2}{4Dt}}\left(i\beta+\frac{r}{2Dt}\right)\mathrm{d}\beta\,, \qquad \beta = q+\frac{ir}{2Dt} \\ &= \frac{e^{-\frac{r^2}{4Dt}-t/\tau}}{8\pi^2}\left[\int_{-\infty}^{\infty} i\beta\, e^{-Dt\beta^2}\,\mathrm{d}\beta + \int_{-\infty}^{\infty}\frac{r}{2Dt}\,e^{-Dt\beta^2}\,\mathrm{d}\beta\right] \\ &= \frac{e^{-\frac{r^2}{4Dt}-t/\tau}}{8\pi^2}\frac{r}{2Dt}\sqrt{\frac{\pi}{Dt}} \\ &= \frac{r}{(4\pi Dt)^{3/2}}e^{-\frac{r^2}{4Dt}-t/\tau}. \end{aligned} \tag{5.78}$$

Finally, to get the Green's function $G(r,t)$ the reduced Green's function $g(r,t)$ is divided by r and the result is obtained:

$$G(r,t) = \frac{1}{(4\pi Dt)^{3/2}}e^{-\frac{r^2}{4Dt}-t/\tau}. \tag{5.79}$$

Applying the Green's function in 3D

To apply the Green's function method in three dimensions, the definition of $G(r,t)$, as given by Eq. (5.79), is slightly adjusted to read as follows:

$$G_{3D}(\mathbf{r}-\mathbf{r}',t-t') = \left(\frac{1}{4\pi D(t-t')}\right)^{3/2}\exp\left(-\frac{(\mathbf{r}-\mathbf{r}')^2}{4D(t-t')}-\frac{t-t'}{\tau}\right). \tag{5.80}$$

The term $(\mathbf{r}-\mathbf{r}')^2$ can be rewritten as $r^2+r'^2-2rr'\cos\theta$ due to the spherical symmetry of the problem and this is inserted into Eq. (5.63)

$$\begin{aligned} n_2(r,t) = \frac{2}{\tau_1}\int\left(\frac{1}{4\pi D_2(t-t')}\right)^{3/2}\exp\left(-\frac{r^2+r'^2-2rr'\cos\theta}{4D_2(t-t')}-\frac{t-t'}{\tau_2}\right) \\ \times\, n_1(r',t')r'^2\,\mathrm{d}r'\,\mathrm{d}t'\sin\theta\,\mathrm{d}\theta\,\mathrm{d}\phi\,, \end{aligned} \tag{5.81}$$

where $r'^2\sin\theta$ is the Jacobian for integration in spherical coordinates.

The angular components of the integral in Eq. (5.81) can be evaluated analytically. The integral over ϕ gives

$$\int_0^{2\pi} d\phi = 2\pi \tag{5.82}$$

and with the identity

$$\int_0^{\pi}\exp(A\cos\theta)\sin\theta\,\mathrm{d}\theta = \frac{2\sinh A}{A} \tag{5.83}$$

the integral over θ gives

$$\int_0^{\pi}\exp\left(\frac{2rr'\cos\theta}{4D_2(t-t')}\right)\sin\theta\,\mathrm{d}\theta = 2\sinh\left(\frac{2rr'}{4D_2(t-t')}\right)\frac{4D_2(t-t')}{2rr'}. \tag{5.84}$$

Inserting these results and collecting the terms, Eq. (5.81) then becomes

$$n_2(r,t) = \frac{4}{\tau_1 r}\int\left(\frac{1}{4\pi D_2(t-t')}\right)^{1/2}\exp\left(-\frac{r^2+r'^2}{4D_2(t-t')}-\frac{t-t'}{\tau_2}\right) \times n_1(r',t')r'\sinh\left(\frac{2rr'}{4D_2(t-t')}\right)\mathrm{d}r'\,\mathrm{d}t' \tag{5.85}$$

which is the result for $n_2(r,t)$ using the Green's function method in the homogeneous case. The integral over r' and t' should be done numerically.

5.1.4 Diffusion equation of second-generation electrons — inhomogeneous case

In the inhomogeneous case of the coated AuNP, the second-generation number density was not found analytically and the solution was instead approximated by solving Eq. (5.85) separately for the inside and outside regions to find $n_{2\mathrm{i}}(r,t)$ and $n_{2\mathrm{o}}(r,t)$, using the corresponding diffusion coefficients D and average lifetimes τ and restricting the domains of r and r' to the respective region. The integrals over r' and t' were solved numerically using MATHEMATICA with the domain of t' being in both cases from 0_+ to t while the range on r' is restricted to the region in question, that is, from 0_+ to R for the inner region and R to ∞ for the outer region.

5.2 CALCULATING MEAN FREE PATHS

The description of electron transport as a diffusion process requires a parametrization of the interaction between the electrons and the medium in which they move. The two governing parameters needed for the diffusion model applied for the present framework are the diffusion coefficient D and the average lifetime τ of the electrons which are in turn defined by the elastic and inelastic scattering mean free paths, λ_{el} and λ_{inel}, respectively, by the relations

$$D = \frac{v\lambda_{\mathrm{el}}}{6} \tag{5.86}$$

$$\tau = \frac{\lambda_{\mathrm{inel}}}{v}, \tag{5.87}$$

where v is the electron velocity. The mean free path is a measure of the average distance traveled by a moving particle between collisions and it follows therefore that a large elastic mean free path leads to a high diffusion coefficient, whereas a large inelastic mean free path leads to a larger average lifetime of the particle before inelastically scattering.

Closely related to the concept of scattering mean free paths is that of scattering cross sections which describe the probability of a scattering event taking place between a projectile and a target. The relationship between the microscopic scattering cross section σ and the scattering mean free path λ can be illustrated by the following argument. Imagine that the probability of an incoming particle interacting with the scattering center is σ, then the average number of scattering events n after traversing a distance $\mathrm{d}x$ is given

by $n = \mathcal{N}\sigma\,\mathrm{d}x$, where $\mathcal{N}$ is the density of scatterers. By setting $n = 1$ the mean free path λ is found as the distance traveled between each collision $\mathrm{d}x = \lambda$ and the macroscopic scattering cross section Λ is defined as the inverse mean free path or, equivalently, the density of scatterers times their cross section [170, 171]:

$$\Lambda = \frac{1}{\lambda} = \mathcal{N}\sigma. \tag{5.88}$$

In this section, the procedure for calculating the elastic and inelastic scattering cross sections for the materials in our system, namely gold, liquid water, and the PEG coating medium is summarized. While an accurate calculation of cross sections, especially for very low-energy electrons, is a complex task and should include quantum mechanical calculations [172–174], this goes beyond the scope of this work. Since the overall framework presented in this chapter relies on several approximations the aim is therefore instead to provide reasonable estimates of the cross sections within the accuracy of the framework.

5.2.1 Inelastic cross section

This section briefly summarizes some of the work carried by de Vera *et al.* published e.g. in Refs. [78, 79, 175] and outlines how it may be applied to the present study.

For the inelastic collisions of low-energy electrons, the electronic excitations and ionizations are considered as the main component of the energy loss above about 20 eV but an estimate for the vibrational excitations of the water and coating molecules, which will begin to dominate at lower energies, is also taken into account [176, 177]. The electronic excitation spectrum of a medium irradiated by a charged particle can be calculated within the dielectric formalism as introduced by Lindhard [178]. In this framework, the charged particle interacts with the electron gas of the target material described by its complex dielectric function $\epsilon(\Delta\varepsilon, q)$, where $\Delta\varepsilon$ and $\hbar q$ are the transferred energy and momentum from the projectile to the target electrons, respectively. The main ingredient in the dielectric formalism is the electronic excitation spectrum represented by the energy-loss function (ELF) which is given by $\mathrm{Im}\left[-1/\epsilon(\Delta\varepsilon, q)\right]$. Knowing the ELF, the macroscopic inelastic scattering cross section for an electron projectile is then given by [79, 165]

$$\Lambda(E)_{\mathrm{inel}} = \frac{1}{\lambda_{\mathrm{inel}}} = \int_{\Delta\varepsilon_-}^{\Delta\varepsilon_+}\int_{q_-}^{q_+} f_{\mathrm{ex}}\frac{e^2}{\hbar\pi}\frac{m}{Eq}\,\mathrm{Im}\left[-1/\epsilon(\Delta\varepsilon, q)\right]\mathrm{d}q\,\mathrm{d}\Delta\varepsilon\,, \tag{5.89}$$

where E is the energy of the electron, m is the mass of the projectile, and f_{ex} is the exchange factor which accounts for the indistinguishability of the incident and the emitted electrons which is important to take into account for low energies. The integration limits for the momentum transfer are given by $q_\pm = \sqrt{2m}\left(\sqrt{E} \pm \sqrt{E - \Delta\varepsilon}\right)$ from energy and momentum conservation laws while the limits for energy transfer are from 0 to E depending on the type of excitation [78, 179]. In the case of ionization, $\Delta\varepsilon_- = I_p$ and $\Delta\varepsilon_+ = (T + I_p)/2$, where I_p is the ionization threshold, T is the energy of the electron emitted as

Table 5.1: The average chemical formula, mean mass density $\bar{\rho}$, and mean atomic number of the coating $\bar{Z}_t$ for the two coatings considered comprising of 32 and 60 PEG molecules, respectively.

N_{PEG}	Chemical formula	$\bar{\rho}$ (g/cm^3)	$\bar{Z}_t$
32	$C_{18.2}H_{146.4}O_{61.2}N_{1.4}S_{1.0}$	0.99	3.38
60	$C_{16.9}H_{107.3}O_{42.4}N_{1.4}S_{1.0}$	1.08	3.39

a result of the ionization, and the factor $1/2$ is due to the indistinguishability of the incident and emitted electrons [180].

It is in general difficult to find experimental values of the optical ELF for a specific coating material due to the large number of available coating designs and because the coatings usually will contain varying amounts of water after solvation. Recently, however, it was shown by Tan *et al.* that due to a common feature of organic materials of having a prominent peak around 20 eV, the optical ELF for organic materials can be parametrized to a good approximation as a single Drude-type function [181]

$$\mathrm{Im}\left[-1/\epsilon(\Delta\varepsilon, q=0)\right] = \frac{a(\bar{Z}_t)(\Delta\varepsilon)}{\left[(\Delta\varepsilon)^2 - b(\bar{Z}_t)^2\right]^2 + c(\bar{Z}_t)^2(\Delta\varepsilon)^2}, \tag{5.90}$$

where $a(\bar{Z}_t)$, $b(\bar{Z}_t)$, and $c(\bar{Z}_t)$ represent the height, position, and width of the peak as a function of the mean atomic number of the target material $\bar{Z}_t$. With this approach the ELF of an arbitrary organic material can be estimated theoretically which was recently shown to be a good approximation [78].

From the calculations of the PEG-coated AuNPs performed in Chapter 3, the mean mass density $\bar{\rho}$ and mean atomic number of the coating region $\bar{Z}_t$ were calculated, see Table 5.1. For liquid water and gold experimental values for the optical limit ELF were obtained from Refs. [182] and [183]. They are shown in Fig. 5.2 together with the ELFs calculated for PEG 32 and PEG 60. Note the similar behavior of the PEG coatings and water with the PEG coatings being about 10 % different from each other due to their different average densities.

The ELF was extended beyond the optical limit ($q = 0$), following Garcia-Molina, Abril and co-workers, by using the Mermin Energy-Loss Function–Generalized Oscillator Strength (MELF-GOS) dispersion algorithm [184, 185], which has been shown to produce accurate electronic excitation cross sections for a variety of materials [78, 186]. Once the full ELF is known it is possible to calculate the inverse inelastic mean free path using Eq. (5.89).

The dielectric formalism loses accuracy for low energies (below about 100 eV) and other inelastic channels in addition to electronic interactions become increasingly important with the main channel being vibrational excitations. The estimate for the inelastic mean free paths for low energies, used in this chapter, therefore relied on experimental values for the inelastic mean free path below about 20 eV for all the materials. For gold, the theoretical estimates performed well down to about 16 eV below which the results were extended by interpolating data points from experiments [187, 188], see Fig. 5.3. For water, the calculated curve is in reasonably good agreement with experimental data for ice [189] while for lower energies the

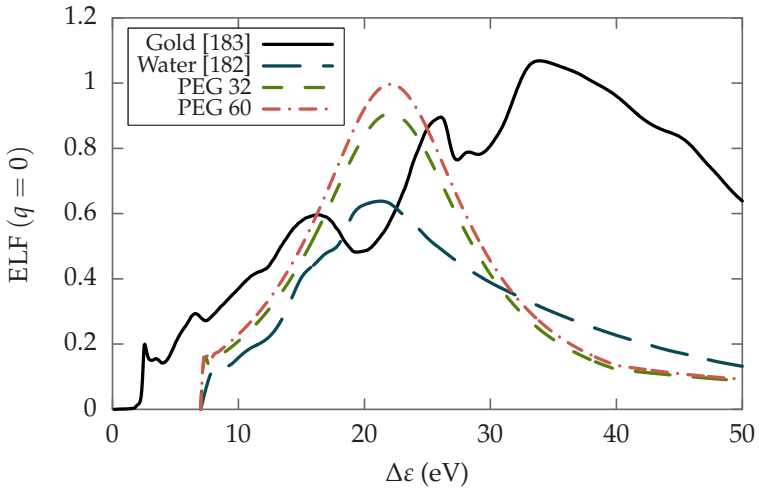

Figure 5.2: Energy-loss function ELF of gold, liquid water, and two PEG coatings of different density (composed of 32 and 60 molecules) in the optical limit ($q = 0$) versus transferred energy $\Delta\varepsilon$. The ELF of liquid water is obtained from inelastic X-ray scattering data [182] and for gold from its optical properties [183].

recommended cross sections from Itikawa & Mason were added to the calculated electronic cross sections [177]. The result is seen to be in reasonable agreement with the experimental data for ice at low energies. Vibrational data was not available for the coatings so their vibrational excitation cross sections were assumed to be the same as for water and the same procedure for obtaining the inelastic mean free path at very low energies was followed. The resulting inelastic mean free paths are shown in Fig. 5.3 and the corresponding values for the average lifetime is given in Table 5.2.

5.2.2 Elastic cross section

The elastic scattering cross sections can be calculated for intermediate and high energies in a relatively straightforward manner using the atomic cross sections of the atoms in the material but this procedure might not hold when the energy of the electrons becomes so low that the electron wavelength becomes comparable to the interatomic distances [192]. However, it is shown below that the atomic cross sections do in fact provide a reasonable approximation for the calculation of the elastic mean free path in the present case. Elastic scattering cross sections of electrons with atoms may be calculated using a method called partial-wave analysis [166, 193] and there are a number of resources for obtaining these cross sections, for example the NIST database [194] or the ELSEPA code [166]. For the calculations in this work, the latter was used since it allows cross sections to be calculated to down to incident electron energies of about 10 eV which is lower than what is available in the NIST database.

The scattering of electrons by atoms can be described by a central potential of the form [166, 193]

$$V(r) = V_{\text{st}}(r) + V_{\text{ex}}(r) + V_{\text{cp}}(r) - iW_{\text{abs}}(r), \tag{5.91}$$

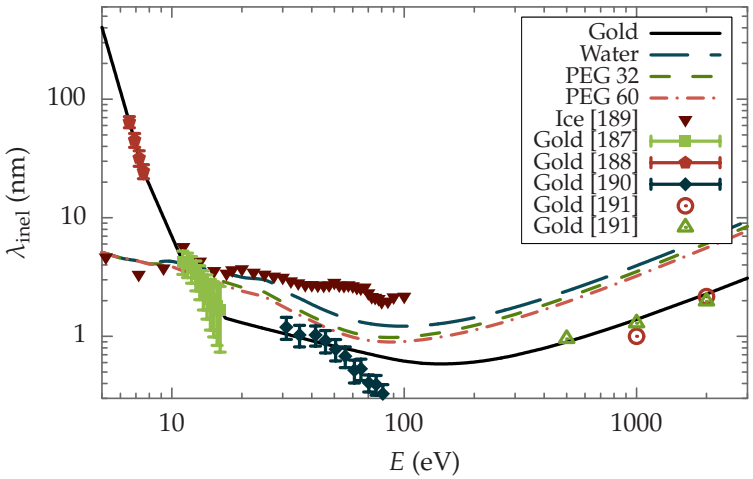

Figure 5.3: Inelastic scattering mean free path λ_{inel} of electrons in gold, liquid water, and two PEG coatings versus energy of the electron E. Lines represent compiled data from calculations within the dielectric formalism (for high energies) and experimental data (for low energies), as explained in the text. Symbols are experimental data for ice [189] and gold [187, 188, 190, 191].

where $V_{\text{st}}(r)$, $V_{\text{ex}}(r)$, and $V_{\text{cp}}(r)$ are the electrostatic, exchange, and correlation-polarization potentials, respectively, and $W_{\text{abs}}(r)$ is the magnitude of the imaginary absorption potential. The Coulumb interaction is represented in the electrostatic potential while $V_{\text{ex}}(r)$ accounts for the electron indistinguishability and $V_{\text{cp}}(r)$ accounts for correlation and induced polarization of the atom. Lastly, the absorption term accounts for the loss of electrons from the elastic channel through inelastic scattering. When aiming to reproduce experimental results using the ELSEPA code this term should be included, but for the purposes of the present work, where the ELSEPA code is used to calculate elastic mean free paths only, this term was switched off since the inelastic mean free path was already explicitly calculated above.

Applying the assumption that the elastic scattering in the coating medium can be described by the atomic cross sections, the coating medium was assumed to be made up by a solid "average coating molecule" with chemical formula and mean mass density $\bar{\rho}$ listed in Table 5.1. By summing up the atomic scattering cross sections, scaled by their stoichiometries, the microscopic scattering cross section σ_{el} of the coating region can then be approximated. The macroscopic elastic scattering cross section Λ_{el} is then calculated using Eq. (5.88), where the number density $\mathcal{N}$ of the coating medium is calculated as the mean mass density $\bar{\rho}$ divided by the mean mass of the molecule.

The results for the calculation down to 10 eV for gold, liquid water, and the two PEG coatings are shown in Fig. 5.4 together with a recommendation for water vapor (density scaled to liquid water) based on a collection of theoretical and experimental results [177]. Below 10 eV the curves were extrapolated. The result for water agrees well with the recommended data for the whole range, which indicates that the extrapolation below 10 eV is a fair approximation also for gold. The two PEG coatings are quite similar

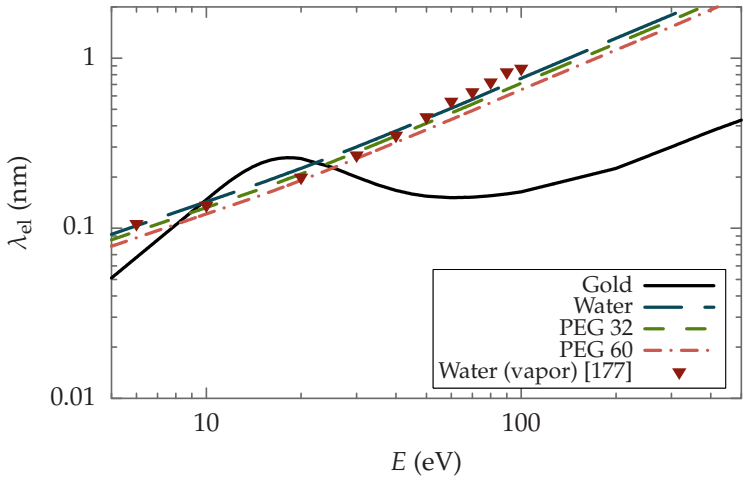

Figure 5.4: Elastic scattering mean free path λ_{el} of electrons in liquid water, gold, and two PEG coatings versus electron energy E. Lines represent calculations within relativistic partial-wave analysis while symbols are recommended data for water [177].

Table 5.2: The diffusion coefficient D (in $nm^2\,fs^{-1}$) and average lifetime τ (in fs) for 5 eV and 25 eV-electrons in gold, the coating medium formed with 32 and 60 PEG molecules, and in pure water.

		Material			
Energy	Quantity	Gold	PEG 32	PEG 60	Water
5 eV	D	0.011	0.020	0.018	0.020
	τ	304	3.84	3.84	3.84
25 eV	D	0.11	0.12	0.11	0.13
	τ	0.39	0.80	0.73	1.01

to water because of their similar densities and chemical compositions. The resulting diffusion coefficients are listed in Table 5.2.

5.3 PRODUCTION OF SECONDARY ELECTRONS

Having both derived the solution to the diffusion equation and calculated the scattering mean free paths, the next step in this framework is to estimate the number of low-energy electrons produced as a result of excitations in the AuNP by a passing ion. The governing mechanisms for the production of low-energy electrons (energy below about 50 eV) from AuNPs were recently revealed by Verkhovtsev *et al.* to be collective electron excitations in the NP, namely plasmon-type excitations of delocalized valence electrons and giant resonance effects caused by excitations of 5*d* electrons in individual atoms of the NP [51, 52].

To demonstrate this, the photoabsorption cross section up to about 60 eV was calculated for small gold clusters of 18 to 42 atoms using time-dependent density functional theory (TDDFT) and was shown to exhibit two striking

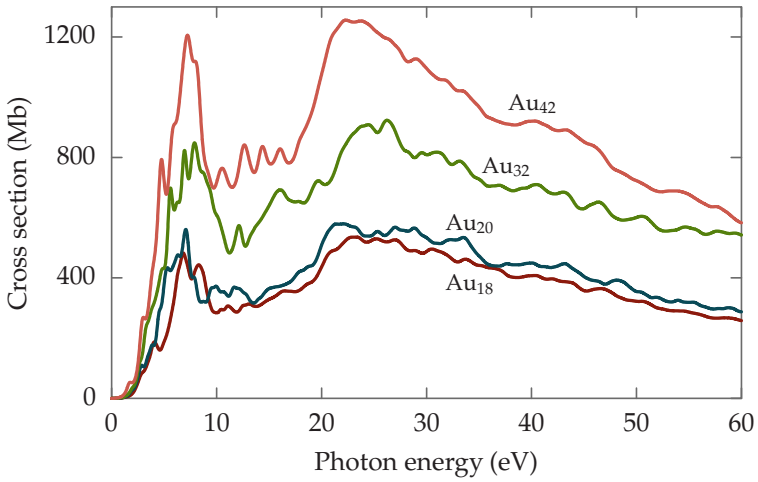

Figure 5.5: Photoabsorption cross sections for the gold clusters Au_{18}, Au_{20}, Au_{32}, and Au_{42} calculated with TDDFT versus photon energy. Data taken from Ref. [52].

features independent of cluster size: A narrow peak centered around 6 eV and a broader peak situated around 22 eV, see Fig. 5.5. Applying the theory of the plasmon resonance approximation (PRA), the first peak was explained as a result of plasmon excitations in the NP whereas the broader peak was explained as atomic giant resonance effects. By integrating the oscillator strength over the energy range up to the ionization threshold of the $5p$ electrons (about 60 eV), which do not take part in the giant resonance excitations, it was shown that about 1.5 and 8 electrons from each atom contribute to the plasmon-type resonance and the giant resonance, respectively. This accounts for about 85 % of the 11 valence electrons per atom and on this basis it was concluded that the total photoabsorption spectrum of small AuNPs can be approximated as a sum of the plasmon and the $5d$ contributions.

The electron production resulting from the relaxation of both types of excitations was calculated based on parameters extracted from fits to the two peaks in the TDDFT-calculated photoionization spectrum which allows for a quantification of the number of produced electrons and their energy spectrum as a function of ion impact kinematics (ion energy and collision distance).

In this section, the formalism of collective electron excitations in AuNPs, detailed originally in Refs. [52, 195–197], is summarized and the main results relevant to this chapter are outlined. Atomic units, $\hbar = m_e = |e| = 1$, are used throughout this section.

5.3.1 Theoretical formalism

To describe the resonance behavior in the photoionization cross section at low energies the PRA was utilized in which this excitation is described as a plasmon type excitation with cross section σ_{pl}. In the case of a spherically

symmetric system it is directly related to the imaginary part of the dynamic polarizability $\alpha(\omega)$ of the system

$$\sigma_{\mathrm{pl}}(\omega) = \frac{4\pi\omega}{c} \operatorname{Im} \alpha(\omega), \tag{5.92}$$

where ω is the photon energy and c is the speed of light. The dynamic polarizability of the system has a resonant behavior at the frequencies where the collective excitation modes of the electrons are excited and the photoionization cross section can be shown to be proportional to a profile given given by the relation

$$\sigma_{\mathrm{pl}}(\omega) \propto \frac{\omega^2\Gamma}{(\omega^2 - \omega_{\mathrm{r}}^2)^2 + \omega^2\Gamma}, \tag{5.93}$$

where ω_{r} is the resonance frequency and Γ is its width.

The delocalized electrons of solid atomic clusters may form two distinct types of plasmon excitations, namely the volume plasmon and the surface plasmon. Taking into account the angular multipolarity of the plasmon, the resonance frequency of the surface plasmon $\omega_l^{(\mathrm{s})}$ is given by

$$\omega_l^{(\mathrm{s})} = \left(1 - \frac{1}{2l+1}\sqrt{1 + 4l(l+1)R^{2l+1}}\right)^{1/2} \frac{\omega^{(\mathrm{v})}}{\sqrt{2}}, \tag{5.94}$$

where l is the multipole angular momentum of the mode, R is the radius of the NP, and $\omega^{(\mathrm{v})}$ is the resonance frequency of the volume plasmon given by

$$\omega^{(\mathrm{v})} = \sqrt{\frac{3N}{R^3}}, \tag{5.95}$$

with N being the total number of delocalized electrons in the system. Only the dipole ($l = 1$) is considered for photoionization [196] in which case Eq. (5.94) reduces to

$$\omega^{(\mathrm{s})} = \left[\frac{N}{2R^3}\left(3 - \sqrt{1 + 8R^3}\right)\right]^{1/2}. \tag{5.96}$$

Using this frequency as the surface plasmon resonance frequency, the resonance profile given by Eq. (5.93) was fitted to the TDDFT data for the lowest energy peak and the width Γ was extracted to be used in calculating the electron production, as described in the following section. The result of the fit is shown in Fig. 5.6.

In the case of giant resonance caused by $5d$ electrons in individual atoms, the photoionization cross section $\sigma_{5d}(\omega)$ can be fitted by a Fano resonance profile [198]

$$\sigma_{5d}(\omega) \propto \frac{(\Gamma_{5d} + \omega - \omega_{5d})^2}{(\Gamma_{5d}/2)^2 + (\omega - \omega_{5d})^2}, \tag{5.97}$$

where ω_{5d} is the resonance frequency and Γ_{5d} is its width. Using a function of this shape, the TDDFT data was fitted from 20.2 eV to 57.2 eV which corresponds to the ionization threshold of the $5d$ shell to the ionization threshold of the $5p$ shell of atomic gold. The result of the fit of the $5d$ giant resonance contribution is shown in Fig. 5.6.

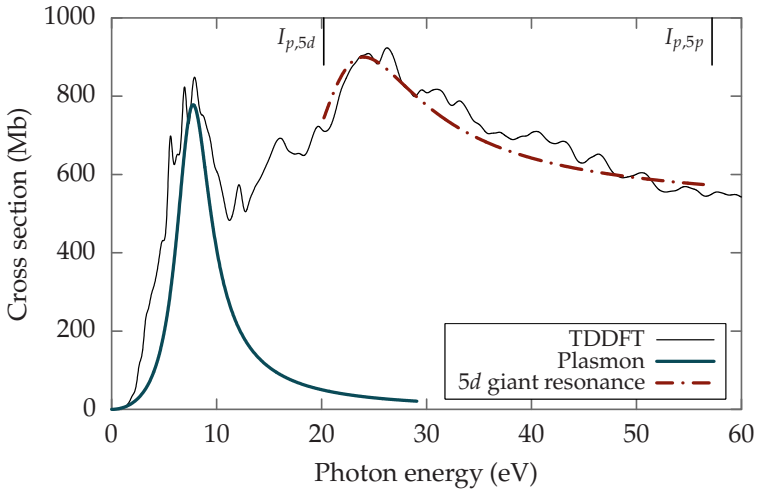

Figure 5.6: Photoabsorption cross section versus photon energy calculated with TDDFT for a Au_{32} cluster and fits of the two major contributions: Plasmon-type excitation (by Eq. (5.93)) and the 5*d* giant resonance excitation (by Eq. (5.97)). The 5*d* giant resonance is fitted in the interval between the ionization threshold I_p of the 5*d* shell and the 5*p* shell with limits indicated by vertical lines. Data taken from Ref. [52].

5.3.2 Electron production

The resonance peak for the plasmon excitation at about 6.3 eV is situated above the ionization potential of the Au_{32} cluster, $I_p = 5.7\,\text{eV}$, as calculated by TDDFT calculations. Excitations located above I_p can then decay via ionization processes while those located below the ionization threshold will decay via electron-phonon coupling leading to vibrations of the ionic core. The 5*d* resonance peak lies entirely above the ionization threshold and will completely result in ionization processes.

To quantify the electron production as a result of ion irradiation, the inelastic scattering cross section σ, which describes the probability of an inelastic scattering event occurring due to the incident ion, is calculated. Inelastic scattering implies that an amount of energy $\Delta\varepsilon$ is transferred to the target by the ion and the probability of causing ionization can then be related to the transferred energy $\Delta\varepsilon$. Below it is shown how the differential scattering cross section per deposited energy per scattering angle is calculated and how the electron production as a result of inelastic scattering can be determined for the plasmon excitation and the giant resonance excitation.

Plasmon excitation

The differential scattering cross section for the plasmon excitations integrated over all scattering angles $\Omega_{\mathbf{p}_2}$ is given by

$$\frac{\mathrm{d}\sigma_{\mathrm{pl}}}{\mathrm{d}\Delta\varepsilon} = \int \mathrm{d}\Omega_{\mathbf{p}_2} \frac{\mathrm{d}^2\sigma_{\mathrm{pl}}}{\mathrm{d}\Delta\varepsilon\,\mathrm{d}\Omega_{\mathbf{p}_2}} = \frac{2\pi}{p_1 p_2} \int_{q_{\min}}^{q_{\max}} q\,\mathrm{d}q \frac{\mathrm{d}^2\sigma_{\mathrm{pl}}}{\mathrm{d}\Delta\varepsilon\,\mathrm{d}\Omega_{\mathbf{p}_2}}, \tag{5.98}$$

where $\Omega_{\mathbf{p}_2}$ is the solid angle of scattering, $\mathbf{p_1}$ and $\mathbf{p_2}$ are the initial and final momenta of the projectile, respectively, and $\mathbf{q} = \mathbf{p_1} - \mathbf{p_2}$ is the transferred

momentum. The doubly differential inelastic scattering cross section of the plasmon excitation can be written as a sum of the inelastic scattering cross section for the surface and the volume plasmon

$$\frac{\mathrm{d}^2\sigma_{\mathrm{pl}}}{\mathrm{d}\Delta\varepsilon\,\mathrm{d}\Omega_{\mathbf{p}_2}} = \frac{\mathrm{d}^2\sigma_{\mathrm{pl}}^{(\mathrm{s})}}{\mathrm{d}\Delta\varepsilon\,\mathrm{d}\Omega_{\mathbf{p}_2}} + \frac{\mathrm{d}^2\sigma_{\mathrm{pl}}^{(\mathrm{v})}}{\mathrm{d}\Delta\varepsilon\,\mathrm{d}\Omega_{\mathbf{p}_2}} \tag{5.99}$$

which are both expanded as a sum over the multipole contributions with angular momentum l

$$\begin{aligned}\frac{\mathrm{d}^2\sigma_{\mathrm{pl}}^{(\mathrm{s})}}{\mathrm{d}\Delta\varepsilon\,\mathrm{d}\Omega_{\mathbf{p}_2}} &\propto \sum_l \frac{\omega_l^{(\mathrm{s})2}\Gamma_l^{(\mathrm{s})}}{\left(\omega^2-\omega_l^{(\mathrm{s})2}\right)^2+\omega^2\Gamma_l^{(\mathrm{s})2}} \\ \frac{\mathrm{d}^2\sigma_{\mathrm{pl}}^{(\mathrm{v})}}{\mathrm{d}\Delta\varepsilon\,\mathrm{d}\Omega_{\mathbf{p}_2}} &\propto \sum_l \frac{\omega^{(\mathrm{v})2}\Gamma_l^{(\mathrm{v})}}{\left(\omega^2-\omega^{(\mathrm{v})2}\right)^2+\omega^2\Gamma_l^{(\mathrm{v})2}}.\end{aligned} \tag{5.100}$$

The resonance widths Γ_l for these terms were derived by the ratio γ_l of the width of the plasmon resonance to its frequency such that $\gamma_l^{(\mathrm{s})} = \Gamma_l^{(\mathrm{s})}/\omega_l^{(\mathrm{s})} = 0.6$ for all multipole terms for the surface plasmon and $\gamma_l^{(\mathrm{v})} = \Gamma_l^{(\mathrm{v})}/\omega^{(\mathrm{v})} = 1.0$ for the volume plasmon [52]. The upper limit in l is decided by the following argument: If the wavelength of the plasmon $\lambda_{\mathrm{pl}} = 2\pi R/l$ becomes smaller than the wavelength of an electron on the Fermi surface $\lambda_{\mathrm{e}} = 2\pi/\sqrt{2I_p}$, where I_p is the ionization threshold of the system, then it is more likely that the electron excitations will be formed by single-electron transitions than collective excitations [195, 196]. In this analysis the dipole ($l = 1$), quadrupole ($l = 2$), and octupole ($l = 3$) terms are thus included.

The differential cross section is redefined as a function of the energy E of the emitted electrons to directly calculate the energy spectrum of electrons emitted via the plasmon excitation mechanism. The energy of the emitted electrons E is related to the transferred energy $\Delta\varepsilon$ by the incident particle and the ionization threshold I_p as $E = \Delta\varepsilon - I_p$. The differential cross section can then be redefined as the probability to produce $N_{\mathrm{e}}^{\mathrm{pl}}$ electrons with energy E emitted from a segment $\mathrm{d}x$ by

$$\frac{\mathrm{d}^2N_{\mathrm{e}}^{\mathrm{pl}}}{\mathrm{d}x\,\mathrm{d}E} = \frac{1}{V}\frac{\mathrm{d}\sigma_{\mathrm{pl}}}{\mathrm{d}E}, \tag{5.101}$$

where V is the volume of the NP.

The number of electrons produced per distance $\mathrm{d}x$ per energy $\mathrm{d}E$ via the plasmon excitation mechanism from a 1.6 nm "naked" (meaning, with no coating) AuNP irradiated with a 0.3 MeV/u carbon ion was calculated and shown in Fig. 5.7. Also shown for comparison is the number of electrons produced under 0.1 MeV/u and 1.0 MeV/u ion irradiation. From the figure it is apparent that the main contribution to the very low-energy electrons comes from the surface plasmon while the volume plasmon contributes the majority of the produced electrons above about 4 eV. It is also evident that the majority of the electrons produced via the plasmon excitation mechanism have energies in the range 0 eV to 20 eV. By integrating Eq. (5.101) over the kinetic energy range of the emitted electrons $\mathrm{d}N_{\mathrm{e}}^{\mathrm{pl}}/\mathrm{d}x$ is obtained which

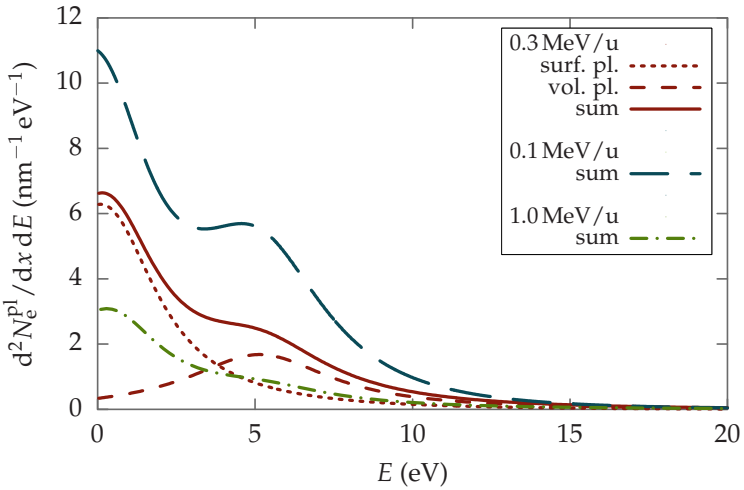

Figure 5.7: Number of electrons $\mathrm{d}^2N_\mathrm{e}^\mathrm{pl}$ / $\mathrm{d}x\,\mathrm{d}E$ per unit length $\mathrm{d}x$ per unit energy $\mathrm{d}E$ with energy E produced via the plasmon excitation mechanism from a 1.6 nm diameter AuNP irradiated by carbon ions of three different energies as indicated. For the 0.3 MeV/u case, dotted and dashed curves show the contributions of the surface and the volume plasmons, respectively.

can be interpreted as the characteristic distance $\mathrm{d}x$ the ion should traverse to ionize the NP via the plasmon mechanism. For a 0.3 MeV/u-ion this distance is $\mathrm{d}x = 0.03$ nm which means that the ion induces the emission of about 50 electrons due to the relaxation of plasmon excitations during the passage of the 1.6 nm AuNP. The traversal takes about $t = v_\mathrm{ion}/D_\mathrm{NP} = 0.2$ fs, where D_NP is the NP diameter, which is similar to the lifetime of the dipole plasmon resonance of about about 0.19 fs defined as its inverse width, $\tau_\mathrm{pl} = 1/\Gamma = R/(3lv_\mathrm{F})$ where R is the radius of the NP, l is the multipolarity, and v_F is the velocity of the NP valence electrons on the Fermi surface [199]. Since the velocity of the emitted low-energy electrons is about an order of magnitude smaller than the velocity of the ion it is therefore possible to neglect the charge state of the NP during the ion passage and assume that the ion interacts with a neutral target.

The characteristic collision distance d is determined by the ratio of the velocity of the ion v_ion and the transferred energy $\Delta\varepsilon$ by $d = v_\mathrm{ion}/\Delta\varepsilon$ [195, 196]. For a 0.3 MeV/u-ion (velocity about 3.5 au) with a characteristic energy transfer of about 5 eV (about 0.2 au) the collision distance is about 18 au or $d = 0.9$ nm which corresponds to a distance of 0.1 nm from the surface of the NP. The collision distance will be important in Section 5.4.4 where the effect of ion energy on the production of radicals is investigated.

Giant resonance excitation

In the case of the giant resonance the differential inelastic scattering cross section is given by

$$\frac{\mathrm{d}\sigma_{5d}}{\mathrm{d}\Delta\varepsilon} = \frac{2Z^2c}{\pi\Delta\varepsilon v_\mathrm{ion}^2}\sigma_{5d}(\Delta\varepsilon)\ln\left(\frac{v_\mathrm{ion}}{\Delta\varepsilon R_{5d}}\right), \tag{5.102}$$

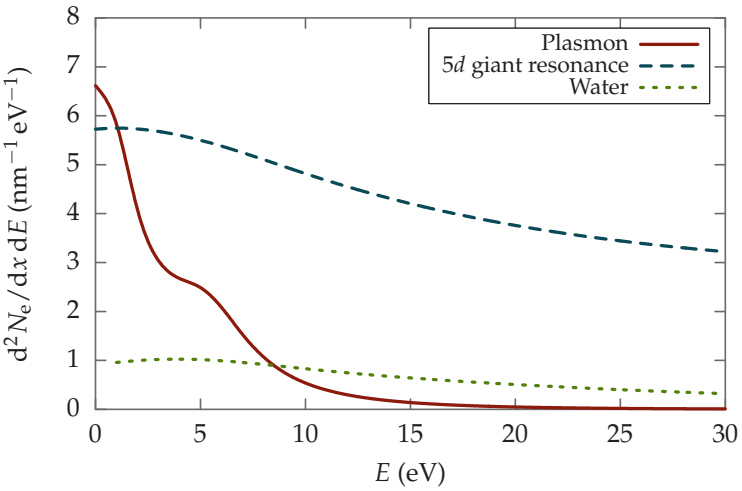

Figure 5.8: Number of electrons d^2N_e / $\mathrm{d}x\,\mathrm{d}E$ per unit length $\mathrm{d}x$ per unit energy $\mathrm{d}E$ with energy E produced via the plasmon excitation and the $5d$ excitation mechanisms in the 1.6 nm AuNP irradiated by a 0.3 MeV/u C^{6+} ion. Also shown is the number of electrons generated along the equivalent segment of ion track in liquid water, calculated as outlined in Ref. [78].

where Z and v_ion are the charge and the velocity of the projectile, respectively, and R_{5d} is the characteristic radius of the $5d$ shell. One can then estimate the number of electrons N_e^{5d} produced by the $5d$ excitations per unit length $\mathrm{d}x$ in energy range $\mathrm{d}E$ by the expression

$$\frac{\mathrm{d}^2N_\mathrm{e}^{5d}}{\mathrm{d}x\,\mathrm{d}E} = An\frac{\mathrm{d}\sigma_{5d}}{\mathrm{d}E}, \tag{5.103}$$

where n is the atomic density of the NP and $A = N_{5d}/N_\mathrm{tot}$ is the ratio of the number of atoms N_{5d} which take part in the excitation to the total number of atoms in the NP N_tot. This follows from the fact that only those atoms within a cylindrical shell around the ion track from $r_\mathrm{min} \approx R_{5d}$ to $r_\mathrm{max} \approx v_\mathrm{ion}/\Delta\varepsilon$ will be excited simultaneously via the giant resonance mechanism [52]. For a typical energy transfer via the $5d$ excitation mechanism of about $\Delta\varepsilon = 22\,\mathrm{eV}$ the cylinder outer radius $r_\mathrm{max} = 0.23\,\mathrm{nm}$. This is comparable with the nearest-neighbor distance in small gold clusters (0.29 nm) [200] and it can therefore be assumed that only those atoms located on the ion track are excited at this ion energy. For higher ion energies, more atoms will be excited as discussed in Section 5.4.

In order to highlight the effect of $5d$ excitations the number of electrons emitted per unit length per unit energy $\mathrm{d}^2N_\mathrm{e}^{5d}$ / $\mathrm{d}x\,\mathrm{d}E$ was averaged over different positions of the ion track ranging from a central collision to the glancing collision. The result is presented in Fig. 5.8 which shows the number of electrons produced by the plasmon and $5d$ excitation mechanisms of the NP as well as the number of electrons produced by ionization in water of a segment of the ion path with a similar track length.

5.4 RESULTS AND DISCUSSION

For the analysis of the diffusion of electrons emitted from the NP, the number of electrons emitted in the energy range 0 eV to 10 eV and those in the energy range 10 eV to 30 eV were quantified. The first group are produced as a result of both plasmon type excitations and giant resonance effects while the latter are produced mainly due to the giant resonance effects. The diffusion of these two groups is approximated by representing them as two populations with a characteristic energy of 5 eV and 25 eV, respectively, with corresponding values of the diffusion coefficient and average lifetimes listed in Table 5.2.

In Section 5.4.1 the calculated number densities of first-generation electrons of both energies are presented while in Section 5.4.2 the results related to the second-generation electrons produced due to inelastic collisions by the first-generation electrons with energy 25 eV are presented. The inelastic scattering of first-generation electrons with energy 5 eV is assumed in this model not to lead to the production of new electrons because their energy is below the ionization threshold of water and PEG.

In Section 5.4.3 the production of radicals resulting from the inelastic scattering of first-generation electrons and direct ionization of the medium by the passing carbon ion of energy 0.3 MeV/u, corresponding to the Bragg peak region, is analyzed. For both sources of radicals, the water content of the coating is taken into account in the case of 32 and 60 PEGs attached to the NP as calculated in Chapter 3.

Finally, in Section 5.4.4 the dependence of the radical production on the structural parameters of the NP and the ion energy is analyzed and in Section 5.5 the findings of this chapter are concluded.

5.4.1 Diffusion of first-generation electrons

The number of emitted electrons with the two energies 5 eV and 25 eV was calculated as $N_e^{5\,eV} = 118$ and $N_e^{25\,eV} = 138$, respectively, using the methodology discussed in Section 5.3. Inserting these numbers with the according values for the diffusion coefficient D and average lifetime τ, listed in Table 5.2, the number density of first-generation electrons $n_1(r,t)$ was found for the two energies by numerically solving Eq. (5.85) for the inner and outer regions. The result for the case 32 PEG molecules attached to the surface is shown in Fig. 5.9 at various time instances t.

Due to the random collisions of the electrons they diffuse away from the surface at a rate given by the diffusion coefficient. Since the 25 eV-electrons have a diffusion coefficient about six times larger than that of the 5 eV-electrons, a faster broadening of the density is observed. On the other hand the average lifetime of the 5 eV-electrons is about five times greater than that of the 25 eV-electrons which means that the exponential decay of the electron number density due to inelastic collisions with the medium is slower and it therefore takes a longer time before the electrons are completely extinct.

The coating thickness was taken to be 1.4 nm based on the results from Chapter 3. To estimate the number of electrons which are able to escape the

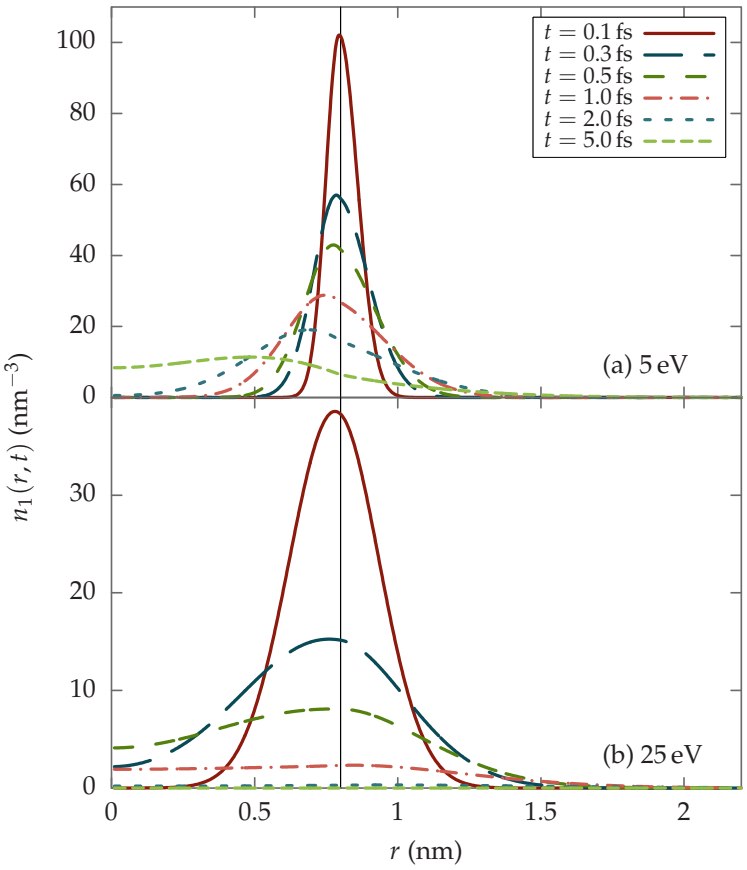

Figure 5.9: Number density of first-generation electrons $n_1(r,t)$ of energy (a) 5 eV and (b) 25 eV at various time instances t versus distance from the NP center r for the PEG 32 coating. The times indicated correspond to both panels.

Table 5.3: Fluence $F(r)$ of first-generation electrons evaluated at the end of the coating ($r - R = 1.4\,\text{nm}$) for the two coatings PEG 32 and PEG 60 as well as with no coating normalized to the case of no coating.

	Coating medium		
Energy	PEG 32	PEG 60	No coating
5 eV	1.0	0.65	1.0
25 eV	0.53	0.35	1.0

coating without experiencing an inelastic collision the integral fluence $F(r)$ (from here on just called fluence) of first-generation electrons integrated over the area of a sphere with radius r was calculated as a function of distance from the NP surface $r - R$. Defining the flux of electrons $J(r,t)$ from Fick's first law

$$J(r,t) = -D\frac{\partial n(r,t)}{\partial r} \tag{5.104}$$

the fluence is then given by

$$F(r) = \int_0^\infty 4\pi r^2 J(r,t)\,\mathrm{d}t\,. \tag{5.105}$$

The calculations were done for the case of PEG 32 and PEG 60 coatings as well as for the "naked" AuNP (that is, with no coating). The fluence evaluated at the end of the coating for the two electron populations are presented in Table 5.3, where the numbers are normalized to the case of no coating.

The fluence evaluated at the coating boundary is identical for 5 eV-electrons traveling in pure water and in PEG 32 because the diffusion coefficient and average lifetime were comparable for these media. In PEG 60 the diffusion coefficient is lower than in PEG 32 which leads to a lower fluence at the coating boundary compared to that of PEG 32 and pure water by about 35 %. For 5 eV-electrons the diffusion coefficient and average lifetime are lower in both coatings compared to water which leads to a reduction in the fluence at the coating boundary of about 47 % and 65 % for PEG 32 and PEG 60, respectively.

It should be stressed, however, that in all cases the vast majority of the emitted electrons undergo inelastic collisions in the coating region with just about 1 % of the emitted electrons escaping through purely elastic collisions.

5.4.2 Diffusion of second-generation electrons

In the present model, we consider the population of 25 eV-electrons capable of producing second-generation electrons as a result of inelastic collisions. As mentioned in Section 5.1.3, each of such inelastic collisions produces two second-generation electrons. If a mean ionization energy $\bar{B}$ for the valence electrons of the coating medium of 15 eV is assumed[2] then the

2 This value was estimated from *ab initio* calculations of the PEG molecule and its value is close to that of liquid water.

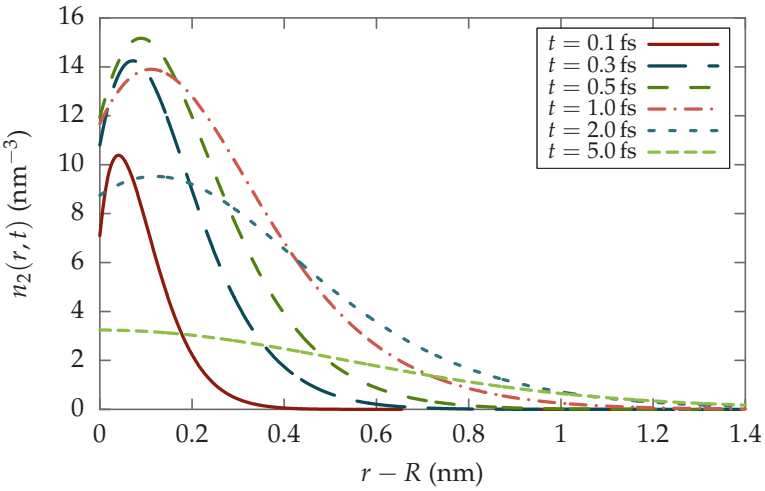

Figure 5.10: Number density of 5 eV second-generation electrons $n_{2o}(r,t)$ in PEG 32 versus distance from the NP surface $r - R$ for various time instances t.

remaining 10 eV is split evenly (as discussed in Section 5.2) such that the two second-generation electrons each have an energy of 5 eV.

Using Eq. (5.85) with D and τ taken from Table 5.2 the number density of second-generation electrons in the coating medium $n_{2o}(r,t)$, for the case of PEG 32, was calculated, see Fig. 5.10. Initially the density increases with time as the first-generation electrons are inelastically scattering thereby leading to the production of second-generation electrons. A maximum is reached after about 0.5 fs after which the inelastic scattering of the second generation outweighs their generation. Despite the lower diffusion coefficient of 5 eV-electrons, the number density profile is significantly broader than that of both populations of first-generation electrons because of the fact that second-generation electrons may have their origin in the whole coating region. This results in a substantial contribution to the total integral fluence in the coating as can be seen in Fig. 5.11 which shows the fluence of the first-generation electrons of energy 25 eV, second-generation electrons, and their sum in the top panel, while the bottom panel shows the sum for the coatings PEG 32 and PEG 60 as well as for the naked NP. Because the number density of the second-generation electrons is maximum about 0.1 nm to 0.2 nm outside the NP core, as seen in Fig. 5.10, there is a flux of electrons towards the NP surface leading to a negative fluence of electrons close to the NP core. This is the reason why the sum of fluences is slightly lower than the first-generation fluence at small distances from the NP in Fig. 5.11 (a).

5.4.3 Radical production

In this model, when electrons of energy 25 eV inelastically collide with the coating medium to produce second-generation electrons, they may also electronically excite or ionize a water molecule which may then dissociate through different channels to produce an OH radical [77, 201, 202]. Low-energy electrons with energy below the ionization potential of water may also contribute to the production of water radicals through the process of

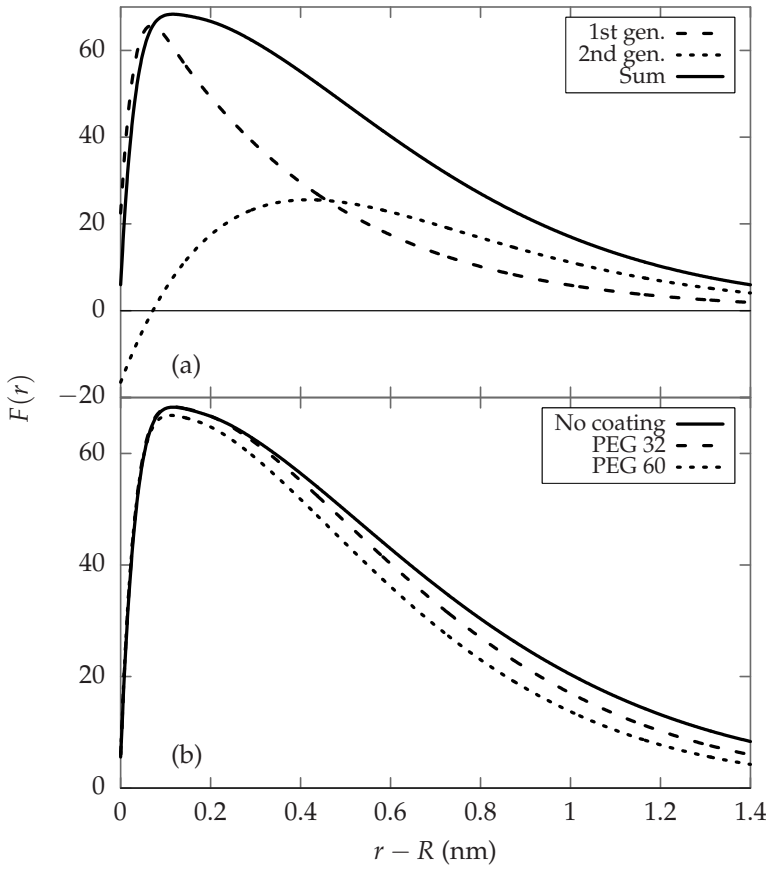

Figure 5.11: Fluence $F(r)$ versus distance from the NP surface $r - R$ of (a) the first and second-generation electrons and their sum in PEG 32 and of (b) sums of fluence due to first and second-generation electrons in PEG 32, PEG 60, and for no coating.

dissociative electron attachment (DEA) [50]. This source may in principle be included in this framework since cross sections for DEA can be calculated or taken from experiments [177, 203, 204]. However, since the probability of attachment to water is small (less than 10^{-4}) [30] this contribution is neglected in the current framework. Additionally the dissociation pathways of inelastic collisions of electrons with the PEG molecules were not part of this research and any products of such collisions are therefore not included in this analysis.

One of the results of Chapter 3 was that the water content in the coating region varies considerably with the number of PEG molecules attached to the NP surface. This finding is included in the calculation of radical production by a probability factor of an electron encountering a water molecule in the coating. This probability $\alpha(r)$ is defined as the ratio of the mass density of water to the total mass density as a function of distance r from the NP surface

$$\alpha(r) = \frac{\rho_{H_2O}(r)}{\rho_{H_2O}(r) + \rho_{PEG}(r)}. \tag{5.106}$$

The production rate of radicals at position r and time t is then given by the lifetime of those first-generation electrons with sufficient energy multiplied by the probability of colliding with a water molecule

$$\frac{\partial n_{OH}(r,t)}{\partial t} = \frac{n_{1,E>I_p}(r,t)}{\tau_{1o}}\alpha(r). \tag{5.107}$$

The number density of radicals $n_{OH}(r,t)$ is found by integrating the production rate over time

$$n_{OH}(r,t) = \int_0^t \mathrm{d}t' \, \frac{n_{1,E>I_p}(r,t')}{\tau_{1o}}\alpha(r). \tag{5.108}$$

Taking the integration limit on time t long enough that all first-generation electrons have inelastically scattered then the number density of OH radicals will be converged. Additionally since the diffusion coefficient of OH radicals is several orders of magnitude smaller than that of the electrons considered in this framework [77], the radicals may be approximated as frozen for the timescales relevant to this analysis and treat n_{OH} as dependent on r only, $n_{OH}(r,t) \equiv n_{OH}(r)$.

The number density of radicals $n_{OH}(r)$ is shown in Fig. 5.12 for the two coatings PEG 32 and PEG 60 as well as for no coating. The coating has a dramatic effect on the production of radicals, especially for the PEG 60 coating. The reason can be found by comparing Figs. 3.11 and 5.9. Water is absent from the first 0.3 nm from surface of the NP in both coatings while this is where most first-generation electrons inelastically scatter. As a result most inelastic collisions will be with PEG molecules rather than water molecules leading to a significantly reduced total radical production compared to a NP without coating where water is naturally present at the NP surface.

To quantify this reduction the number of radicals produced due to inelastic collisions of electrons emitted from the NP N_{OH}^{NP} is calculated. This is done by integrating $n_{OH}(r)$ over the coating region ($r = R$ to $r = R + t_{coat}$) and adding to it the number of electrons which escape the coating $F(R + t_{coat})$,

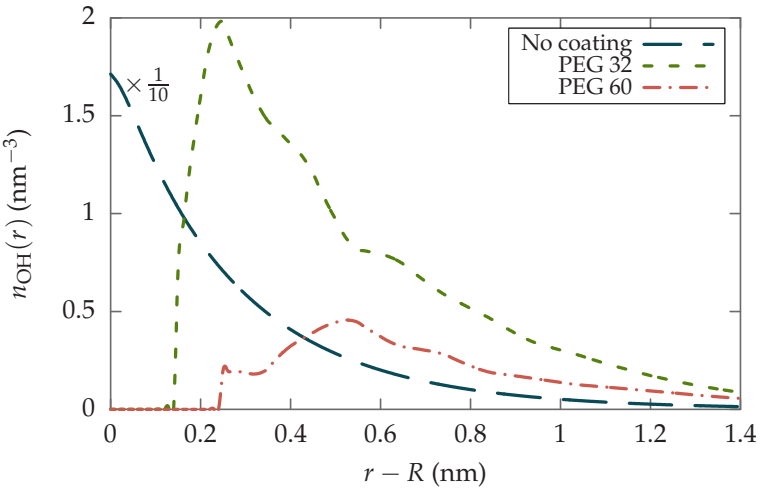

Figure 5.12: Number density of radicals $n_{OH}(r)$ produced by inelastic scattering of first-generation electrons of energy 25 eV in the coating region versus distance from the NP surface $r - R$ for coatings PEG 32 and PEG 60 as well as for no coating (no coating line has been scaled by 1/10).

since they are assumed to all inelastically scatter with water outside the coating,

$$N_{OH}^{NP} = F(R + t_{coat}) + \int_{R}^{R+t_{coat}} dr\, 4\pi r^2 n_{OH}(r). \tag{5.109}$$

Inserting $n_{OH}(r, t)$ calculated for the 25 eV-electrons and adding the fluence at the coating boundary as given in Table 5.3 the number of OH radicals produced from the NP is $N_{OH}^{NP} = 21.8$ for PEG 32. For the case of PEG 60 and no coating the numbers are 8.6 and 75.1, respectively.

To quantify the total number of produced radicals N_{OH}^{total} it is necessary to include the radicals produced as a result of ionization of the medium along the track of the passing ion N_{OH}^{track}. The ionization of the medium results in hydrolysis of water molecules along the ion track, which may lead to radical production, as well as emission of electrons which may collide with other water molecules to further increase the production of radicals.

As an example an ion passing by the NP core at a distance of 0.1 nm from the surface, which corresponds to the maximum plasmon resonance excitation for an ion of energy 0.3 MeV/u, as discussed in Section 5.3, is considered. To take into account the varying water content of the coatings, a probability factor similar to $\alpha(r)$ defined above is included, only in this case the situation is simplified by taking an average probability $\bar{\alpha}$ since the distance of the ion to the NP surface varies during the passage. This is done in the following way:

The total track length L of the ion's path through the coating when passing the NP at a distance d from the NP surface, considering the coating has a thickness t_{coat} and the NP core has radius R, is given by

$$L = 2\sqrt{(R + t_{coat})^2 - (R + d)^2}, \tag{5.110}$$

see illustration in Fig. 5.13. The radial distance from the center of the NP to the ion varies as the ion passes through the coating. When it is halfway

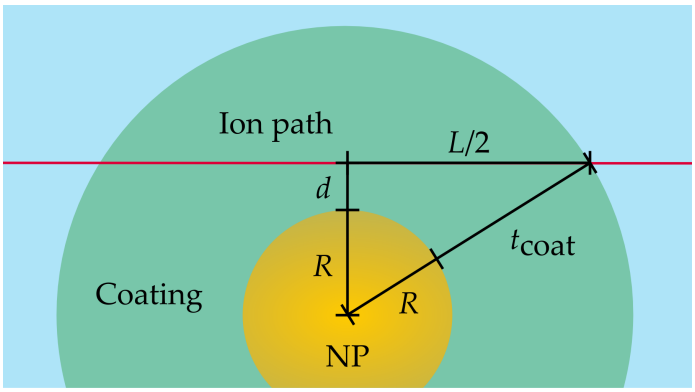

Figure 5.13: Illustration of the geometry of the ion track length, defined in Eq. (5.110), through the coating of thickness t_{coat} a distance d from the AuNP core which has radius R.

through the coating the distance is simply $R + d$ and when it is at the edge of the coating it is given by $R + t_{coat}$. When the ion is a distance l from the halfway point through the coating, the radial distance r is given by

$$r(l) = \sqrt{l^2 + (R + d)^2}. \tag{5.111}$$

The mean radial distance $\bar{r}$ is then found by $\bar{r} = \int_0^L r(l)\,\mathrm{d}l\,/L$. This finally allows for a definition of an average water content of the coating on the path of the ion as $\bar{\alpha} \equiv \alpha(\bar{r})$. For an ion passing the NP at a distance $d = 0.1\,\mathrm{nm}$ one finds $\bar{r} = 0.6\,\mathrm{nm}$ and thus $\bar{\alpha}_{\mathrm{PEG32}} = 0.49$ and $\bar{\alpha}_{\mathrm{PEG60}} = 0.22$. In the case of no coating $\bar{\alpha}_{\mathrm{naked}} = 1.0$ by definition.

The number of radicals produced along the track is then calculated as the average water content $\bar{\alpha}$ multiplied by the sum of (i) the number of ionization events produced by the passing ion and (ii) those radicals produced by inelastic collisions of the electrons produced by the ionization of the ion which have sufficient energy to cause hydrolysis:

$$N_{\mathrm{OH}}^{\mathrm{track},i} = L\left(\int_0^{30\,\mathrm{eV}} \mathrm{d}E\,\frac{\mathrm{d}^2 N_{\mathrm{e}}^{\mathrm{track}}}{\mathrm{d}x\,\mathrm{d}E} + \int_{I_p}^{30\,\mathrm{eV}} \mathrm{d}E\,\frac{\mathrm{d}^2 N_{\mathrm{e}}^{\mathrm{track}}}{\mathrm{d}x\,\mathrm{d}E}\right)\bar{\alpha}_i, \tag{5.112}$$

where i denotes the coating medium either PEG 32, PEG 60, or no coating, and the two terms on the r.h.s. correspond to the contributions (i) and (ii) mentioned above, differing only in the lower integration limit, and I_p is the ionization threshold of water. The term $\mathrm{d}^2 N_{\mathrm{e}}^{\mathrm{track}}/\,\mathrm{d}x\,\mathrm{d}E$ denotes the number of electrons produced per distance $\mathrm{d}x$ within an energy range $\mathrm{d}E$. This was calculated using the method described in Ref. [78]. The upper limit in energy is taken as 30 eV to compare with the number of electrons emitted from the NP which also had an upper limit of about 30 eV in the current framework. For a carbon ion of energy 0.3 MeV/u traveling in water the number of electrons produced per nanometer in the range 0 eV to 30 eV is $\mathrm{d}N_{\mathrm{e}}^{\mathrm{track}}/\,\mathrm{d}x = 19\,\mathrm{nm}^{-1}$ while 9 of those have energies above I_p. In this picture transport of the electrons produced along the track is not calculated and it is assumed to a first approximation that they collide with water molecules with a probability given by the average water content $\bar{\alpha}$.

Inserting $\bar{\alpha}_i$ for the different coating media, the number of electrons produced along the track is $N_{\mathrm{OH}}^{\mathrm{track},i} = 48.3$, 24.3, and 112.4 for $i =$ PEG 32, PEG

Table 5.4: Total radical yield due to inelastic scattering of first-generation electrons of energy 25 eV emitted from the AuNP plus the radicals produced due to hydrolysis around the ion track for the coatings PEG 32 and PEG 60 as well as for no coating. This is compared with the number of radicals produced by an ion traversing a similar distance in pure water. Also shown is the relative radical yield normalized to the case of an ion traversing a similar track length in pure water.

	PEG 32	PEG 60	No coating	Water
$N_{\mathrm{OH}}^{\mathrm{total}}$	70.1	32.9	187.5	112.4
Relative radical yield	0.62	0.29	1.67	1

60, and no coating (pure water), respectively. The total number of produced radicals is then the sum of those produced along the track and those produced due to electrons emitted from the NP surface $N_{\mathrm{OH}}^{\mathrm{total}} = N_{\mathrm{OH}}^{\mathrm{track}} + N_{\mathrm{OH}}^{\mathrm{NP}}$. This number should be compared with the number of radicals produced along the track in pure water which is 112.4. The results are presented in Table 5.4.

The presence of a coating has a clear negative effect on the production of radicals for both PEG 32 and PEG 60 coatings which in fact cause a suppression of the generation of radicals compared to pure water, meaning that the presence of the NP actually reduces overall radical yield. For the denser PEG 60 coating the larger volume devoid of water close to the surface leads to a reduction of more than 70 % compared to the case of no NP present. The fact that there is a significant enhancement in the case of no coating illustrates the importance of having water close to the NP surface. Considering Fig. 5.9, water should be present inside of the first 0.4 nm from the NP surface in order to maximize the radical yield due to emitted electrons.

These results are in accordance with the experimental findings by Gilles *et al.* who also found decreasing radical yield for increasingly dense PEG coatings on AuNPs [34]. Among the experiments performed by the authors considered two PEG coatings with different molecular weights (1000 Da and 4000 Da) but similar thicknesses (2.3 nm and 1.9 nm) and surface densities (2.7 nm^{-2} and 1.9 nm^{-2}). Observing a six-fold decrease in the radical production from the 4000 Da-coating, it was concluded that the main factor was the atomic number density of the coating which was about four times greater than the in the 1000 Da-case. It should be mentioned that the experimental conditions were different from the ones simulated here: The PEG molecules were between 4 and 16 times longer, the AuNP core was about 32 nm in diameter, and the experiments were performed with 17.5 keV X-rays. The fact that similar conclusions were reached may indicate that the reduced radical yield by NPs with dense PEG coatings is not restricted to any particular NP design or radiation modality but that the lack of water close to the surface will reduce the radical yield for any system.

5.4.4 Production of electrons and radicals at different projectile energies and coating compositions

In the previous section the radical yield for the case of a AuNP coated with 32 or 60 PEG molecules as well as with no coating, irradiated by a 0.3 MeV/u C^{6+} ion, was analyzed. For the two coated cases the result was a radical production smaller than in the case of no NP present due to the lack of water at the surface of the coated NPs. In this section, the dependence of the radical production on the structural parameters of the PEG coating and on the ion impact kinematics is explored. In particular the relationship between the production of low-energy electrons and the ion energy and how the water content of the coating affects the total radical production is studied.

Varying ion energy

We begin by varying the ion energy in the range 0.3 MeV/u to 10 MeV/u. Increasing the ion energy affects a number of interaction mechanisms. First, the characteristic collision distance d for the maximum plasmon excitation depends on the ion velocity, as discussed in Section 5.3.2, as $d = v_{\text{ion}}/\Delta\varepsilon$, where v_{ion} is the ion velocity and $\Delta\varepsilon$ is the transferred energy. Increasing the ion energy from 0.3 MeV/u to 1.0 MeV/u increases the collision distance from the NP surface, $d - R$, from about 0.1 nm to 0.85 nm which has two effects: (i) The average radial distance of the ion from the NP surface is increased and since the average water content increases with radial distance from the NP, the production of radicals along the ion track $N_{\text{OH}}^{\text{track}}$ is therefore increased accordingly. For ions of energy 5.0 MeV/u and 10.0 MeV/u the ion track is completely outside the coating and will therefore be located in pure water. And (ii) the increased distance from the NP decreases the electron production via the plasmon mechanism, as shown in Fig. 5.7 and discussed in Section 5.3.

Second, since atoms within a cylinder of radius $r_{\text{max}} \approx v_{\text{ion}}/\Delta\varepsilon$ are excited via the giant resonance effect, an increase of the ion energy will lead to an increase in the number of atoms N_{5d} which are excited. However this is counteracted for large ion energies by the fact that the production of electrons depends inversely on v_{ion}^2 (see Eqs. (5.102) and (5.103)).

And finally, the ionization cross section for water decreases with increasing ion energy (also due to an inverse dependence on v_{ion}^2) which results in a lower production of radicals both along the track in the coating but also in the pure water medium. Since the base of comparison for the relative radical yield is then lowered with increasing ion energy, the result is a strongly enhanced low-energy electron production relative to the production from water when the energy of the ion exceeds that of the Bragg peak region. The results are summarized in Table 5.5 and shown in Fig. 5.14.

Varying coating average hydration

Let us now turn to the effect of the water content in the coating. For the calculation of the number of OH radicals produced along the ion track $N_{\text{OH}}^{\text{track}}$ as it passes through the coating, defined in Eq. (5.112), an average water content $\bar{\alpha}$ was defined. Using the average water content now as a free pa-

Table 5.5: Total relative radical yield due to the presence of the AuNP calculated for various ion energies and coating media as well as for no coating compared to the case of no NP present.

	Coating medium		
Ion energy (MeV/u)	PEG 32	PEG 60	No coating
0.3	0.62	0.29	1.67
1.0	1.39	0.66	3.0
5.0	6.5	3.2	20.0
10.0	9.0	4.1	28.5

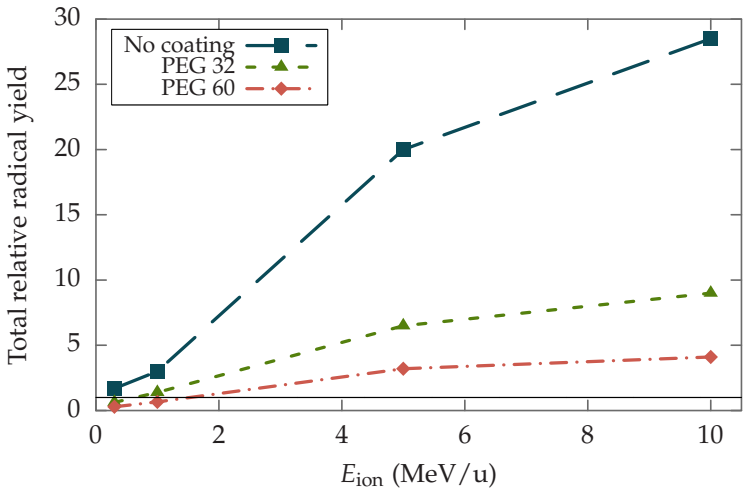

Figure 5.14: Total relative radical yield compared to having no NP present versus the ion projectile energy E_{ion} for PEG 32 and PEG 60 coating medium as well as for no coating. A horizontal line is drawn at a relative yield equal to one. Lines connecting the points are meant only to guide the eye.

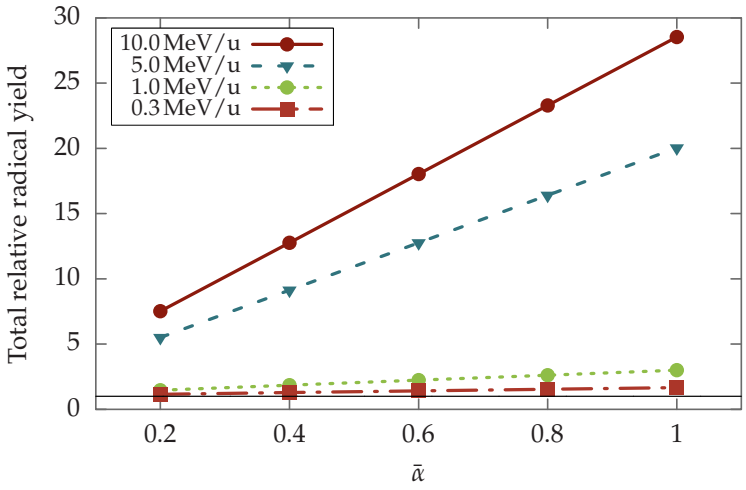

Figure 5.15: Total relative radical yield compared to having no NP present versus average water content $\bar{\alpha}$ of the coating region assuming a homogeneous material estimated for different ion energies. A horizontal line is drawn a relative yield equal to one. Lines connecting the points are meant only to guide the eye.

rameter for both the production of radicals along the ion track and for the radicals produced due to inelastic collisions of electrons emitted from the NP (that is, replacing $\alpha(r)$ by $\bar{\alpha}$ in Eq. (5.108)), the effect of the water content of the coating on the total production of radicals can be illustrated. The density of first-generation electrons $n_1(r,t)$ calculated for the case of no coating was used in Eq. (5.108) since there was no data for the case where the coating medium has a uniform average water content. The density profiles were rather similar for all simulated coating media so this approximation should have a negligible effect on the end result. The average water content $\bar{\alpha}$ was varied between 0.2 and 1.0, the latter corresponding to the case of no coating, and the resulting total production of radicals for ion energies between 0.3 MeV/u and 10.0 MeV/u was calculated. The results are shown in Fig. 5.15

When approximating the coating with an average water content, the result is a relative radical yield larger than one for all cases because even in the lowest water content simulated ($\bar{\alpha} = 0.2$) there will be water at the surface of the NP. For the ion energy $E_{\text{ion}} = 0.3\,\text{MeV/u}$, corresponding to the Bragg peak region, the relative radical yield only grows slightly from 1.2 to 1.7 when increasing the relative average water content from 0.2 to 1.0 because the production of radicals in pure water is relatively high at this energy. This picture changes drastically at higher ion energies. For an ion energy of $E_{\text{ion}} = 10.0\,\text{MeV/u}$ the relative radical yield is 7.5 even for the lowest water content and increases to about 28.5 for the case of no coating. These results clearly indicate the importance of having water present at the NP surface. This should be carefully considered when designing coatings for NPs intended as radiosensitizing agents.

5.5 CONCLUSION

In this chapter a comprehensive framework for modeling the radiosensitizing capabilities of coated NPs due to the emission of low-energy electrons induced by carbon ion irradiation was presented. The framework comprised several distinct theoretical and numerical methods: (i) MD simulations of the coating structure and water content, (ii) quantification of the number and energy of low-energy, secondary electrons emitted from the NP core as a result of collective electron excitations arising from ion irradiation evaluated by the plasmon resonance approximation, (iii) calculation of the elastic and inelastic scattering cross sections of electrons traveling in the gold core, the coating medium, and in water by means of the dielectric formalism and partial-wave analysis, and finally (iv) development of a diffusion model for the transport of the emitted electrons through the coating and a numerical solution for first and second-generation electrons.

The methodology presented in this chapter is general and may be applied to any NP core coated by organic molecules to investigate the radical production due to ion radiation interaction. This framework complements the Monte Carlo approach, which is commonly applied for studying the radiosensitization properties of NPs due to electrons with energies in the range of 10^2 eV to 10^3 eV, by accounting for the transport of low-energy electrons and many-body phenomena such as collective electron excitations in the metal core.

The framework was applied to the case of a 1.6 nm AuNP coated by PEG molecules of two different surface densities (32 and 60 PEG molecules attached, respectively) and irradiated by a 0.3 MeV/u carbon ion (corresponding to the energy of the Bragg peak region) while calculating the diffusion of emitted electrons with two characteristic energies (5 eV and 25 eV) considered as representing electrons emitted mainly due to the plasmon excitation and the giant resonance, respectively. It was shown that nearly all electrons emitted from the NP surface undergo an inelastic collision inside the coating medium with the vast majority inelastically scattering within just 0.3 nm from the surface. The lack of water molecules in this region for both coated NPs was shown to be detrimental to the OH radical production via electrons emitted from the NP, and therefore the radiosensitizing capabilities of such a NP, with the two studied cases showing a suppression in the relative radical yield, compared to the case of no NP present, of 47 % and 71 %, respectively, rather than a radiosensitizing effect.

The effect of ion energy on the radical production was studied by varying the ion energy between 0.3 MeV/u and 10.0 MeV/u and it was shown that the relative radical yield, compared to having no NP present, increases with increasing ion energy. When the ion energy exceeds that of an ion in the Bragg peak region, corresponding to the entrance channel of the ion track, an increase in the radical production, compared to having no NP present, is possible even for the most densely coated NPs considered.

The effect of the water content of the coating was studied by assuming a homogeneous coating medium with varying average water content. It was demonstrated that the presence of water at the NP surface outweighs the importance for an overall well hydrated coating when considering the

radical production since most electrons inelastically scatter close to the NP surface. The recommendation is therefore to apply coatings in such a way as to be permeable to water all the way to the NP surface in order to increase radical production.

6 CONCLUSIONS AND FUTURE WORK

This thesis has been devoted to a theoretical investigation of the structural properties of coated nanoparticles (NPs) intended for use as radiosensitizing agents during cancer radiotherapy. While significant research efforts have focused on investigating the mechanisms of radiosensitization by NPs and how to optimize the NP design, previous theoretical studies have largely ignored the effect of coating the NP on the radiosensitization. However, NPs are always coated *in vivo* and their coating has been demonstrated to reduce the radical production caused by irradiation of these NPs. It is therefore important to include the coating in "complete" simulations in order to accurately model properties of such NPs.

This thesis seeks to provide a convenient means of including the coating in simulations of NPs for radiotherapy scenarios to enable a more efficient design process of coated NP systems and to investigate the structural properties that play key roles in determining whether such a coated NP will be an efficient radiosensitizer. Three main areas have been investigated namely; the detailed structure and water content of the coating, the energetics of the coating formation, and the effect of the presence of a coating and its structure on the radiosensitizing abilities of ion-irradiated NPs. We have considered the case of a poly(ethylene glycol) (PEG) coated gold NP (AuNP) due to its common use in experiments. However, one of the main points of this work is that the presented methodology is completely general and may be applied in a straight forward manner to any other core-coating combination using the methodologies outlined in this thesis.

After introducing the field and the problems addressed in this thesis in Chapter 1 and overviewing the applied methodology in Chapter 2 original results obtained in the three areas listed above were presented in Chapters 3 to 5.

In Chapter 3 a 1.6 nm AuNP coated with between 4 and 60 PEG molecules each consisting of five monomers was modeled. This range of molecules corresponds to surface densities reported experimentally. This chapter presented how to set up and anneal the metal core, how to obtain and prepare input files for organic coating molecules, how to attach them evenly to the NP surface, and how to make and equilibrate a surrounding water box and thus established a convenient methodology for the detailed structural analysis of any coated NP system by the use of molecular dynamics simulations. First, it was demonstrated that the total thickness of the coating was fluctuating between around 1.3 nm and 1.45 nm with no clear dependence on the number of attached PEG molecules which contradicts the prediction of the theoretical framework by de Gennes which is commonly used by experimentalists to evaluate the conformation of PEG coatings for a given coating surface density. In that framework, a low surface density leads to a semi-spherical conformation of the polymer while a high density

leads to a more linear conformation due to the mutual repulsion of the polymers. It was demonstrated that the attached PEG molecules were in a mixed state between these two conformations due to the curvature of the spherical NP which provides greater conformational freedom for the tails of the PEG molecules than a flat surface. The total size of coated NPs is important for *in vivo* applications because cell uptake and stability in the blood stream depend on it and it is therefore important to be able to accurately predict the size of a given coated NP system when making choices about the design of the NP and its coating. Second, it was demonstrated that the water content of the PEG coating is dependent on the number of attached PEG molecules such that increasing the number of PEG molecules on the NP decreased the amount of water in the coating, especially near the NP surface. Besides playing a role in the protective abilities of the PEG coating, the water content has been demonstrated to be important for the radiosensitizing abilities of coated NPs [33, 34]. The results of this chapter have been published in Ref. [205].

In Chapter 4 two different analyses of the energetics involved with the formation of the PEG coating were performed. Simplifying the situation to a single PEG molecule adsorbing on a flat Au surface the free energy-change associated with the adsorption was quantified by performing a metadynamics simulation which directly calculated the free-energy surface in the direction perpendicular to the Au surface. The free energy change was found to be $-1.27\,\text{eV}$. This was compared with a semi-analytical calculation of the Helmholtz free-energy change associated with the binding of the PEG molecule. The Helmholtz free-energy was evaluated by calculating the potential energy contribution from molecular dynamics simulations and the entropy contribution from an approximated theoretical viewpoint. It was found that the potential energy contribution ($-3.16\,\text{eV}$) dominated over the entropy contribution ($0.29\,\text{eV}$) and that the binding was favorable ($-2.87\,\text{eV}$). In both cases the calculated binding strength was somewhere between physisorption (about $0.3\,\text{eV}$) and covalent binding (about $3\,\text{eV}$ to $9\,\text{eV}$). There may be a number of reasons for the relatively large discrepancy between these two values: (i) Only translational entropy is taken into account in the semi-analytical method which thus disregards the contributions that would arise from the loss of rotational and conformational entropy associated with being adsorbed to a surface. (ii) The simulated adsorbed state could be in a particular low-energy configuration from which it did not escape during the simulation. This should be investigated by simulating an ensemble of adsorbed configurations. These results are planned for a future publication.

Finally, Chapter 5 presents a comprehensive methodology quantifying the production of low-energy electrons and radicals induced by incident ionizing radiation, and therefore the capability of the coated NP to act as a radiosensitizing agent. The results of the molecular dynamics simulations of PEG-coated AuNPs performed in Chapter 3 are combined with previous work performed by Verkhovtsev *et al.* [51] and de Vera *et al.* [78] on the low-energy electron production from ion-irradiated NPs and the calculation of mean free paths of electrons in organic media and with a diffusion description of the electron transport previously presented by Surdutovich & Solov'yov [77]. The result was a detailed calculation of the production and

diffusion of low-energy electrons emitted from the NP surface into the coating region and a quantification of the radical production of a PEG-coated AuNP under irradiation of carbon ions. Focusing on low-energy electrons (below about 50 eV) two excitation mechanisms of the NP due to the passing ion were considered, namely a plasmon-type excitation and a collective excitation of 5*d* electrons in individual atoms of the NP. This allowed for a quantification of the emitted electrons and their energy spectrum. Using a suitable parametrization of the organic coating medium, the inelastic scattering mean free path of the electrons traveling through the coating medium was calculated using the dielectric formalism. Together with the elastic mean free path, which was calculated using the free software package ELESPA, based on partial-wave analysis, the diffusion coefficient and the average lifetime of the electrons were quantified. The electron transport was modeled as a diffusion process after having derived the solution to the diffusion equation for electrons emitted from a spherical shell into two media (the gold core and the PEG coating). The diffusion of the electrons was approximated by considering the electrons as belonging to one of two families of characteristic energies 5 eV and 25 eV. It was demonstrated that the vast majority (about 99 %) of the emitted electrons undergo an inelastic collision before escaping the coating with most of them inelastically scattering in the first 0.3 nm outside the NP core. Since this region is devoid of water for the two studied coatings (having 32 or 60 PEG molecules attached) the result is a suppression of the production of OH radicals compared to having no NP present because the electrons emitted from the NP surface do not collide with water molecules. The radical production for the PEG 32 and PEG 60 coatings was only 63 % and 29 % compared to having no NP present. By varying the water content of the coating, it was shown that a small but even average water content of the coating leads to a higher radical production than a large average water content if no water is present at the surface. Lastly by varying the ion energy it was found that ion energies exceeding those found in the Bragg peak (0.3 MeV/u) lead to a larger production of radicals. By increasing the ion energy up to 10.0 MeV/u the relative radical yield increased from a suppression of 37 % and 71 % to a yield 9.0 and 4.1 times greater than the case of no NP present for the PEG 32 and PEG 60 coatings, respectively. This framework complements the results of Monte Carlo simulations, which are mainly focused on studying the radiosensitization properties of NPs due to emitted secondary electrons with energies in the range of 10^2 eV to 10^3 eV, by accounting for the transport of low-energy electrons and many-body phenomena such as collective electron excitations in the metal core. The results discussed in this chapter have been submitted for publication (repository version in Ref. [206]).

In conclusion, this thesis has presented a detailed methodology for simulating the thickness and water content of PEG coatings and how these properties can affect the radiosensitizing abilities of such NPs in certain situations as well as the binding energy of PEG molecules to gold surfaces. The critical importance of having water present at the NP surface was demonstrated and that this can be accomplished by applying the least dense coating which will still protect the NP *in vivo*. The presented methodology should allow for a more efficient screening of proposed NP designs by permitting a quantifica-

tion of the radical yield due to low-energy electrons emitted from the NPs due to ion irradiation for varying NP cores, coatings, and ion energies.

6.1 FUTURE WORK

The work presented in this thesis may be continued along several different but equally exciting and interesting avenues.

Having already demonstrated the methodology of simulating the structure of a specific design of PEG-coated AuNPs, it should be straight forward to apply the same procedure to AuNPs of different sizes and shapes as well as different lengths of PEG molecules. This will enable comparisons between a wider selection of experiments and probe the relationship between AuNP size, PEG length, and the water content of the coating. In addition, the precise dependence of the coating structure on the binding sites on the NP surface should be studied. In the presented work, the PEG molecules were evenly distributed but this should be refined to investigate the binding specifically on faces, edges, corners, or defects of the NP surface. Furthermore, the PEG coating *in vivo* is known to be gradually exchanged with proteins present in the biological environment and it is therefore necessary to study the structure of AuNPs coated with such proteins, e.g. glutathione, which is abundant in the cellular environment, or a mixture of PEG molecules with specific targeting proteins which are used in so-called "active targeting" coatings [11, 207]. Lastly, the applied force field should be refined to better parametrize the interactions between the coating molecule and the NP surface to better predict the conformation of the simulated coating as a function of the NP core material.

The energetic stability of the coating could be explored further by performing metadynamics simulations of a surface with pre-adsorbed molecules to study the binding free-energy as a function of finite surface coverages. In this way the free-energy surface will be affected by the presence of other molecules present on the surface which are likely to impose a barrier for adsorption which in turn depends on the surface density of attached molecules. This procedure could be transferred to the case of a coated NP, although in this case the metadynamics simulations will become more challenging due to the geometry of the problem. The semi-analytical approach may instead provide a more suitable method given that the contributions to entropy change from rotational and conformational degrees of freedom may be studied further and included in this model. The presented methodology can be used to study NP coatings formed under various conditions corresponding to synthesis in different temperatures, salt concentrations, and coating molecule concentrations.

The framework for quantifying the production of radicals from an ion-irradiated NP should be extended and refined by calculating the diffusion and radical production from a range of secondary electron energies beyond just the two energies considered in the thesis. The same framework could also be applied to the production of higher energy electrons emitted due to excitation by photons, for example X-ray induced Auger electrons, which is the focus of many experiments and Monte Carlo simulations. For instance it

is expected that inclusion to the model of the more energetic δ-electrons, of energy 100 eV and higher, emitted from a metal NP should lead to a contribution to the radical production in the vicinity of the NP. The ratio between the energy-loss functions for gold and water is about 10 for a transferred energy of 100 eV, and larger for larger transferred energies, which means that one may expect a relative increase of production of δ-electrons of a similar magnitude for a AuNP compared to water. Energetic δ-electrons propagating in water have a range of about 5 nm [208, 209] which means that such electrons will penetrate the coating (of thickness about 1.4 nm) and produce OH radicals in the surrounding water medium. Assuming that each ionization event requires about 15 eV then a δ-electron of 100 eV will produce about 7 OH radicals. Since the number of such electrons emitted from the NP is an order of magnitude larger than that produced in pure water, there will be, at least, an order of magnitude increase in the radical yield due to these electrons. A more elaborate analysis of the radical yield including the effect of δ-electrons should be performed for a more complete picture.

The directions for future work outlined here should be able to refine and improve the methodologies presented in this thesis with the aim to make even better computational tools for the design of radiosensitizing NPs for cancer radiotherapy.

A THE GREEN'S FUNCTION METHOD

The Green's function method is used to study the response $u(x)$ of a system to an impulse $f(x)$. Formally, it says that the convolution of a Green's function G with an arbitrary function $f(x)$ is the solution to the inhomogeneous differential equation for $f(x)$. This means that, given a linear ordinary differential equation in the form $L(u(x)) = f(x)$, where L represents a linear differential operator, one can first solve $L(G(x,s)) = \delta(s-x)$ for all s to find $G(x,s)$. Then the solution to the differential equation can be found by solving the integral $u(x) = \int G(x,s)f(s)\,\mathrm{d}s$, which is called the convolution of the two functions.

In other words, to understand the response of a system to some arbitrary external force, it is sufficient to understand how the system responds to an impulse force (as given by the delta function). In this chapter, we begin with a simple example and then show how the Green's function method can be used to solve the diffusion equation for the second generation of electrons.

A.1 CIRCUIT EXAMPLE

The Green's function method was developed to study electricity and magnetism, so we present here a simple example of using the method for studying the current in an electric circuit.[1]

The current $i(t)$ in a circuit with a resistor R and an inductor L (not to be confused with the general operator L mentioned above) in series driven by the voltage $v(t)$ is given by

$$Li''(t) + Ri(t) = v(t). \tag{A.1}$$

Before we continue, notice that the solution we are looking for ($u(x)$ above) is here the current $i(t)$ (the response), and the impulse to the system ($f(x)$ above) is here $v(t)$ (the voltage driving the system).

If the voltage takes the shape of a delta function $\delta(s-x)$, physically meaning that it is momentarily switched on and off, then the response of the circuit, that is, the current in the circuit $i(t)$, is given by the Green function $G(x,s)$, where s is the moment in time where the impulse acts. With the initial condition that $i(0) = 0$ (no current before switching on voltage), the Green's function can be found and is given by

$$i(t)_{\text{impulse}} = G(t,s) = H(t-s)\frac{\exp\left(-\frac{R(t-s)}{L}\right)}{L}, \tag{A.2}$$

1 This example was taken from this text: http://blog.wolfram.com/2016/03/31/new-in-the-wolfram-language-greenfunction-and-applications-in-electricity-odes-and-pdes/

where $H(t-s)$ is the Heaviside step function. The resulting (impulse) response is described by an instantaneous increase at $t = s$ followed by an exponential decay to 0.

If now we *drive* the system with some other form than a delta function, for example $v(t) = \sin(t)$, then we can use the Green's function given above to find the response of the circuit by the convolution integral

$$i(t) = \int_0^t G(t,s)v(s)ds, \tag{A.3}$$

which in this case gives an oscillating behavior which decays initially until stabilizing around a constant value.

A.2 SECOND-GENERATION ELECTRONS

The diffusion equation for the second generation of electrons is given by

$$\frac{\partial n_2(r,t)}{\partial t} = D_2\nabla^2 n_2(r,t) + 2\frac{n_1(r,t)}{\tau_1} \tag{A.4}$$

where the subscripts 1 and 2 refer to electrons of the first and second generation, respectively. The positive term $2n_1/\tau_1$ is a consequence of the fact that each electron from the first generation which undergoes an inelastic collision, at a rate given by the average lifetime τ_1, leads to the production of two electrons of the second generation. The decay of the second-generation electron number density is not considered here for simplicity.

The essence of the problem is to find the response u, which in this problem is $n_2(r,t)$, to the impulse f, which in this problem is $2n_1(r,t)/\tau_1$. The Green's function method is then to find the Green's function in the case of a (delta) impulse term, and then convolve it with the linear differential operator of the problem.

We want to recast Eq. (A.4) to get it in the form of

$$L(r,t)u(r,t) = f(r,t), \tag{A.5}$$

where L is a linear differential operator acting on u to yield f. This is readily done:

$$\underbrace{\left(\frac{\partial}{\partial t} - D_2\nabla^2\right)}_{L(r,t)}\underbrace{n_2(r,t)}_{u(r,t)} = \underbrace{2\frac{n_1(r,t)}{\tau_1}}_{f(r,t)}. \tag{A.6}$$

Doing this enables us to take advantage of the definition of the Green's function, which (in two dimensions r and t) reads

$$L(r,t)G(r-r',t-t') = \delta(r-r')\delta(t-t') \tag{A.7}$$

as mentioned in the introduction.

Let us now multiply both sides of Eq. (A.7) with $f(r',t')$ and integrate it

$$\int L(r,t)G(r-r',t-t')f(r',t')\,\mathrm{d}r'\,\mathrm{d}t' = \int \delta(r-r')\delta(t-t')f(r',t')\,\mathrm{d}r'\,\mathrm{d}t'. \tag{A.8}$$

The right hand side can be rewritten by using the identity given by the "picket fence representation" of $f(x)$

$$\int \delta(x-y)f(y)\,\mathrm{d}y = f(x) \tag{A.9}$$

such that

$$\int \delta(r-r')\delta(t-t')f(r',t')\,\mathrm{d}r'\,\mathrm{d}t' = f(r,t). \tag{A.10}$$

This gives us a new definition of $f(r,t)$, which we can combine with the relationship between L, u, and f, as given by Eq. (A.5), and insert in Eq. (A.8) to get

$$L(r,t)u(r,t) = \int L(r,t)G(r-r',t-t')f(r',t')\,\mathrm{d}r'\,\mathrm{d}t'\,. \tag{A.11}$$

Since $L(r,t)$ does not depend on r' or t', it can be taken outside the integral and can then be eliminated from both sides to yield

$$u(r,t) = \int G(r-r',t-t')f(r',t')\,\mathrm{d}r'\,\mathrm{d}t' \tag{A.12}$$

which can be rewritten as

$$n_2(r,t) = 2\int G(r-r',t-t')\frac{n_1(r',t')}{\tau_1}\,\mathrm{d}r'\,\mathrm{d}t'\,. \tag{A.13}$$

where we substituted $u(r,t)$ and $f(r',t')$ for $n_2(r,t)$ and $2n_1(r',t')/\tau_1$, respectively, as given by Eq. (A.6).

This integral is the convolution integral between the Green's function for the problem and the driving term, which solves the problem.

B PROGRAMMING WORK DONE

During the course of the ARGENT project, I have worked on several plugins for the Virtual NanoLab (VNL) software while being seconded at QuantumWise. In brief, I have been involved with the following tasks:

- Overhaul of the Wulff constructor plugin.
- Plugin for import/export of input files for input geometries used by MBN Explorer.
- Python class for creating input files for molecular dynamics and metadynamics simulations in ATK-ForceField using the CHARMM and GolP-CHARMM force fields.

As part of my work in the Platform team at QuantumWise I was involved in working on the graphical user interface of the VNL platform. My main task here was to update the Wulff constructor plugin which enables the user to create nanoparticles from any material by inputting surface energies and a radius, as described in Chapter 3. The update consisted of making possible the choice of arbitrary cut planes by the input of Miller indices and to load pre-calculated surface energies from an online database. In addition, a semi-transparent preview of the resulting Wulff construction was made available to better illustrate the effect of the chosen parameters.

To enable a closer link between the MBN Explorer (MBN) software package and the VNL platform, an input/output functionality was created for the reading/writing of input files for MBN. It was thus made possible to construct the input geometry for MBN simulations using VNL which was exploited to create (with the Wulff constructor plugin) the gold nanoparticles for the simulations performed in Chapter 3.

Finally, it was made simpler to use the CHARMM force field for molecular dynamics simulations in VNL by building a suite of functions in a comprehensive Python class which can read the required geometry and topology input files and translate the input to the Python format used by ATK-ForceField. The interaction between different types of atoms can be manually written in the input files read by ATK-ForceField, but for the cases simulated in Chapter 4 the resulting file was about 30 000 lines and an automated process was certainly necessary. The resulting Python class reads `pdb`, `psf`, and `inp` files and constructs the required atom types, bond, angle, dihedral, and improper dihedral terms as well as the nonbonded interactions and outputs this to a `py` file. Furthermore, the "virtual site" and "image charge" concepts of the GolP-CHARMM force field were implemented as well in this class. The geometry simulated in Chapter 4 was created using this functionality.

C PUBLICATIONS

The following is a list of publications to peer-reviewed journals and contributions to a book chapter published during the work done for this thesis.

1. Haume, K., Mason, N. J. & Solov'yov, A. V. Modeling of nanoparticle coatings for medical applications. *Eur. Phys. J. D* **70,** 181 (2016).
2. Haume, K. *et al.* Gold nanoparticles for cancer radiotherapy: a review. *Cancer Nanotechnol.* **7,** 8 (2016).
3. Bolsa Ferruz, M. *et al.* in *Nanoscale Insights into Ion-Beam Cancer Ther.* 379–434 (Springer International Publishing, Cham, 2017).
4. Haume, K. *et al.* Transport of secondary electrons through coatings of ion-irradiated metallic nanoparticles. *Eur. Phys. J. D* **72,** 116 (2018).

The front pages of the journal publications are shown on the following page.

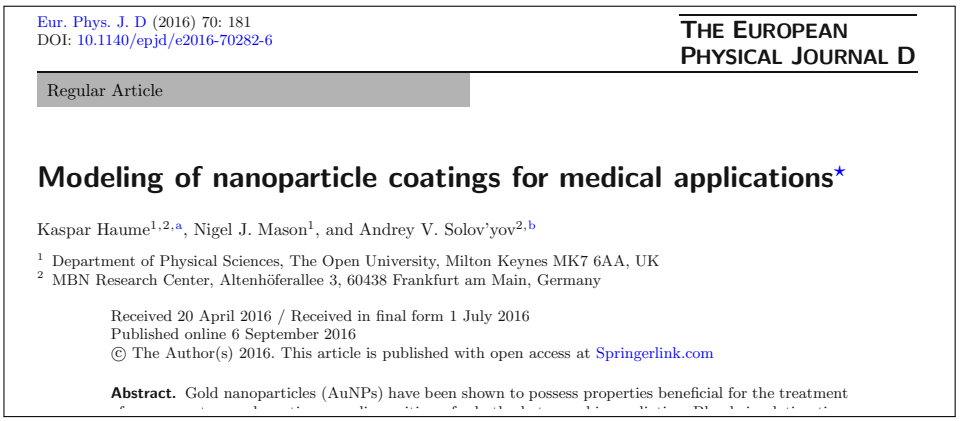

Eur. Phys. J. D (2016) 70: 181
DOI: 10.1140/epjd/e2016-70282-6

THE EUROPEAN PHYSICAL JOURNAL D

Regular Article

Modeling of nanoparticle coatings for medical applications*

Kaspar Haume[1,2,a], Nigel J. Mason[1], and Andrey V. Solov'yov[2,b]

[1] Department of Physical Sciences, The Open University, Milton Keynes MK7 6AA, UK
[2] MBN Research Center, Altenhöferallee 3, 60438 Frankfurt am Main, Germany

Received 20 April 2016 / Received in final form 1 July 2016
Published online 6 September 2016

Abstract. Gold nanoparticles (AuNPs) have been shown to possess properties beneficial for the treatment

Figure C.1: Front page of publication [1].

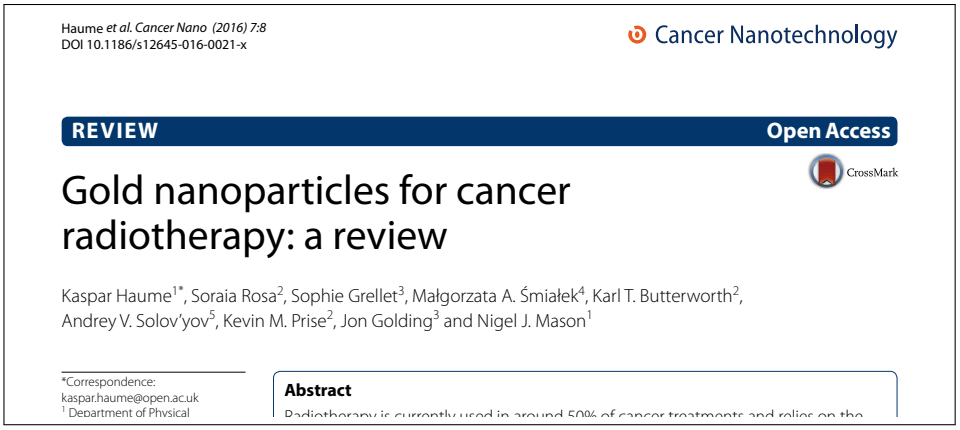

Haume *et al. Cancer Nano* (2016) 7:8
DOI 10.1186/s12645-016-0021-x

Cancer Nanotechnology

REVIEW Open Access

Gold nanoparticles for cancer radiotherapy: a review

Kaspar Haume[1*], Soraia Rosa[2], Sophie Grellet[3], Małgorzata A. Śmiałek[4], Karl T. Butterworth[2], Andrey V. Solov'yov[5], Kevin M. Prise[2], Jon Golding[3] and Nigel J. Mason[1]

*Correspondence:
kaspar.haume@open.ac.uk
[1] Department of Physical

Abstract
Radiotherapy is currently used in around 50% of cancer treatments and relies on the

Figure C.2: Front page of publication [2].

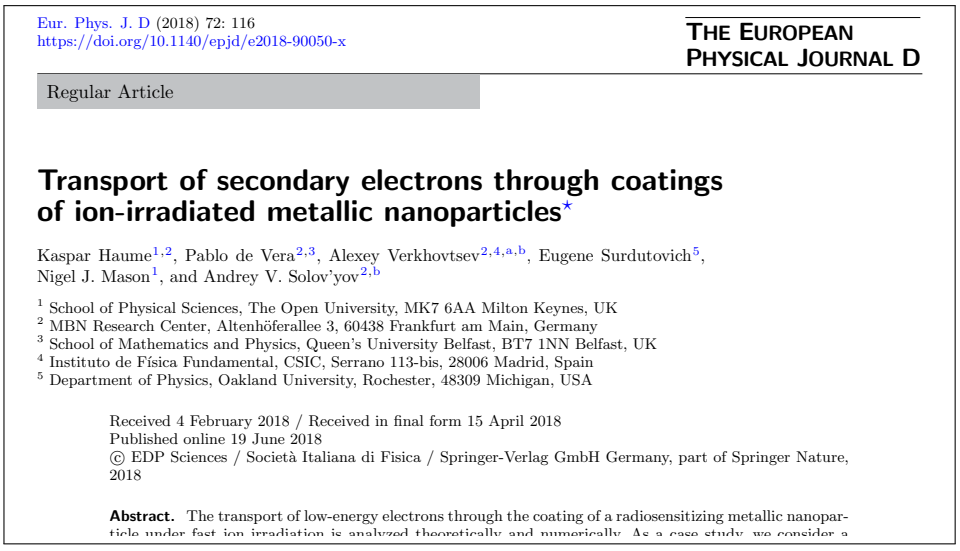

Eur. Phys. J. D (2018) 72: 116
https://doi.org/10.1140/epjd/e2018-90050-x

THE EUROPEAN PHYSICAL JOURNAL D

Regular Article

Transport of secondary electrons through coatings of ion-irradiated metallic nanoparticles*

Kaspar Haume[1,2], Pablo de Vera[2,3], Alexey Verkhovtsev[2,4,a,b], Eugene Surdutovich[5], Nigel J. Mason[1], and Andrey V. Solov'yov[2,b]

[1] School of Physical Sciences, The Open University, MK7 6AA Milton Keynes, UK
[2] MBN Research Center, Altenhöferallee 3, 60438 Frankfurt am Main, Germany
[3] School of Mathematics and Physics, Queen's University Belfast, BT7 1NN Belfast, UK
[4] Instituto de Física Fundamental, CSIC, Serrano 113-bis, 28006 Madrid, Spain
[5] Department of Physics, Oakland University, Rochester, 48309 Michigan, USA

Received 4 February 2018 / Received in final form 15 April 2018
Published online 19 June 2018

Abstract. The transport of low-energy electrons through the coating of a radiosensitizing metallic nanoparticle under fast ion irradiation is analyzed theoretically and numerically. As a case study, we consider a

Figure C.3: Front page of publication [4].

D PEG MOLECULE PARAMETERS

In this appendix the `pdb`, `psf`, and `inp` files used for the molecular dynamics simulations of the PEG molecule in Chapters 3 and 4 are listed as they were created in the process described in Section 3.2 and illustrated in Fig. 3.3.

D.1 PDB FILE

```
REMARK FOR INFORMATIONS, PLEASE CONTACT:
REMARK ZOETE VINCENT
REMARK VINCENT.ZOETE_AT_ISB-SIB.CH
REMARK SWISS INSTITUTE OF BIOINFORMATICS
REMARK MOLECULAR MODELING GROUP
REMARK QUARTIER SORGE - BATIMENT GENOPODE
REMARK CH-1015 LAUSANNE
REMARK SWITZERLAND
REMARK T: +41 21 692 4082
REMARK ************************************************************
REMARK DATE:  6/ 2/15  19: 7:28   CREATED BY USER: vzoete
ATOM    1 N1 LIG   1    -3.097 -2.812 0.000 1.00 0.00 LIG
ATOM    2 C1 LIG   1    -1.764 -3.582 0.000 1.00 0.00 LIG
ATOM    3 C2 LIG   1    -0.430 -2.812 0.000 1.00 0.00 LIG
ATOM    4 O1 LIG   1     0.904 -3.582 0.000 1.00 0.00 LIG
ATOM    5 C3 LIG   1     2.237 -2.812 0.000 1.00 0.00 LIG
ATOM    6 C4 LIG   1     3.571 -3.582 0.000 1.00 0.00 LIG
ATOM    7 O2 LIG   1     4.905 -2.812 0.000 1.00 0.00 LIG
ATOM    8 C5 LIG   1     6.239 -3.582 0.000 1.00 0.00 LIG
ATOM    9 C6 LIG   1     7.572 -2.812 0.000 1.00 0.00 LIG
ATOM   10 O3 LIG   1     8.906 -3.582 0.000 1.00 0.00 LIG
ATOM   11 C7 LIG   1    10.240 -2.812 0.000 1.00 0.00 LIG
ATOM   12 C8 LIG   1    11.573 -3.582 0.000 1.00 0.00 LIG
ATOM   13 O4 LIG   1    12.907 -2.812 0.000 1.00 0.00 LIG
ATOM   14 C9 LIG   1    14.241 -3.582 0.000 1.00 0.00 LIG
ATOM   15 C10 LIG  1    15.574 -2.812 0.000 1.00 0.00 LIG
ATOM   16 O5 LIG   1    16.908 -3.582 0.000 1.00 0.00 LIG
ATOM   17 C11 LIG  1    18.242 -2.812 0.000 1.00 0.00 LIG
ATOM   18 C12 LIG  1    19.575 -3.582 0.000 1.00 0.00 LIG
ATOM   19 S1 LIG   1    20.909 -2.812 0.000 1.00 0.00 LIG
ATOM   20 H1 LIG   1    -3.097 -1.802 0.000 1.00 0.00 LIG
ATOM   21 H2 LIG   1    -3.972 -3.317 0.000 1.00 0.00 LIG
ATOM   22 H3 LIG   1    -1.764 -4.127 0.944 1.00 0.00 LIG
ATOM   23 H4 LIG   1    -1.764 -4.127 -0.944 1.00 0.00 LIG
ATOM   24 H5 LIG   1    -0.430 -2.267 0.944 1.00 0.00 LIG
ATOM   25 H6 LIG   1    -0.430 -2.267 -0.944 1.00 0.00 LIG
ATOM   26 H7 LIG   1     2.237 -2.267 -0.944 1.00 0.00 LIG
```

```
ATOM   27 H8 LIG   1     2.237 -2.267 0.944 1.00 0.00 LIG
ATOM   28 H9 LIG   1     3.571 -4.127 0.944 1.00 0.00 LIG
ATOM   29 H10 LIG  1     3.571 -4.127 -0.944 1.00 0.00 LIG
ATOM   30 H11 LIG  1     6.239 -4.127 0.944 1.00 0.00 LIG
ATOM   31 H12 LIG  1     6.239 -4.127 -0.944 1.00 0.00 LIG
ATOM   32 H13 LIG  1     7.572 -2.267 -0.944 1.00 0.00 LIG
ATOM   33 H14 LIG  1     7.572 -2.267 0.944 1.00 0.00 LIG
ATOM   34 H15 LIG  1    10.240 -2.267 -0.944 1.00 0.00 LIG
ATOM   35 H16 LIG  1    10.240 -2.267 0.944 1.00 0.00 LIG
ATOM   36 H17 LIG  1    11.573 -4.127 0.944 1.00 0.00 LIG
ATOM   37 H18 LIG  1    11.573 -4.127 -0.944 1.00 0.00 LIG
ATOM   38 H19 LIG  1    14.241 -4.127 0.944 1.00 0.00 LIG
ATOM   39 H20 LIG  1    14.241 -4.127 -0.944 1.00 0.00 LIG
ATOM   40 H21 LIG  1    15.574 -2.267 -0.944 1.00 0.00 LIG
ATOM   41 H22 LIG  1    15.574 -2.267 0.944 1.00 0.00 LIG
ATOM   42 H23 LIG  1    18.242 -2.267 -0.944 1.00 0.00 LIG
ATOM   43 H24 LIG  1    18.242 -2.267 0.944 1.00 0.00 LIG
ATOM   44 H25 LIG  1    19.575 -4.127 0.944 1.00 0.00 LIG
ATOM   45 H26 LIG  1    19.575 -4.127 -0.944 1.00 0.00 LIG
ATOM   46 H27 LIG  1    21.290 -2.592 1.244 1.00 0.00 LIG
TER    47    LIG    1
END
```

D.2 PSF FILE

```
PSF EXT

     4 !NTITLE
 REMARKS original generated structure x-plor psf file
 REMARKS topology top_thiol-pegamine.rtf
 REMARKS topology top_all36_cgenff.rtf
 REMARKS segment LIG { first NONE; last NONE; auto angles dihedrals }

    46 !NATOM
      1 LIG    1      LIG    N1     NG321 -0.775000   14.0070       0
      2 LIG    1      LIG    C1     CG321  0.007000   12.0110       0
      3 LIG    1      LIG    C2     CG321 -0.015000   12.0110       0
      4 LIG    1      LIG    O1     OG301 -0.338000   15.9994       0
      5 LIG    1      LIG    C3     CG321 -0.011000   12.0110       0
      6 LIG    1      LIG    C4     CG321 -0.011000   12.0110       0
      7 LIG    1      LIG    O2     OG301 -0.338000   15.9994       0
      8 LIG    1      LIG    C5     CG321 -0.011000   12.0110       0
      9 LIG    1      LIG    C6     CG321 -0.011000   12.0110       0
     10 LIG    1      LIG    O3     OG301 -0.338000   15.9994       0
     11 LIG    1      LIG    C7     CG321 -0.011000   12.0110       0
     12 LIG    1      LIG    C8     CG321 -0.011000   12.0110       0
     13 LIG    1      LIG    O4     OG301 -0.338000   15.9994       0
     14 LIG    1      LIG    C9     CG321 -0.011000   12.0110       0
     15 LIG    1      LIG    C10    CG321 -0.011000   12.0110       0
     16 LIG    1      LIG    O5     OG301 -0.338000   15.9994       0
     17 LIG    1      LIG    C11    CG321 -0.010000   12.0110       0
     18 LIG    1      LIG    C12    CG321 -0.099000   12.0110       0
     19 LIG    1      LIG    S1     SG311 -0.242000   32.0600       0
```

```
  20 LIG   1      LIG    H1     HGPAM2 0.296000    1.0080       0
  21 LIG   1      LIG    H2     HGPAM2 0.296000    1.0080       0
  22 LIG   1      LIG    H3     HGA2   0.090000    1.0080       0
  23 LIG   1      LIG    H4     HGA2   0.090000    1.0080       0
  24 LIG   1      LIG    H5     HGA2   0.090000    1.0080       0
  25 LIG   1      LIG    H6     HGA2   0.090000    1.0080       0
  26 LIG   1      LIG    H7     HGA2   0.090000    1.0080       0
  27 LIG   1      LIG    H8     HGA2   0.090000    1.0080       0
  28 LIG   1      LIG    H9     HGA2   0.090000    1.0080       0
  29 LIG   1      LIG    H10    HGA2   0.090000    1.0080       0
  30 LIG   1      LIG    H11    HGA2   0.090000    1.0080       0
  31 LIG   1      LIG    H12    HGA2   0.090000    1.0080       0
  32 LIG   1      LIG    H13    HGA2   0.090000    1.0080       0
  33 LIG   1      LIG    H14    HGA2   0.090000    1.0080       0
  34 LIG   1      LIG    H15    HGA2   0.090000    1.0080       0
  35 LIG   1      LIG    H16    HGA2   0.090000    1.0080       0
  36 LIG   1      LIG    H17    HGA2   0.090000    1.0080       0
  37 LIG   1      LIG    H18    HGA2   0.090000    1.0080       0
  38 LIG   1      LIG    H19    HGA2   0.090000    1.0080       0
  39 LIG   1      LIG    H20    HGA2   0.090000    1.0080       0
  40 LIG   1      LIG    H21    HGA2   0.090000    1.0080       0
  41 LIG   1      LIG    H22    HGA2   0.090000    1.0080       0
  42 LIG   1      LIG    H23    HGA2   0.090000    1.0080       0
  43 LIG   1      LIG    H24    HGA2   0.090000    1.0080       0
  44 LIG   1      LIG    H25    HGA2   0.090000    1.0080       0
  45 LIG   1      LIG    H26    HGA2   0.090000    1.0080       0
  46 LIG   1      LIG    H27    HGP3   0.160000    1.0080       0

45 !NBOND: bonds
   1       2       1      20       1      21       2       3
   2      22       2      23       3       4       3      24
   3      25       4       5       5       6       5      26
   5      27       6       7       6      28       6      29
   7       8       8       9       8      30       8      31
   9      10       9      32       9      33      10      11
  11      12      11      34      11      35      12      13
  12      36      12      37      13      14      14      15
  14      38      14      39      15      16      15      40
  15      41      16      17      17      18      17      42
  17      43      18      19      18      44      18      45
  19      46

81 !NTHETA: angles
   1       2      23       1       2      22       1       2       3
   2       3      25       2       3      24       2       1      21
   2       1      20       3       4       5       3       2      23
   3       2      22       4       5      27       4       5      26
   4       5       6       4       3      25       4       3      24
   4       3       2       5       6      29       5       6      28
   5       6       7       6       7       8       6       5      27
   6       5      26       7       8      31       7       8      30
   7       8       9       7       6      29       7       6      28
   8       9      33       8       9      32       8       9      10
   9      10      11       9       8      31       9       8      30
  10      11      35      10      11      34      10      11      12
```

```
    10      9     33     10      9     32     11     12     37
    11     12     36     11     12     13     12     13     14
    12     11     35     12     11     34     13     14     39
    13     14     38     13     14     15     13     12     37
    13     12     36     14     15     41     14     15     40
    14     15     16     15     16     17     15     14     39
    15     14     38     16     17     43     16     17     42
    16     17     18     16     15     41     16     15     40
    17     18     45     17     18     44     17     18     19
    18     19     46     18     17     43     18     17     42
    19     18     45     19     18     44     20      1     21
    22      2     23     24      3     25     26      5     27
    28      6     29     30      8     31     32      9     33
    34     11     35     36     12     37     38     14     39
    40     15     41     42     17     43     44     18     45

 93 !NPHI: dihedrals
     1      2      3      4      1      2      3     24
     1      2      3     25      2      3      4      5
     3      4      5      6      3      4      5     26
     3      4      5     27      3      2      1     20
     3      2      1     21      4      5      6      7
     4      5      6     28      4      5      6     29
     4      3      2     22      4      3      2     23
     5      6      7      8      5      4      3     24
     5      4      3     25      6      7      8      9
     6      7      8     30      6      7      8     31
     7      8      9     10      7      8      9     32
     7      8      9     33      7      6      5     26
     7      6      5     27      8      9     10     11
     8      7      6     28      8      7      6     29
     9     10     11     12      9     10     11     34
     9     10     11     35     10     11     12     13
    10     11     12     36     10     11     12     37
    10      9      8     30     10      9      8     31
    11     12     13     14     11     10      9     32
    11     10      9     33     12     13     14     15
    12     13     14     38     12     13     14     39
    13     14     15     16     13     14     15     40
    13     14     15     41     13     12     11     34
    13     12     11     35     14     15     16     17
    14     13     12     36     14     13     12     37
    15     16     17     18     15     16     17     42
    15     16     17     43     16     17     18     19
    16     17     18     44     16     17     18     45
    16     15     14     38     16     15     14     39
    17     18     19     46     17     16     15     40
    17     16     15     41     19     18     17     42
    19     18     17     43     20      1      2     22
    20      1      2     23     21      1      2     22
    21      1      2     23     22      2      3     24
    22      2      3     25     23      2      3     24
    23      2      3     25     26      5      6     28
    26      5      6     29     27      5      6     28
    27      5      6     29     30      8      9     32
```

```
     30      8      9      33      31      8      9      32
     31      8      9      33      34      11     12     36
     34      11     12     37      35      11     12     36
     35      11     12     37      38      14     15     40
     38      14     15     41      39      14     15     40
     39      14     15     41      42      17     18     44
     42      17     18     45      43      17     18     44
     43      17     18     45      44      18     19     46
     45      18     19     46

    0 !NIMPHI: impropers


    0 !NDON: donors


    0 !NACC: acceptors


    0 !NNB

      0      0      0      0      0      0      0      0
      0      0      0      0      0      0      0      0
      0      0      0      0      0      0      0      0
      0      0      0      0      0      0      0      0
      0      0      0      0      0      0      0      0
      0      0      0      0      0      0

    1     0 !NGRP
      0      0      0
```

D.3 INP FILE

```
* Parameters generated by analogy by
* CHARMM General Force Field (CGenFF) program version 1.0.0
*

! Penalties lower than 10 indicate the analogy is fair; penalties
    between 10
! and 50 mean some basic validation is recommended; penalties higher
    than
! 50 indicate poor analogy and mandate extensive validation/optimization.


BONDS
CG321 CG321 222.50  1.5300 ! PROT alkane update, adm jr., 3/2/92
CG321 NG321 263.00  1.4740 ! AMINE aliphatic amines
CG321 OG301 360.00  1.4150 ! diethylether, alex
CG321 SG311 198.00  1.8180 ! PROT fitted to C-S s 9/26/92 (FL)
CG321 HGA2 309.00  1.1110 ! PROT alkane update, adm jr., 3/2/92
NG321 HGPAM2 453.10 1.0140 ! AMINE aliphatic amines
SG311 HGP3 275.00  1.3250 ! PROT methanethiol pure solvent, adm jr.,
    6/22/92
```

```
ANGLES
CG321 CG321 NG321 43.70 112.20 ! 46 , from CG331 CG321 NG311, PENALTY=
    2.1
CG321 CG321 OG301 45.00 111.50 ! diethylether, alex
CG321 CG321 SG311 58.00 114.50 ! PROT expt. MeEtS, 3/26/92 (FL)
CG321 CG321 HGA2 26.50  110.10 22.53 2.17900 ! PROT alkane update, adm
    jr., 3/2/92
NG321 CG321 HGA2 32.40  109.50 50.00 2.14000 ! AMINE aliphatic amines
OG301 CG321 HGA2 45.90  108.89 ! ETOB, Ethoxybenzene, cacha
SG311 CG321 HGA2 46.10  111.30 ! PROT vib. freq. and HF/geo. (DTN)
    8/24/90
HGA2 CG321 HGA2  35.50  109.00  5.40 1.80200 ! PROT alkane update, adm
    jr., 3/2/92
CG321 NG321 HGPAM2 41.00 112.10 ! AMINE aliphatic amines
HGPAM2 NG321 HGPAM2 42.00 105.85 ! AMINE aliphatic amines kevo: 29.50 ->
     42.00 based on MAM1 molvib & AMET scans
CG321 OG301 CG321 95.00 109.70 ! diethylether, alex
CG321 SG311 HGP3 38.80   95.00 ! PROT methanethiol pure solvent, adm jr.,
     6/22/92

DIHEDRALS
NG321 CG321 CG321 OG301 0.2500 1 180.00 ! 46 , from OG301 CG321 CG321 OG
    301, PENALTY= 33
NG321 CG321 CG321 OG301 1.2400 2  0.00 ! 46 , from OG301 CG321 CG321 OG
    301, PENALTY= 33
NG321 CG321 CG321 HGA2  0.1600 3  0.00 ! 46 , from NG311 CG321 CG331
    HGA3, PENALTY= 7.2
OG301 CG321 CG321 OG301 0.2500 1 180.00 ! 1,2 dimethoxyethane, 2/12/05,
    ATM
OG301 CG321 CG321 OG301 1.2400 2  0.00 ! 1,2 dimethoxyethane
OG301 CG321 CG321 SG311 0.8000 3  0.00 ! 46 , from SG311 CG321 CG324 NG
    3P2, PENALTY= 40
OG301 CG321 CG321 HGA2  0.1900 3  0.00 ! alkane, 4/98, yin and
    mackerell
SG311 CG321 CG321 HGA2  0.0100 3  0.00 ! PROT DTN 8/24/90
HGA2 CG321 CG321 HGA2   0.2200 3  0.00 ! LIPID alkanes
CG321 CG321 NG321 HGPAM2 0.1000 3 0.00 ! 46 , from CG331 CG321 NG311
    HGP1, PENALTY= 12.4
HGA2 CG321 NG321 HGPAM2 0.0100 3  0.00 ! amines
CG321 CG321 OG301 CG321 0.5700 1  0.00 ! 1,2 dimethoxyethane, 2/12/05,
    ATM
CG321 CG321 OG301 CG321 0.2900 2  0.00 ! 1,2 dimethoxyethane
CG321 CG321 OG301 CG321 0.4300 3  0.00 ! 1,2 dimethoxyethane
HGA2 CG321 OG301 CG321  0.2840 3  0.00 ! diethylether, alex
CG321 CG321 SG311 HGP3  0.2400 1  0.00 ! PRSH, n-thiopropanol, kevo for
     gsk/ibm
CG321 CG321 SG311 HGP3  0.1500 2  0.00 ! PRSH, n-thiopropanol, kevo for
     gsk/ibm
CG321 CG321 SG311 HGP3  0.2700 3  0.00 ! PRSH, n-thiopropanol, kevo for
     gsk/ibm
HGA2 CG321 SG311 HGP3   0.2000 3  0.00 ! PROT methanethiol pure solvent,
     adm jr., 6/22/92

IMPROPER
```

```
NONBONDED nbxmod 5 atom cdiel fshift vatom vdistance vfswitch -
cutnb 14.0 ctofnb 12.0 ctonnb 10.0 eps 1.0 e14fac 1.0 wmin 1.5

!see mass list above for better description of atom types
CG321  0.0     -0.0560  2.0100 0.0 -0.01 1.9 ! alkane (CT2)
HGA2   0.0     -0.0350  1.3400 ! alkane, igor, 6/05
HGP3   0.0     -0.1000  0.4500 ! methanethiol pure solvent, adm jr.,
    6/22/92
HGPAM2 0.0     -0.0100  0.8750 ! aliphatic amines
NG321  0.0     -0.0600  1.9900 ! aliphatic amines
OG301  0.0     -0.1000  1.6500 ! ether; LJ from THP, sng 1/06
SG311  0.0     -0.4500  2.0000 ! methanethiol/ethylmethylsulfide pure
    solvent
```

BIBLIOGRAPHY

1. Stewart, B. W.K. P. & Wild, C. P. World cancer report 2014. *World health organization* (2015).
2. Sánchez-Santos, M. E. in *Radiat. Damage Biomol. Syst.* (eds García Gómez-Tejedor, G. & Fuss, C. M.) 397–409 (Springer Netherlands, Dordrecht, 2012).
3. Schardt, D., Elsässer, T. & Schulz-Ertner, D. Heavy-ion tumor therapy: physical and radiobiological benefits. *Rev. Mod. Phys.* **82,** 383–425 (2010).
4. Surdutovich, E. & Solov'yov, A. V. Multiscale approach to the physics of radiation damage with ions. *Eur. Phys. J. D* **68,** 353 (2014).
5. Kobayashi, K. *et al.* Enhancement of radiation effect by heavy elements. *Rev. Mutat. Res.* **704,** 123–131 (2010).
6. Usami, N. *et al.* Comparison of DNA breaks at entrance channel and Bragg peak Induced by fast C^{6+} ions. *J. Radiat. Res.* **51,** 21–26 (2010).
7. Ranganathan, R. *et al.* Nanomedicine: towards development of patient-friendly drug-delivery systems for oncological applications. *Int. J. Nanomedicine* **7,** 1043–1060 (2012).
8. Akhter, S. *et al.* Gold nanoparticles in theranostic oncology: current state-of-the-art. *Expert. Opin. Drug. Del.* **9,** 1225–1243 (2012).
9. Asharani, P. V. *et al.* Toxicity of silver nanoparticles in zebrafish models. *Nanotechnology* **19,** 255102 (2008).
10. Chanda, N. *et al.* Radioactive gold nanoparticles in cancer therapy: therapeutic efficacy studies of GA–^{198}AuNP nanoconstruct in prostate tumor-bearing mice. *Nanomed.-Nanotechnol.* **6,** 201–209 (2010).
11. Sun, T. *et al.* Engineered nanoparticles for drug delivery in cancer therapy. *Angew. Chem. Int. Edit.* **53,** 12320–64 (2014).
12. Sharma, A. & Sharma, U. S. Liposomes in drug delivery: progress and limitations. *Int. J. Pharm.* **154,** 123–140 (1997).
13. Barbé, C. *et al.* Silica Particles: a novel drug-delivery system. *Adv. Mater.* **16,** 1959–1966 (2004).
14. Barreto, J. A. *et al.* Nanomaterials: applications in cancer imaging and therapy. *Adv. Mater.* **23,** H18–H40 (2011).
15. Mignot, A. *et al.* A top-down synthesis route to ultrasmall multifunctional Gd-based silica nanoparticles for theranostic applications. *Chem. - Eur. J.* **19,** 6122–6136 (2013).
16. Sancey, L. *et al.* The use of theranostic gadolinium-based nanoprobes to improve radiotherapy efficacy. *Brit. J. Radiol.* **87,** 20140134 (2014).
17. Schlathölter, T. *et al.* Improving proton therapy by metal-containing nanoparticles: Nanoscale insights. *Int. J. Nanomed.* **11,** 1549–1556 (2016).

18. Kwatra, D., Venugopal, A. & Anant, S. Nanoparticles in radiation therapy: a summary of various approaches to enhance radiosensitization in cancer. *Transl. Cancer Res.* **2,** 330–342 (2013).
19. Jain, S., Hirst, D. G. & O'Sullivan, J. M. Gold nanoparticles as novel agents for cancer therapy. *Br. J. Radiol.* **85,** 101–113 (2012).
20. Hainfeld, J. F., Slatkin, D. N. & Smilowitz, H. M. The use of gold nanoparticles to enhance radiotherapy in mice. *Phys. Med. Biol.* **49,** N309–N315 (2004).
21. Ghita, M. *et al.* A mechanistic study of gold nanoparticle radiosensitisation using targeted microbeam irradiation. *Sci. Rep.* **7,** 44752 (2017).
22. Lacombe, S., Porcel, E. & Scifoni, E. Particle therapy and nanomedicine: state of art and research perspectives. *Cancer Nanotechnol.* **8,** 9 (2017).
23. Taggart, L. E. *et al.* The role of mitochondrial function in gold nanoparticle mediated radiosensitisation. *Cancer Nanotechnol.* **5,** 5 (2014).
24. McMahon, S. J. *et al.* Biological consequences of nanoscale energy deposition near irradiated heavy atom nanoparticles. *Sci. Rep.* **1,** 1–10 (2011).
25. Coulter, J. A. *et al.* Cell type-dependent uptake, localization, and cytotoxicity of 1.9 nm gold nanoparticles. *Int. J. Nanomed.* **7,** 2673–2685 (2012).
26. Chithrani, B. D., Ghazani, A. A. & Chan, W. C. W. Determining the size and shape dependence of gold nanoparticle uptake into mammalian cells. *Nano Lett.* **6,** 662–668 (2006).
27. Elsässer, T. & Scholz, M. Cluster effects within the local effect model. *Radiat. Res.* **167,** 319–329 (2007).
28. Lin, Y. *et al.* Biological modeling of gold nanoparticle enhanced radiotherapy for proton therapy. *Phys. Med. Biol.* **60,** 4149–4168 (2015).
29. McMahon, S. J., Paganetti, H. & Prise, K. M. Optimising element choice for nanoparticle radiosensitisers. *Nanoscale* **8,** 581–589 (2016).
30. *Nanoscale Insights into Ion-Beam Cancer Therapy* 1st ed. (ed Solov'yov, A. V.) (Springer International Publishing, Cham, 2017).
31. Verkhovtsev, A. V., Surdutovich, E. & Solov'yov, A. V. Multiscale approach predictions for biological outcomes in ion-beam cancer therapy. *Sci. Rep.* **6,** 27654 (2016).
32. Martínez-Rovira, I. & Prezado, Y. Evaluation of the local dose enhancement in the combination of proton therapy and nanoparticles. *Med. Phys.* **42,** 6703–6710 (2015).
33. Xiao, F. *et al.* On the role of low-energy electrons in the radiosensitization of DNA by gold nanoparticles. *Nanotechnology* **22,** 465101 (2011).
34. Gilles, M., Brun, E. & Sicard-Roselli, C. Gold nanoparticles functionalization notably decreases radiosensitization through hydroxyl radical production under ionizing radiation. *Colloid. Surface. B* **123,** 770–777 (2014).

35. Karakoti, A. S. *et al.* PEGylated inorganic nanoparticles. *Angew. Chem. Int. Edit.* **50,** 1980–1994 (2011).

36. Liu, C.-J. *et al.* Enhancement of cell radiation sensitivity by pegylated gold nanoparticles. *Phys. Med. Biol.* **55,** 931–945 (2010).

37. Carter, J. D. *et al.* Nanoscale energy deposition by X-ray absorbing nanostructures. *J. Phys. Chem. B* **111,** 11622–11625 (2007).

38. Porcel, E. *et al.* Nano-sensitization under gamma rays and fast ion radiation. *J. Phys. Conf. Ser.* **373,** 012006 (2012).

39. Alizadeh, E. *et al.* Radiation damage to DNA: the indirect effect of low-energy electrons. *J. Phys. Chem. Lett.* **4,** 820–825 (2013).

40. Alizadeh, E., Orlando, T. M. & Sanche, L. Biomolecular damage induced by ionizing radiation: the direct and indirect effects of low-energy electrons on DNA. *Annu. Rev. Phys. Chem.* **66,** 379–398 (2015).

41. Joiner, M. & van der Kogel, A. *Basic clinical radiobiology* 4th ed. (eds Joiner, M. & van der Kogel, A.) (CRC Press, London, 2009).

42. Loeffler, J. S. & Durante, M. Charged particle therapy — optimization, challenges and future directions. *Nat. Rev. Clin. Oncol.* **10,** 411–424 (2013).

43. Krämer, M. & Durante, M. Ion beam transport calculations and treatment plans in particle therapy. *Eur. Phys. J. D* **60,** 195–202 (2010).

44. Giap, H., Roda, D. & Giap, F. Can proton beam therapy be clinically relevant for the management of lung cancer? *Transl. Cancer Res.* **4,** 3–15 (2015).

45. Polf, J. C. *et al.* Enhanced relative biological effectiveness of proton radiotherapy in tumor cells with internalized gold nanoparticles. *Appl. Phys. Lett.* **98,** 193702 (2011).

46. Usami, N. *et al.* Mammalian cells loaded with platinum-containing molecules are sensitized to fast atomic ions. *Int. J. Radiat. Biol.* **84,** 603–611 (2008).

47. Porcel, E. *et al.* Platinum nanoparticles: a promising material for future cancer therapy? *Nanotechnology* **21,** 085103 (2010).

48. Heredia-Avalos, S. *et al.* Target inner-shells contributions to the stopping power and straggling for H and He ions in gold. *J. Phys. Condens. Matter* **19,** 466205 (2007).

49. Scifoni, E., Surdutovich, E. & Solov'yov, A. V. Spectra of secondary electrons generated in water by energetic ions. *Phys. Rev. E* **81,** 021903 (2010).

50. Boudaïffa, B. Resonant formation of DNA strand breaks by low-energy (3 eV to 20 eV) electrons. *Science* **287,** 1658–1660 (2000).

51. Verkhovtsev, A. V., Korol, A. V. & Solov'yov, A. V. Revealing the mechanism of the low-energy electron yield enhancement from sensitizing nanoparticles. *Phys. Rev. Lett.* **114,** 063401 (2015).

52. Verkhovtsev, A. V., Korol, A. V. & Solov'yov, A. V. Electron production by sensitizing gold nanoparticles irradiated by fast ions. *J. Phys. Chem. C* **119,** 11000–11013 (2015).

53. Thierry, B. & Griesser, H. J. Dense PEG layers for efficient immunotargeting of nanoparticles to cancer cells. *J. Mater. Chem.* **22,** 8810 (2012).
54. Jeon, S. I. *et al.* Protein-surface interactions in the presence of polyethylene oxide. 1. Simplified theory. *J. Colloid Interface Sci.* **142,** 149–158 (1991).
55. Howard, M. D. *et al.* PEGylation of nanocarrier drug delivery systems: state of the art. *J. Biomed. Nanotechnol.* **4,** 133–148 (2008).
56. Rahme, K. *et al.* PEGylated gold nanoparticles: polymer quantification as a function of PEG lengths and nanoparticle dimensions. *RSC Adv.* **3,** 6085 (2013).
57. Smith, M. C. *et al.* Quantitative analysis of PEG-functionalized colloidal gold nanoparticles using charged aerosol detection. *Anal. Bioanal. Chem.* **407,** 3705–3716 (2015).
58. Hansen, M. *et al.* Analyzing the influence of PEG molecular weight on the separation of PEGylated gold nanoparticles by asymmetric-flow field-flow fractionation. *Anal. Bioanal. Chem.* **407,** 8661–8672 (2015).
59. Tsai, D.-H. *et al.* Quantitative determination of competitive molecular adsorption on gold nanoparticles using attenuated total reflectance-fourier transform infrared spectroscopy. *Langmuir* **27,** 9302–9313 (2011).
60. Otsuka, H., Nagasaki, Y. & Kataoka, K. PEGylated nanoparticles for biological and pharmaceutical applications. *Adv. Drug Deliv. Rev.* **55,** 403–419 (2003).
61. Jokerst, J. V. *et al.* Nanoparticle PEGylation for imaging and therapy. *Nanomedicine* **6,** 715–728 (2011).
62. Walkey, C. D. *et al.* Nanoparticle size and surface chemistry determine serum protein adsorption and macrophage uptake. *J. Am. Chem. Soc.* **134,** 2139–2147 (2012).
63. Manson, J. *et al.* Polyethylene glycol functionalized gold nanoparticles: the influence of capping density on stability in various media. *Gold Bull.* **44,** 99–105 (2011).
64. Ghorai, P. K. & Glotzer, S. C. Molecular dynamics simulation study of self-assembled monolayers of alkanethiol surfactants on spherical gold nanoparticles. *J. Phys. Chem. C* **111,** 15857–15862 (2007).
65. Luque, N. B. *et al.* Effect of coverage and defects on the adsorption of propanethiol on Au(111) surface: a theoretical study. *Langmuir* **27,** 14514–14521 (2011).
66. De Gennes, P. G. Conformations of polymers attached to an interface. *Macromolecules* **13,** 1069–1075 (1980).
67. De Gennes, P. G. Polymers at an interface; a simplified view. *Adv. Colloid Interface Sci.* **27,** 189–209 (1987).
68. Levin, C. S. *et al.* Determining the conformation of thiolated poly(ethylene glycol) on Au nanoshells by surface-enhanced Raman scattering spectroscopic assay. *Anal. Chem.* **78,** 3277–3281 (2006).
69. Vonarbourg, A. *et al.* Parameters influencing the stealthiness of colloidal drug delivery systems. *Biomaterials* **27,** 4356–4373 (2006).

70. Albanese, A., Tang, P. S. & Chan, W. C. W. The effect of nanoparticle size, shape, and surface chemistry on biological systems. *Annu. Rev. Biomed. Eng.* **14,** 1–16 (2012).

71. McCully, M. *et al.* Significance of the balance between intracellular glutathione and polyethylene glycol for successful release of small interfering RNA from gold nanoparticles. *Nano Res.* **8,** 3281–3292 (2015).

72. Kumar, D., Meenan, B. J. & Dixon, D. Glutathione-mediated release of Bodipy from PEG cofunctionalized gold nanoparticles. *Int. J. Nanomedicine* **7,** 4007–4022 (2012).

73. Laio, A. & Parrinello, M. Escaping free-energy minima. *P. Natl. Acad. Sci. USA* **99,** 12562–12566 (2002).

74. Barducci, A., Bonomi, M. & Parrinello, M. Metadynamics. *Wires. Comput. Mol. Sci.* **1,** 826–843 (2011).

75. Liu, C. J. *et al.* Enhanced X-ray irradiation-induced cancer cell damage by gold nanoparticles treated by a new synthesis method of polyethylene glycol modification. *Nanotechnology* **19** (2008).

76. Zhang, X.-D. *et al.* Size-dependent radiosensitization of PEG-coated gold nanoparticles for cancer radiation therapy. *Biomaterials* **33,** 6408–6419 (2012).

77. Surdutovich, E. & Solov'yov, A. V. Transport of secondary electrons and reactive species in ion tracks. *Eur. Phys. J. D* **69,** 193 (2015).

78. De Vera, P. *et al.* Semiempirical model for the ion impact ionization of complex biological media. *Phys. Rev. Lett.* **110,** 148104 (2013).

79. De Vera, P., Abril, I. & Garcia-Molina, R. Inelastic scattering of electron and light ion beams in organic polymers. *J. Appl. Phys.* **109,** 094901 (2011).

80. Frenkel, D. & Smit, B. *Understanding molecular simulation* 2nd ed. (Academic Press, San Diego, 2002).

81. Rapaport, D. C. *The art of molecular dynamics simulation* 2nd ed. (Cambridge University Press, Cambridge, 2004).

82. Allen, M. P. Introduction to molecular dynamics simulation. *Comput. Soft Matter From Synth. Polym. to Proteins* **23,** 1–28 (2004).

83. Born, M. & Oppenheimer, R. Zur quantentheorie der molekeln. *Ann. Phys.* **389,** 457–484 (1927).

84. Jones, J. E. On the determination of molecular fields. II. From the equation of state of a gas. *P. R. Soc. A* **106,** 463–477 (1924).

85. Stillinger, F. H. & Weber, T. A. Computer simulation of local order in condensed phases of silicon. *Phys. Rev. B* **31,** 5262–5271 (1985).

86. Tersoff, J. New empirical approach for the structure and energy of covalent systems. *Phys. Rev. B* **37,** 6991–7000 (1988).

87. Daw, M. S. & Baskes, M. I. Embedded-atom method: derivation and application to impurities, surfaces, and other defects in metals. *Phys. Rev. B* **29,** 6443–6453 (1984).

88. Sutton, A. P. & Chen, J. Long-range Finnis–Sinclair potentials. *Philos. Mag. Lett.* **61,** 139–146 (1990).

89. Doye, J. & Wales, D. Global minima for transition metal clusters described by Sutton-Chen potentials. *New J. Chem.* **22,** 733–744 (1998).

90. MacKerell, A. D. *et al.* All-atom empirical potential for molecular modeling and dynamics studies of proteins. *J. Phys. Chem. B* **102,** 3586–3616 (1998).

91. Vanommeslaeghe, K. *et al.* CHARMM general force field: a force field for drug-like molecules compatible with the CHARMM all-atom additive biological force fields. *J. Comput. Chem.* **31,** 671–690 (2010).

92. Brooks, B. R. *et al.* CHARMM: the biomolecular simulation program. *J. Comput. Chem.* **30,** 1545–1614 (2009).

93. Jorgensen, W. L. *et al.* Comparison of simple potential functions for simulating liquid water. *J. Chem. Phys.* **79,** 926 (1983).

94. Verlet, L. Computer "Experiments" on classical fluids. I. Thermodynamical properties of Lennard-Jones molecules. *Phys. Rev.* **159,** 98–103 (1967).

95. Swope, W. C. *et al.* A computer simulation method for the calculation of equilibrium constants for the formation of physical clusters of molecules: application to small water clusters. *J. Chem. Phys.* **76,** 637–649 (1982).

96. Schneider, J. & Colombi Ciacchi, L. Specific material recognition by small peptides mediated by the interfacial solvent structure. *J. Am. Chem. Soc.* **134,** 2407–2413 (2012).

97. Meißner, R. H., Wei, G. & Ciacchi, L. C. Estimation of the free energy of adsorption of a polypeptide on amorphous SiO_2 from molecular dynamics simulations and force spectroscopy experiments. *Soft Matter* **11,** 6254–6265 (2015).

98. O'Brien, C. P. *et al.* Modeling of peptide adsorption interactions with a poly(lactic acid) surface. *Langmuir* **24,** 14115–14124 (2008).

99. Berendsen, H. J. C. *et al.* Molecular dynamics with coupling to an external bath. *J. Chem. Phys.* **81,** 3684–3690 (1984).

100. Andersen, H. C. Molecular dynamics simulations at constant pressure and/or temperature. *J. Chem. Phys.* **72,** 2384–2393 (1980).

101. Solov'yov, I. A. *et al.* MesoBioNano explorer — a universal program for multiscale computer simulations of complex molecular structure and dynamics. *J. Comput. Chem.* **33,** 2412–2439 (2012).

102. Hünenberger, P. H. in *Advanced computer simulation. Advances in polymer science* (eds Holm, C. & Kremer, K.) 105–149 (Springer Berlin Heidelberg, 2005).

103. Schneider, T. & Stoll, E. Molecular-dynamics study of a three-dimensional one-component model for distortive phase transitions. *Phys. Rev. B* **17,** 1302–1322 (1978).

104. Kühne, T. D. Second generation Car-Parrinello molecular dynamics. *Wiley Interdiscip. Rev. Comput. Mol. Sci.* **4,** 391–406 (2014).

105. Ben-Nun, M. & Martínez, T. J. in *Adv. Chem. Phys.* 439–512 (John Wiley & Sons, Inc., New York, 2002).

106. Merchant, B. A. & Madura, J. D. A review of coarse-grained molecular dynamics techniques to access extended spatial and temporal scales in biomolecular simulations. *Annu. Rep. Comput. Chem* **7,** 67–87 (2011).

107. Kmiecik, S. *et al.* Coarse-grained protein models and their applications. *Chem. Rev.* **116,** 7898–7936 (2016).

108. Da Rocha, E. L., Caramori, G. F. & Rambo, C. R. Nanoparticle translocation through a lipid bilayer tuned by surface chemistry. *Phys. Chem. Chem. Phys.* **15,** 2282–90 (2013).

109. Yang, K. & Ma, Y.-Q. Computer simulation of the translocation of nanoparticles with different shapes across a lipid bilayer. *Nat. Nanotechnol.* **5,** 579–583 (2010).

110. Li, Y. *et al.* Multiscale modeling and uncertainty quantification in nanoparticle-mediated drug/gene delivery. *Comput. Mech.* **53,** 511–537 (2014).

111. Abrams, C. & Bussi, G. Enhanced sampling in molecular dynamics using metadynamics, replica-exchange, and temperature-acceleration. *Entropy* **16,** 163–199 (2013).

112. Bernardi, R. C., Melo, M. C. & Schulten, K. Enhanced sampling techniques in molecular dynamics simulations of biological systems. *Biochim. Biophys. Acta* **1850,** 872–877 (2015).

113. Barducci, A., Bussi, G. & Parrinello, M. Well-tempered metadynamics: a smoothly converging and tunable free-energy method. *Phys. Rev. Lett.* **100,** 020603 (2008).

114. Schneider, J. *et al.* ATK-ForceField: a new generation molecular dynamics software package. *Model. Simul. Mater. Sc.* **25,** 085007 (2017).

115. Laio, A. *et al.* Assessing the accuracy of metadynamics. *J. Phys. Chem. B* **109,** 6714–6721 (2005).

116. Bussi, G., Laio, A. & Parrinello, M. Equilibrium free energies from nonequilibrium metadynamics. *Phys. Rev. Lett.* **96,** 090601 (2006).

117. Stokbro, K. *et al.* Semiempirical model for nanoscale device simulations. *Phys. Rev. B* **82,** 1–8 (2010).

118. Brandbyge, M. *et al.* Density-functional method for nonequilibrium electron transport. *Phys. Rev. B* **65,** 165401 (2002).

119. Nikjoo, H. *et al.* Track structure in radiation biology: theory and applications. *Int. J. Radiat. Biol.* **73,** 355–364 (1998).

120. Humphrey, W., Dalke, A. & Schulten, K. VMD: visual molecular dynamics. *J. Mol. Graph.* **14,** 33–38 (1996).

121. Tribello, G. A. *et al.* PLUMED 2: new feathers for an old bird. *Comput. Phys. Commun.* **185,** 604–613 (2014).

122. Williams, T., Kelley, C. & Others. *Gnuplot 5.0: an interactive plotting program* 2013.

123. Daniel, M. C. & Astruc, D. Gold nanoparticles: assembly, supramolecular chemistry, quantum-size-related properties, and applications toward biology, catalysis, and nanotechnology. *Chem. Rev.* **104,** 293–346 (2004).

124. Perrault, S. D. *et al.* Mediating tumor targeting efficiency of nanoparticles through design. *Nano Lett.* **9,** 1909–1915 (2009).

125. Gref, R. *et al.* Biodegradable long-circulating polymeric nanospheres. *Science* **263,** 1600–1603 (1994).

126. Greish, K. Enhanced permeability and retention of macromolecular drugs in solid tumors: a royal gate for targeted anticancer nanomedicines. *J. Drug Target.* **15,** 457–464 (2007).

127. Gref, R. *et al.* "Stealth" corona-core nanoparticles surface modified by polyethylene glycol (PEG): influences of the corona (PEG chain length and surface density) and of the core composition on phagocytic uptake and plasma protein adsorption. *Colloid. Surface. B* **18,** 301–313 (2000).

128. Alexis, F. *et al.* Factors affecting the clearance and biodistribution of polymeric nanoparticles. *Mol. Pharm.* **5,** 505–515 (2008).

129. Kingshott, P., Thissen, H. & Griesser, H. J. Effects of cloud-point grafting, chain length, and density of PEG layers on competitive adsorption of ocular proteins. *Biomaterials* **23,** 2043–2056 (2002).

130. Lee, H. *et al.* A coarse-grained model for polyethylene oxide and polyethylene glycol: conformation and hydrodynamics. *J. Phys. Chem. B* **113,** 13186–13194 (2009).

131. Li, Y. & Hu, Y. Computational investigation of the influence of chain length on the shielding effect of PEGylated nanoparticles. *RSC Adv.* **4,** 51022–51031 (2014).

132. Terekhin, V. V. *et al.* Conjugates of gold nanoparticles and poly(ethylene glycol): formation in hydrosol, direct transfer to organic medium, and stability of organosols. *Colloid J.* **77,** 511–519 (2015).

133. Wuelfing, W. P. *et al.* Nanometer gold clusters protected by surface-bound monolayers of thiolated poly(ethylene glycol) polymer electrolyte. *J. Am. Chem. Soc.* **120,** 12696–12697 (1998).

134. Verma, A. & Stellacci, F. Effect of surface properties on nanoparticle-cell interactions. *Small* **6,** 12–21 (2010).

135. Monopoli, M. P. *et al.* Biomolecular coronas provide the biological identity of nanosized materials. *Nat. Nanotechnol.* **7,** 779–786 (2012).

136. Tiwari, P. M. *et al.* Functionalized gold nanoparticles and their biomedical applications. *Nanomaterials* **1,** 31–63 (2011).

137. Sapsford, K. E. *et al.* Functionalizing nanoparticles with biological molecules: developing chemistries that facilitate nanotechnology. *Chem. Rev.* **113,** 1904–2074 (2013).

138. Wulff, G. Zur frage der geschwindigkeit des wachsthums und der auflösung der krystallflächen. *Z. Kristallogr. Cryst. Mater.* **34,** 449–530 (1901).

139. Zoete, V. *et al.* SwissParam: a fast force field generation tool for small organic molecules. *J. Comput. Chem.* **32,** 2359–2368 (2011).

140. Barnard, A. S. Modeling the impact of alkanethiol SAMs on the morphology of gold nanocrystals. *Cryst. Growth Des.* **13,** 5433–5441 (2013).

141. Vericat, C. *et al.* Self-assembled monolayers of thiols and dithiols on gold: new challenges for a well-known system. *Chem. Soc. Rev.* **39,** 1805 (2010).

142. Pool, R., Schapotschnikow, P. & Vlugt, T. J. H. Solvent effects in the adsorption of alkyl thiols on gold structures: a molecular simulation study. *J. Phys. Chem.* **111,** 10201–10212 (2007).

143. Wright, L. B. *et al.* GolP-CHARMM: first-principles based force fields for the interaction of proteins with Au(111) and Au(100). *J. Chem. Theory Comput.* **9,** 1616–1630 (2013).

144. Kankate, L., Turchanin, A. & Gölzhäuser, A. On the release of hydrogen from the S–H groups in the formation of self-assembled monolayers of thiols. *Langmuir* **25,** 10435–10438 (2009).

145. Tielens, F. & Santos, E. AuS and SH bond formation/breaking during the formation of alkanethiol SAMs on Au(111): a theoretical study. *J. Phys. Chem. C* **114,** 9444–9452 (2010).

146. Solov'yov, I. A., Solov'yov, A. V. & Greiner, W. Fusion process of Lennard-Jones clusters: global minima and magic numbers formation. *Int. J. Mod. Phys. E* **13,** 47 (2003).

147. Solov'yov, I. *et al.* Cluster growing process and a sequence of magic numbers. *Phys. Rev. Lett.* **90,** 053401 (2003).

148. Flory, P. J. *Principles of polymer chemistry* 2nd ed. (Cornell University Press, Ithaca, 1953).

149. Owens, D. E. & Peppas, N. A. Opsonization, biodistribution, and pharmacokinetics of polymeric nanoparticles. *Int. J. Pharm.* **307,** 93–102 (2006).

150. Simpson, C. A. *et al.* Short-chain PEG mixed monolayer protected gold clusters increase clearance and red blood cell counts. *ACS Nano* **5,** 3577–3584 (2011).

151. Zimmt, M. B., Peterson, K. A. & Fayer, M. D. Short polymer chain statistics and the relationship to end to end electronic excitation transport: random walks with variable-step lengths. *Macromolecules* **21,** 1145–1154 (1988).

152. Tambasco, M., Kumar, S. K. & Szleifer, I. Quantitatively modeling the equilibrium properties of thiol-decorated gold nanoparticles. *Langmuir* **24,** 8448–51 (2008).

153. Lin, J. *et al.* PEGylation on mixed monolayer gold nanoparticles: effect of grafting density, chain length, and surface curvature. *J. Colloid Interface Sci.* **504,** 325–333 (2017).

154. Gölander, C.-G. *et al.* in *Poly(ethylene glycol) chemistry* (ed Harris, J. M.) 1st ed., 221–245 (Springer Science & Business Media, Boston, 1992).

155. Häkkinen, H. The gold–sulfur interface at the nanoscale. *Nat. Chem.* **4,** 443–455 (2012).

156. Maksymovych, P. *et al.* Gold adatom as a key structural component in self-assembled monolayers of organosulfur molecules on Au(111). *Prog. Surf. Sci.* **85,** 206–240 (2010).

157. Voznyy, O. *et al.* The role of gold adatoms and stereochemistry in self-assembly of methylthiolate on Au(111). *J. Am. Chem. Soc.* **131,** 12989–12993 (2009).

158. Iori, F. *et al.* GolP: an atomistic force-field to describe the interaction of proteins with Au(111) surfaces in water. *J. Comput. Chem.* **30,** 1465–1476 (2009).

159. Hoefling, M. *et al.* Interaction of amino acids with the Au(111) surface: adsorption free energies from molecular dynamics simulations. *Langmuir* **26,** 8347–8351 (2010).

160. Iori, F. & Corni, S. Including image charge effects in the molecular dynamics simulations of molecules on metal surfaces. *J. Comput. Chem.* **29,** 1656–1666 (2008).

161. Lavrich, D. J. *et al.* Physisorption and chemisorption of alkanethiols and alkyl sulfides on Au(111). *J. Phys. Chem. B* **102,** 3456–3465 (1998).

162. Wright, L. B. *et al.* Facet selectivity in gold binding peptides: exploiting interfacial water structure. *Chem. Sci.* **6,** 5204–5214 (2015).

163. Sanche, L. Low energy electron-driven damage in biomolecules. *Eur. Phys. J. D* **35,** 367–390 (2005).

164. Cedervall, T. *et al.* Understanding the nanoparticle-protein corona using methods to quantify exchange rates and affinities of proteins for nanoparticles. *P. Natl. Acad. Sci. USA* **104,** 2050–2055 (2007).

165. Abril, I. *et al.* in *Theory of heavy ion collision physics in hadron therapy* (ed Belkić, D.) 129–164 (Academic Press, San Diego, 2013).

166. Salvat, F., Jablonski, A. & Powell, C. J. ELSEPA — Dirac partial-wave calculation of elastic scattering of electrons and positrons by atoms, positive ions and molecules. *Comput. Phys. Commun.* **165,** 157–190 (2005).

167. Surdutovich, E. & Solov'yov, A. V. Random walk approximation for the radial dose dependence. *Eur. Phys. J. D* **66,** 245 (2012).

168. Wilson, W. E. & Nikjoo, H. A Monte Carlo code for positive ion track simulation. *Radiat. Environ. Biophys.* **38,** 97–104 (1999).

169. Abate, J. & Valkó, P. P. Multi-precision Laplace transform inversion. *Int. J. Numer. Methods Eng.* **60,** 979–993 (2004).

170. Sigmund, P. *Particle Penetration and Radiation Effects* (Springer Berlin Heidelberg, New York, 2006).

171. De Vera, P. *Charged particle interaction with biological materials: modelling and application to ion beam cancer therapy* PhD thesis (Universitat d'Alacant, 2016).

172. Emfietzoglou, D., Cucinotta, F. A. & Nikjoo, H. A complete dielectric response model for liquid water: a solution of the Bethe ridge problem. *Radiat. Res.* **164,** 202–211 (2005).

173. Incerti, S. *et al.* Comparison of GEANT4 very low energy cross section models with experimental data in water. *Med. Phys.* **37,** 4692–4708 (2010).

174. Blanco, F. *et al.* Modelling low energy electron and positron tracks in biologically relevant media. *Eur. Phys. J. D* **67,** 199 (2013).

175. De Vera, P., Garcia-Molina, R. & Abril, I. Angular and energy distributions of electrons produced in arbitrary biomaterials by proton impact. *Phys. Rev. Lett.* **114,** 018101 (2015).

176. Dingfelder, M. *et al.* Electron emission from foils and biological materials after proton impact. *Radiat. Phys. Chem.* **77,** 1213–1217 (2008).

177. Itikawa, Y. & Mason, N. Cross sections for electron collisions with water molecules. *J. Phys. Chem. Ref. Data* **34,** 1 (2005).

178. Lindhard, J. On the properites of a gas of charged particles. *Kong. Dansk. Vidensk.* **28,** 8 (1954).

179. Garcia-Molina, R. *et al.* Inelastic scattering and energy loss of swift electron beams in biologically relevant materials. *Surf. Interface Anal.* **49,** 11–17 (2017).

180. Nikjoo, H. *et al.* Radiation track, DNA damage and response — a review. *Reports Prog. Phys.* **79,** 116601 (2016).

181. Tan, Z. *et al.* Electron stopping power and mean free path in organic compounds over the energy range of 20 eV to 10 000 eV. *Nucl. Instrum. Meth. B* **222,** 27–43 (2004).

182. Hayashi, H. *et al.* The complete optical spectrum of liquid water measured by inelastic x-ray scattering. *P. Natl. Acad. Sci. USA* **97,** 6264–6266 (2000).

183. *Handbook of optical constants of solids* 1st ed. (ed Palik, E. D.) (Academic press, Orlando, 1997).

184. Abril, I. *et al.* Dielectric description of wakes and stopping powers in solids. *Phys. Rev. A* **58,** 357–366 (1998).

185. Garcia-Molina, R. *et al.* in *Radiation damage in biomolecular systems* 239–261 (Springer, 2012).

186. Abril, I. *et al.* Effect of the Bethe surface description on the electronic excitations induced by energetic proton beams in liquid water and DNA. *Nucl. Instrum. Meth. B* **268,** 1763–1767 (2010).

187. Kanter, H. Slow-electron mean free paths in aluminum, silver, and gold. *Phys. Rev. B* **1,** 522–536 (1970).

188. Sze, S., Moll, J. & Sugano, T. Range-energy relation of hot electrons in gold. *Solid. State. Electron.* **7,** 509–523 (1964).

189. Michaud, M., Wen, A. & Sanche, L. Cross sections for low-energy (1–100 eV) electron elastic and inelastic scattering in amorphous ice. *Radiat. Res.* **159,** 3–22 (2003).

190. Lindau, I. *et al.* Determination of the escape depth of photoemitted electrons in gold in the energy range 25–75 eV by use of synchrotron radiation. *J. Electron Spectrosc.* **8,** 487–491 (1976).

191. Gergely, G. *et al.* Experimental measurements of the surface excitation parameters of Cu, Au, Ni, Ag, Ge and Pd based on Si and other reference standard materials. *Surf. Interface Anal.* **36,** 1098–1101 (2004).

192. Liljequist, D. A study of errors in trajectory simulation with relevance for 0.2–50 eV electrons in liquid water. *Radiat. Phys. Chem.* **77,** 835–853 (2008).

193. Salvat, F. Optical-model potential for electron and positron elastic scattering by atoms. *Phys. Rev. A* **68,** 012708 (2003).

194. Jablonski, A., Salvat, F. & Powell, C. J. Comparison of electron elastic-scattering cross sections calculated from two commonly used atomic potentials. *J. Phys. Chem. Ref. Data* **33,** 409–451 (2004).

195. Verkhovtsev, A., Korol, A. V. & Solov'yov, A. V. Formalism of collective electron excitations in fullerenes. *Eur. Phys. J. D* **66,** 253 (2012).

196. Solov'yov, A. V. Plasmon excitations in metal clusters and fullerenes. *Int. J. Mod. Phys. B* **19,** 4143–4184 (2005).

197. Connerade, J.-P. & Solov'yov, A. V. Formalism for multiphoton plasmon excitation in jellium clusters. *Phys. Rev. A* **66,** 013207 (2002).

198. Fano, U. Effects of configuration interaction on intensities and phase shifts. *Phys. Rev.* **124,** 1866–1878 (1961).

199. Gerchikov, L. G. *et al.* Surface- and volume-plasmon excitations in electron inelastic scattering on metal clusters. *Phys. Rev. A* **62,** 043201 (2000).

200. Assadollahzadeh, B. & Schwerdtfeger, P. A systematic search for minimum structures of small gold clusters Au_n ($n = 2$ to 20) and their electronic properties. *J. Chem. Phys.* **131,** 064306 (2009).

201. Kreipl, M. S., Friedland, W. & Paretzke, H. G. Time- and space-resolved Monte Carlo study of water radiolysis for photon, electron and ion irradiation. *Radiat. Environ. Biophys.* **48,** 11–20 (2009).

202. Nikjoo, H. *et al.* Track-structure codes in radiation research. *Radiat. Meas.* **41,** 1052–1074 (2006).

203. Lacombe, L. *et al.* Rare reaction channels in real-time time-dependent density functional theory: the test case of electron attachment. *Eur. Phys. J. D* **69,** 195 (2015).

204. Fedor, J. *et al.* Fragmentation of transient water anions following low-energy electron capture by H_2O/D_2O. *J. Phys. B At. Mol. Opt.* **39,** 3935–3944 (2006).

205. Haume, K., Mason, N. J. & Solov'yov, A. V. Modeling of nanoparticle coatings for medical applications. *Eur. Phys. J. D* **70,** 181 (2016).

206. Haume, K. *et al.* Transport of low-energy secondary electrons through coatings of ion-irradiated metallic nanoparticles (submitted). *Eur. Phys. J. D.* arXiv: 1801.06894 (2018).

207. Wang, M. & Thanou, M. Targeting nanoparticles to cancer. *Pharmacol. Res.* **62,** 90–99 (2010).

208. Pianetta, P. *X-Ray Data Booklet* (ed Thompson, A. C.) chap. 3.2 (Lawrence Berkeley National Laboratory, University of California, Berkley, California, 2009).

209. Meesungnoen, J. *et al.* Low-energy electron penetration range in liquid water. *Radiat. Res.* **158,** 657–660 (2002).